

## AN ABSTRACT OF THE THESIS OF

June Raven Marion for the degree of Master of Science in Ocean, Earth and Atmospheric Sciences presented on August 19, 2014.

Title: Providing the Best Turbulent Heat Flux Estimates from Eddy Correlation and Bulk Methods Using DYNAMO Data.

Abstract approved: \_\_\_\_\_

Simon P. de Szoeke

In this thesis, data collected during the Dynamics of the Madden Julian Oscillation (DYNAMO) field campaign, conducted in the Indian Ocean in Fall of 2011, is used to compute heat fluxes at the air-sea interface by evaluating eddy covariances and bulk aerodynamic formulae. Errors in daily average gridded fluxes computed with the COARE version 3.5 bulk aerodynamic formula are assessed with respect to five independent in situ time series from DYNAMO and the Tropical Ocean-Global Atmosphere Coupled Ocean-Atmosphere Response Experiment (TOGA-COARE) in the Western Pacific (Nov. 1992 – Feb. 1993).

Oregon State University (OSU), the NOAA Physical Science Division (PSD), and University of Connecticut (UConn) deployed three nearly collocated covariance flux measurement systems on the R/V *Revelle* during DYNAMO. Covariance and bulk fluxes are compared among these systems, and the experimental setup and calculation methods used for the OSU system are described.

OAFlux and TropFlux are two gridded flux products, both of which use global atmospheric reanalyses and in situ observations to produce estimates of surface heat and momentum flux. An array of 106 buoys deployed in the Pacific, Atlantic, and Indian Oceans provide valuable in situ observations of surface meteorological variables including air and ocean temperatures, wind speed and relative humidity. The buoy data is assimilated into the reanalyses and incorporated into the bias correction strategy employed by TropFlux, and the optimal interpolation weights of OAFlux. Locations not constrained by observations have higher root mean square difference between these two products than those near buoys. In fact, OAFlux and TropFlux can sometimes disagree by 100% of the mean flux when buoy data sources are not nearby.

Estimating net air-sea surface heat flux to an accuracy of  $10 \text{ W/m}^2$  requires resolution of diurnal solar warming of the ocean surface, known as the diurnal warm layer (Price, et al., 1986), and diffusive cooling of the viscous sub-layer known as the cool skin (Saunders, 1967). Warm layer and cool skin corrections to the bulk ocean temperature are modeled in the COARE bulk flux algorithm (Fairall et al., 1996). Rigorously calibrated and quality controlled DYNAMO data is used to assess the sensitivity of bulk flux calculations to warm layer and cool skin phenomena. Ignoring both corrections results in positive biases of  $1.9 \text{ W/m}^2$  and  $8.7 \text{ W/m}^2$  for sensible and latent heat respectively, mostly because of systematic overestimates of the SST due to the prominence of the cool skin.

Two new techniques for including the effects of the warm layer and cool skin on daily fluxes are presented and tested using DYNAMO observations. Both techniques make use of a simple solar radiation model that distributes the daily average solar

radiation in a half cosine over 12 hours of the day at hourly resolution. In the first technique the COARE algorithm computes warm layer and cool skin corrections hourly with the solar radiation model. This reduces the root mean square errors of sensible and latent heat fluxes to 0.7 and 2.9 W/m<sup>2</sup>. This improvement requires more than 10 bulk aerodynamic computations per day, a considerable computational expense when evaluating fluxes for decades of global gridded data.

In the second technique, the daily average flux is evaluated beforehand in COARE using the solar radiation model with a range of daily average radiation and wind speed values. The results are sorted by solar radiation and wind speed in a lookup table that specifies an adjustment to the fluxes due to the warm layer and cool skin corrections. The adjustment corrects the daily fluxes computed without the warm layer and cool skin corrections. Using the lookup table corrections reduces the root mean square errors to 0.96 and 3.5 W/m<sup>2</sup>, nearly as well as the more computationally intensive diurnal solar model.

The cool skin correction makes the biggest difference to the fluxes. Ignoring it can cause 10% overestimation of sensible and latent heat flux. Though they ignore the cool skin, both OAFlux and TropFlux estimate the R/V *Revelle* sensible and latent fluxes to within 0.1% of the mean flux. It is possible that fortuitous errors in the gridded products compensate the neglected effect of the cool skin.

Diurnal warm layers intermittently warm the surface temperature during the convectively suppressed phase of the MJO. The warmest net (warm layer minus cool skin) daily mean difference between the bulk and interface temperature reaches 1° C, which is significant compared to the sea-air temperature difference on the order of 2° C.

Observations of stronger diurnal warm layers in the convectively suppressed phase suggest that systematic intraseasonal modulation of the warm layer affects air-sea interaction in the MJO.

©Copyright by June Raven Marion  
August 19, 2014  
All Rights Reserved

Providing the Best Turbulent Heat Flux Estimates from Eddy Correlation and Bulk  
Methods Using DYNAMO Data

by

June Raven Marion

A THESIS

submitted to

Oregon State University

in partial fulfillment of  
the requirements for the  
degree of

Master of Science

Presented August 19, 2014  
Commencement June 2015

Master of Science thesis of June Raven Marion presented on August 19, 2014

APPROVED:

---

Major Professor, representing Ocean, Earth and Atmospheric Sciences

---

Dean of the College of Earth, Ocean, and Atmospheric Sciences

---

Dean of the Graduate School

I understand that my thesis will become part of the permanent collection of Oregon State University libraries. My signature below authorizes release of my thesis to any reader upon request.

---

June Raven Marion, Author

## ACKNOWLEDGEMENTS

I cannot thank Simon de Szoeki enough for his support and encouragement while working toward my Masters. Thanks to ample time at sea together during my first term, we developed a trusting relationship that allowed for candid exchanges of encouragement, frustration, and appreciation. As Simons first graduate student, I was continually impressed with his willingness to consider suggestions of how to improve his teaching and advising skills; an excellent quality not present in all aspiring professors. He was flexible about where and when I worked from the very beginning. Simon was always available to help me with science, programming and life hurdles. He supported my educational and professional goals as they changed and evolved during my time at OSU. Simons hard work and dedication to science are inspirational.

Dr. James Edson was always a joy to work with. Whether building flux systems in Australia, discussing data filters aboard the R/V *Revelle*, or explaining the nuances of the COARE bulk flux algorithm, Jim was always smiling and encouraging me to pursue science. He generously served on my committee and hosted me in Connecticut for 2 weeks to help further my research. I express my sincere appreciation for the opportunity to work (and vacation) with Jim.

Additionally I'd like to thank Dr. Dudley Chelton and Chris Knowels for serving on my committee. Dudley read me entire thesis, despite that only a small part related to his area of expertise. Though Dudley is technically retired, he kindly agreed to serve on my committee. His comments on my thesis reflected his many years of experience advising students and were very helpful improving my final draft.

Furthermore, I extend the deepest thanks to my wonderful friends and family, both here in Corvallis, and around the world. I have had a most adventurous and fulfilling three years working toward my degree and I can attribute my fond memories to those who shared this time with me. My sister Shayna is a shining star in my life. Her encouraging words, unyielding support, and ever-present smile are the best a person could ever ask for. She inspires me more than words can express! We are absolutely

blessed to have each other. I can't wait to see what amazing thing is next for her. My dearest friend Aili Johnston moves mountains by following her heart with ton of charm and a touch of tenacity. She has shown me that sometimes putting yourself out on a limb, exposing your vulnerability, and speaking your mind is the key to success. More than anyone I know, Aili seeks challenges in life. The Picasso quote "I am always doing that which I cannot do, in order that I may learn how to do it" is how Aili lives her life daily. She will change the world; I don't doubt it for a second.

I could go on for days about all of the support and love I have received pursuing my Masters, but I have a boat to catch! To my parents, Grandma Loretta, and sisters, Winnie and Heidi, Pablo, Kalsin, Meghan, Ale, Cris, Jonko, Dan, Kara, Michael Summers both Joanies, Katalina Charles, Yuki, all my favorite climbing partners, old friends and new, and many more, thank you all for an awesome time!!!

## TABLE OF CONTENTS

	<u>Page</u>
Chapter 1: Introduction .....	1
1.1 Turbulent Surface Fluxes .....	2
1.1.1 Eddy Covariance Fluxes.....	2
1.1.2 Bulk Fluxes .....	2
1.1.3 Gridded Flux Products from Satellites and Reanalysis .....	3
1.2 Madden Julian Oscillation.....	3
1.3 TOGA-COARE.....	13
1.4 DYNAMO.....	15
1.5 Research Goals.....	17
Chapter 2: Turbulent Fluxes measured in DYNAMO .....	20
2.1 Eddy Correlation Fluxes.....	23
2.1.1 Theory .....	23
2.1.2 Assumptions.....	26
2.2 Experimental Setup .....	27
2.2.1 Eddy Correlation Flux Calculations.....	30
2.2.1.1 Data Corrections Required for EC Flux Calculations .....	32
a) Motion Correction .....	32
b) Rotate into the Mean Wind .....	34
c) Detrending high-rate variables in the flux window.....	36
2.2.1.2 Compute Covariance Fluxes .....	37
2.3 Methods: Bulk Fluxes .....	37
2.3.1 Theory .....	38

TABLE OF CONTENTS (Continued)

	<u>Page</u>
2.3.2 COARE Version 3.5.....	40
2.3.3 Implementation of COARE.....	41
2.4 Results .....	43
2.4.1 OSU Fluxes .....	43
2.4.2 OSU Bulk vs. Covariance, & Removing the Mean or the Trend.....	45
2.4.3 Comparisons Between OSU, PSD, and UConn Fluxes .....	47
2.4.3.1 OSU, PSD and UConn Covariances.....	48
2.4.3.2 OSU, PSD, and UConn Covariance vs. Consensus Bulk.....	52
2.4.3.3 OSU, PSD, and UConn Bulk vs. Consensus Bulk .....	53
2.5 Discussion .....	54
Chapter 3: Gridded Flux Product Evaluation.....	57
3.1 Observations Ingested into the Gridded Products .....	57
3.2 Independent datasets from the DYNAMO and TOGA-COARE field campaigns.....	59
3.2.1 <i>Revelle</i> fluxes and Meteorological Data.....	60
3.2.2 APL Buoys .....	62
3.2.3 <i>Moana Wave</i> data from TOGA-COARE .....	62
3.3 Gridded products on a 1° X 1° spatial grid.....	63
3.3.1 OAFlux.....	63
3.3.2 TropFlux.....	65
3.4 OAFlux and TropFlux Differences .....	67
3.5 Near Surface Ocean Temperature .....	72
3.5.1 Cool skin .....	72

## TABLE OF CONTENTS (Continued)

	<u>Page</u>
3.5.2 Warm Layer.....	74
3.5.2.1 Satellite Sea Surface Temperature Retrievals .....	80
3.6 Methods and Results .....	83
3.6.1 Solar Radiation Model .....	83
3.6.2 Sensitivity experiments to the Warm layer/Cool skin with <i>Revelle</i> DYNAMO data .....	84
3.6.3 Lookup Table .....	91
3.6.4 Comparison of the 80.5° E, 0° N RAMA Buoy to the Revelle.....	95
3.6.5 Gridded Flux Product Comparison .....	98
3.6.5.1 Effect of Distance from a TPR Buoy on Gridded Flux Estimates .....	99
3.6.5.2 TPR Bias Corrections .....	104
3.6.6 Intraseasonality of warm layer computed with TropFlux and the Solar Model.....	108
3.7 Discussion .....	112
3.7.1 OAFlux and TropFlux Variability.....	112
3.7.2 Intraseasonality of the warm layer .....	112
3.7.3 Gridded Flux Products in the Vicinity of a TPR buoy.....	113
Chapter 4: Conclusions .....	116
4.1 Turbulence Flux Calculations .....	116
4.2 Warm layer and Cool skin Corrections .....	117
4.3 Gridded Flux Estimates.....	119
Appendix 123	
A.1 Experimental Setup .....	123
A.1.1 Wiring .....	124

## TABLE OF CONTENTS (Continued)

	<u>Page</u>
A.1.2 Data Acquisition .....	126
A.2 Processing Raw Data .....	130
A.2.1 MATLAB Reader Programs .....	130
A.2.2 Quality Control .....	132
Bibliography	139

## LIST OF FIGURES

<u>Figure</u>	<u>Page</u>
1.2. The MJO index indicates where the MJO is detected and the magnitude of the signal. Thin lines with numbers are observations and numbers are the day of the month. Yellow lines are individual model forecasts and the green line is the ensemble average. The grey area indicates 50% confidence, while the light grey is 90% confidence. Panels a-d show the progression of observed MJO indices from 2011 August 24 – November 12, along with successive 15 day forecasts from 2011 October 3 – November 27. [Figure credit: Jon Gottschalck, NOAA Climate Prediction Center].....	9
1.3. The intensive Flux Array included 4 buoys, and R/V's Xiangyonghong and <i>Moana Wave</i> . .....	14
1.4. the R/V <i>Revelle</i> and Mirai station and APL buoy locations are shown. Also the island stations on Male, Gan, and Diego Garcia Islands are shown. Pirate infested waters prevented measurements off the coast of Somalia where MJO genesis is thought to occur.....	16
2.1 Marine Atmospheric Boundary Layer (MABL): the surface molecular layer is a thin film in direct contact with the surface of the ocean. The turbulent boundary layer, ~ 10% of the MABL, is where ships and buoys make measurements. The mixed layer, on the order of 80% of the MABL, is well mixed due to developed turbulence. The inversion layer is characterized by reverse gradients and inhibits mixing beyond the MABL. ....	22
2.2 Vertical wind speed divided by horizontal wind speed versus wind direction, binned by horizontal wind speed. ....	32
2.3 Motion correction applied to u, v, and w, where u is positive toward the bow, v is positive to the starboard, and w is positive up. Blue lines are the measured velocities as seen by the anemometer, pink lines are the platform velocities from the integrated platform accelerations, and black lines are the corrected wind vectors. ....	34
2.4 Ship relative vertical wind speed versus ship relative wind direction, sorted by horizontal wind speed. ....	35
2.5 Motion corrected sonic u, v, w with the trend removed (pink) and the mean only removed (blue) for 20 minutes.....	36
2.6 Sensible (top) and latent (bottom) heat flux for legs 2-3 of DYNAMO. Black are covariance fluxes and red are bulk.....	44

## LIST OF FIGURES (Continued)

<u>Figure</u>	<u>Page</u>
2.7 OSU detrended covariance versus bulk fluxes computed with $\tau = 10$ and 20 minutes the black dashed line is a one-to-one reference; $m$ is the slope of the corresponding reference line.....	45
2.8 OSU covariance fluxes with the trend removed, and the mean only removed computed with $\tau = 10$ and 20 minutes. ....	46
2.10 UConn, OSU, and PSD eddy covariance heat fluxes (window length of 20 minutes) versus bulk consensus fluxes. Regression lines and slopes are shown in corresponding colors.....	53
2.11 OSU and PSD bulk fluxes computed for 10-minute averaged bulk quantities versus bulk consensus fluxes. ....	54
2.12 Bulk and covariance mean and standard error for sensible and latent heat flux. Consensus bulk are considered the most reliable. For Sensible heat, OSU covariance, PSD bulk, and Uconn Covariance estimates agree with the consensus bulk fluxes. For latent heat, only the Uconn estimates are in good agreement with the consensus bulk estimate, though OSU covariance is close. ....	56
3.1. Stars indicate the locations of existing TAO, PIRATA and RAMA buoys in the Pacific, Atlantic and Indian Oceans respectively.....	58
3.2. Black stars are the locations of RAMA and TAO buoys in the Indian and west Pacific Oceans. Red dots at latitude $79^\circ$ E, longitude $0^\circ$ N, $1.5^\circ$ S, and $9.5^\circ$ S are the APL buoys. The R/V <i>Revelle</i> and R/V <i>Moana Wave</i> are shown as red dots at $80.5^\circ$ E, $0^\circ$ N and $156^\circ$ E, $1.7^\circ$ S respectively.....	60
3.3 Legs I-IV of the DYNAMO campaign. Leg I departed from Darwin Australia, while all other legs docked in Thailand. Transect paths during legs II & III are seen. All gridded flux data compared to the <i>Revelle</i> was interpolated to the nearest grid point to the daily average location of the ship. This map shows a $2^\circ$ grid. OAFlux and TropFLux use $1^\circ$ grid centered on the $0.5^\circ$ . [Figurecredit: Ludovic Bariteau, NOAA Physical Science Division].....	61
3.4. The difference between OAFlux and TropFlux for 27 November 2011. Black dots are the locations of all currently active TPR buoys. ....	68
3.5. (a) The annual average difference between OAFlux and TropFlux SHF for the year 2011. (b) the % difference between OAFlux and TropFlux SHF relative to the TropFlux mean SHF. (c) the TropFlux mean SHF. Black dots are 106 TPR buoys that are ingested into reanalyses used by both products and are also used in both flux algorithms. ....	69

LIST OF FIGURES (Continued)

<u>Figure</u>	<u>Page</u>
3.6. As in Figure 3.5 but for latent heat flux.....	70
3.7. OAFlux and TropFlux SHF (left) and LHF (right) at 106 buoy locations for 365 days (top) and non-buoy locations (bottom). Each plots shows the histogram of rms difference for 365 days of data. Each realization is RMSD over the spatial pattern of buoy locations, or all locations for one day. The number of realizations for each is $n_b=106$ buoys, and $n_g=16351$ common grid points. Each plot contains 50 bins and the sum of these 50 bins equals 365.....	71
3.9. Observed 0.05 m skin temperature, 4 m thermosalinograph temperature, and the daily average difference between temperatures at these two depths. An intraseasonal signal in the daily average warm layer is apparent in the observations. ....	79
3.10. number of occurrences of the temperature correction required from the observed 4 m Thermosalinograph and the skin temperature modeled in COARE from the 0.05 m sea snake observations. There are 95 realizations and 95 data bins. ....	80
3.11 The simple solar model approximates the diurnal cycle by distributing the daily average shortwave radiation in a half cosine throughout 12 hours in the day. 7 days of observed 10 minute SWR from the <i>Revelle</i> and the corresponding solar model are shown.....	84
3.12. Heat flux difference between the best estimate from 10 min observations and worst estimate from daily averages, as a function of the sensible heat flux, computed with 10 minute resolution (blue dots) and averaged to daily resolution (pink stars) for (a) sensible heat flux and for (b) latent heat flux. ....	87
3.13. The black dots in all 3 panels show the error induced by ignoring the warm layer and cool skin corrections when using a 1 m SST. The cyan dots in panel a show the bias when the warm layer is modeled, but the cool skin is ignored. The pink dots in panel b show the bias when the cool skin is modeled, but the warm layer remains ignored. The green dots in panel c illustrate bias when both the cool skin and the warm layer corrections modeled.....	88
3.14. As in Figure 3.8, but for LHF. ....	88

LIST OF FIGURES (Continued)

<u>Figure</u>	<u>Page</u>
3.15. On the left the mean of all <i>Revelle Experiments</i> are shown for SHF on the top, and LHF on the bottom. The Right panels show the standard deviation of each experiment. Ignoring the cool skin correction makes the biggest difference in both the mean and standard deviation for latent and sensible heat fluxes. The dashed lines represent the value computed from our <i>best estimate</i> of SST. ....	90
3.16. Daily average SHF (a) and LHF (b), without the warm layer and cool skin corrections, and SHF (c) and LHF (d) corrections with the warm layer and cool skin corrections turned on; binned by wind speed and daily average short wave radiation.....	93
3.17. Daily average warm layer (a) and cool skin (b) corrections to adjust from 1 m to the interface temperature binned by wind speed and daily average short wave radiation.....	94
3.18. Sensible and latent heat flux mean and standard deviation computed with the <i>Revelle</i> data with the warm layer and cool skin corrections on, compared to the closest RAMA buoy at 80.5° E, 0° N, computed with, and without warm and cool corrections. ....	97
3.19. Sensible and latent heat fluxes computed from in situ data collected on the <i>Revelle</i> and the <i>Moana Wave</i> plotted with the OAFlux and TropFlux at the nearest grid cell to the location of each ship at the time. ....	100
3.20. As in Figure 3.19, except using the APL buoys located at 78.5° E and 0° N, 1.5° S, and 9.5° S. Note different time axes. ....	101
3.21. The mean and standard deviation of SHF and LHF compared between independent in situ observations and TropFlux and OAFlux. The <i>Revelle</i> was stationed closest to a TPR buoy (3 km). The equator and 1.5° S APL buoys were next closest (166 km) followed by the <i>Moana Wave</i> (188 km). The 9.5° S APL buoy was farthest from a TPR buoy (244 km). ....	103
3.22. The bias computed as the annual average of OAFlux or TropFlux – TPR for 525 buoy years (small dots), and binned by the TPR values (stars). A buoy year is comprised of any calendar year in which buoy data was available greater than 75% of the year. Biases for specific humidity, wind speed, air temperature and SST are shown. ....	106

## LIST OF FIGURES (Continued)

<u>Figure</u>	<u>Page</u>
3.23. Time-longitude plots of outgoing longwave radiation anomalies (a), 1 m ocean temperature (b), and computed warm layer – cool skin corrections from 1 m to interface ocean temperature. Latitude is averaged over $\pm 5^\circ$ , and the x-axis is longitude with the coast of Somalia on the left, and the maritime continent on the right .....	109
3.24. The average gustiness correction over $\pm 5^\circ$ latitude added to TropFlux wind speed is plotted zonally. The $\pm 5^\circ$ latitude strip is inset on the bottom for reference. Large gustiness corrections were added to the Indian Ocean, Maritime Continent, and Western Pacific. The spatially resolved gustiness correction is inset on the bottom for reference. ....	110
3.25. Time-longitude plots of TropFlux wind speed (a), wind speed +the proposed gustiness correction (b), and the warm layer – cool skin corrections computed with the gusty wind speed (c). Averaging is as in Figure 3.23 .....	111
A.0.1. Wiring for the Campbell CR3000, Gladiator gyroscope/accelerometer, including the RS485 converter.....	125
A.0.2. Wiring for The ships navigation system and the Young barometer .....	125
A.0.3. Wiring for LiCor Infrared Gas Analyzer and CSAT3 Sonic Anemometer .....	126
A.0.4. The CR3000 welcome screen. Hover the mouse over the data tab to see cord convert and data viewing options. ....	128
A.0.5. Selection pane for binary files. ....	129
A.0.6. Selection pane for CSV files.....	129

## LIST OF TABLES

<u>Table</u>	<u>Page</u>
2.1	OSU sensible and latent heat flux mean and standard deviation computed with $\tau = 10$ and 20 minutes using covariance and bulk methods..... 47
2.2	Mean and standard deviation of bulk Consensus, OSU and PSD covariance and bulk fluxes. Correlations are with respect to bulk Consensus fluxes.....51
3.1.	<i>Revelle</i> Experiment names, resolution, and SST depth used for all variations. The warm layer, cool skin and solar input can either be Modeled, Ignored, or Observed, indicated by an M, I, O. ....86
3.2.	<i>Revelle</i> hourly mean and standard deviation are computed with the warm layer and cool skin corrections on. Hourly resolution fluxes are averaged to daily and the std is recomputed. ....98
3.3.	RAMA hourly mean, standard deviation and correlation with <i>Revelle</i> fluxes computed with the warm layer and cool skin corrections on and off. Hourly resolution fluxes are averaged to daily and the std and correlation with the <i>Revelle</i> are recomputed. ....98
4.1.	The root mean square difference between OAFlux and TropFlux is compared for site near, and far from in situ buoy data sources. 3 km from a buoy corresponds to a single time series from the <i>Revelle</i> . 160-240 km from TPR includes three APL buoys and the <i>Moana Wave</i> . The last column is all grid cells that have a TPR buoy compered to all that do not. ....104
A.1.	Instrumentation, sampling frequency, and measurement height .....124
A.2.	Phase 1 quality control procedures, nan values in excess of min/max, missing values, and diagnostic flags as noted. Also despiked4sigma all data streams one time unless otherwise noted. ....133

# Providing the Best Turbulent Heat Flux Estimates from Eddy Correlation and Bulk Methods Using DYNAMO Data

## CHAPTER 1: INTRODUCTION

### 1.1 TURBULENT SURFACE FLUXES

Surface fluxes are the dominant mechanism by which momentum and heat are exchanged between the ocean and atmosphere and are thus important to many aspects of the ocean and atmospheric heat budget and circulation. Surface momentum flux drives upper ocean currents and Ekman transport, while heat and moisture fluxes near the equator fuel atmospheric convection and basin-scale circulations, such as the Hadley and Walker Cells. Absorption of tropical sunlight gives rise to warm surface temperatures in tropical oceans, which become the dominant source of energy for developing storms. Increased wind speed increases evaporation, and latent heat stored in the atmospheric boundary layer. Evaporation and wind stress also cool the surface and deepen the ocean mixed layer. Both of these coupled phenomena decrease sea surface temperature (SST) and act as negative feedbacks, diminishing the energy available to the atmosphere. As such, air-sea coupling is complicated and non-linear and can be difficult to accurately represent in climate and numerical weather prediction models. Fluxes are an important boundary condition for the atmosphere and ocean; hence, inaccurate flux parameterization can have deleterious effects on model simulations. Therefore, accurate parameterization of air-sea

fluxes is vital for understanding climate, the hydrologic cycle, and the global energy budget.

### **1.1.1 Eddy Covariance Fluxes**

One approach to measure fluxes is to directly measure the fluctuations driven by the turbulent eddies responsible for the flux. This is the eddy correlation (EC) method. In this framework, researchers sample turbulent eddies directly as they pass through a sensor volume, measuring the flux of heat, mass, moisture, or momentum. Once a few assumptions are met, EC fluxes can represent fluxes to a high degree of confidence. This technique is based on the theory that turbulent eddies are an important mechanism of energy transport in a fluid system, and therefore most of the vertical transport of momentum, sensible heat, and moisture in a fluid system can be measured as the covariance of vertical motion with horizontal motion, air temperature, and moisture, respectively. However, while the equations are simple, thorough quality control and complex motion correction procedures are required to produce accurate fluxes.

### **1.1.2 Bulk Fluxes**

Fluxes can be computed from bulk aerodynamic formulae based on the principle of Monin-Obukhov similarity theory that the vertical flux of a scalar is proportional to the vertical gradient of the scalar. The required inputs are commonly measured and include SST, air temperature, relative humidity, and wind speed. These so-called bulk fluxes are well suited for ship based measurement procedures. Reliable bulk fluxes can be computed using mean wind speed, temperature, and moisture differences between the saturated sea-surface and the air at the measurement height.

### **1.1.3 Gridded Flux Products from Satellites and Reanalysis**

Gridded flux products based on satellite and reanalysis data provide spatially resolved estimates of air-sea fluxes for long time records of multiple decades. Gridded flux products offer spatial context compared to local in situ measurements, which are limited to a single point for the duration of a deployment.

I evaluate two gridded flux products, the Objectively Analyzed Air-Sea Flux (OAFlux) (Yu and Weller 2007, Jin and Weller, 2008) and TropFlux (Kumar et al. 2012) during DYNAMO and COARE. Both OAFlux and TropFlux use  $1^\circ \times 1^\circ$  daily average SST, air temperature, humidity and wind speed for input variables to COARE version 3.0 bulk algorithm. Both products offer spatially resolved estimates of momentum flux and sensible and latent heat flux.

## **1.2 MADDEN JULIAN OSCILLATION**

The Madden Julian Oscillation (MJO) is characterized by an eastward propagating envelope of deep convection which forms in the equatorial Indian Ocean with a period of 30-90 days (Madden & Julian, 1971; Zhang, 2005). A single MJO is composed of a convectively suppressed phase, an initiation phase, and a convectively active phase. Density differences between the atmospheric boundary layer, which is warmed and moistened by surface heat fluxes, and the upper troposphere, which is cooled by longwave radiation, provide buoyancy that drives atmospheric convection. In the tropics, deep updrafts saturated with water vapor characterize active convection, and heavy local precipitation events may result. Whether updrafts are precipitating or not,

convection is a primary vertical heat transport process from the boundary layer to the free troposphere (AMS Glossary of Meteorology).

Outgoing longwave radiation (OLR) anomalies are used to detect deep convection and the MJO. OLR is observed as an upward radiance from the Earth by satellites. The emitted radiation is proportional to the 4<sup>th</sup> power of temperature according to the Stefan-Boltzman law. The radiating temperature of the atmosphere depends on the radiating height. In regions of deep convection, cloud tops approach the upper troposphere and the radiating temperature is relatively cold, resulting in a negative OLR anomaly. In clear sky conditions, the radiating temperature is closer to the surface temperature, which is relatively warm, and results in a positive OLR anomaly. Hence, satellite retrievals of OLR give clues to global convective conditions: negative OLR anomalies indicate deep convective systems, while positive OLR anomalies indicate clear sky conditions.

The MJO convectively suppressed phase exhibits minimal organized convection, positive OLR anomalies, weak and variable easterlies, and the net surface heat flux is into the ocean, raising the ocean surface temperature. In contrast, the active phase exhibits periods of enhanced convection, negative OLR anomalies, westerly wind bursts, and net surface heat flux out of the ocean, cooling the ocean surface. The transition from suppressed to active, known as the initiation phase, is less well defined, but often exhibits a deep moistening of the troposphere. It is helpful to think of the active phase of the MJO as an eastward propagating planetary-scale envelope of deep convection, with embedded negative OLR anomalies and strong westerly wind bursts. The MJO is sometimes described using 8 phases corresponding to the geographic location of the convectively active phase of the MJO. Figure 1.1 (adapted from Cassou, 2008) shows composites of

OLR throughout phases 2, 4, 6, and 8 of the MJO as the signal progresses eastward around the globe. In Phase 2, negative OLR anomalies characteristic of the MJO convectively active phase are centered in the Indian Ocean. By Phase 4, the negative anomaly has progressed over the Maritime Continent. Phase 6 has a developing positive OLR anomaly in the Indian Ocean, characteristic of the MJO suppressed phase there, and the negative anomaly east of the maritime continent has strengthened. A positive OLR anomaly in phase 8 is centered over the Maritime Continent with a weakening negative anomaly in the central Pacific.

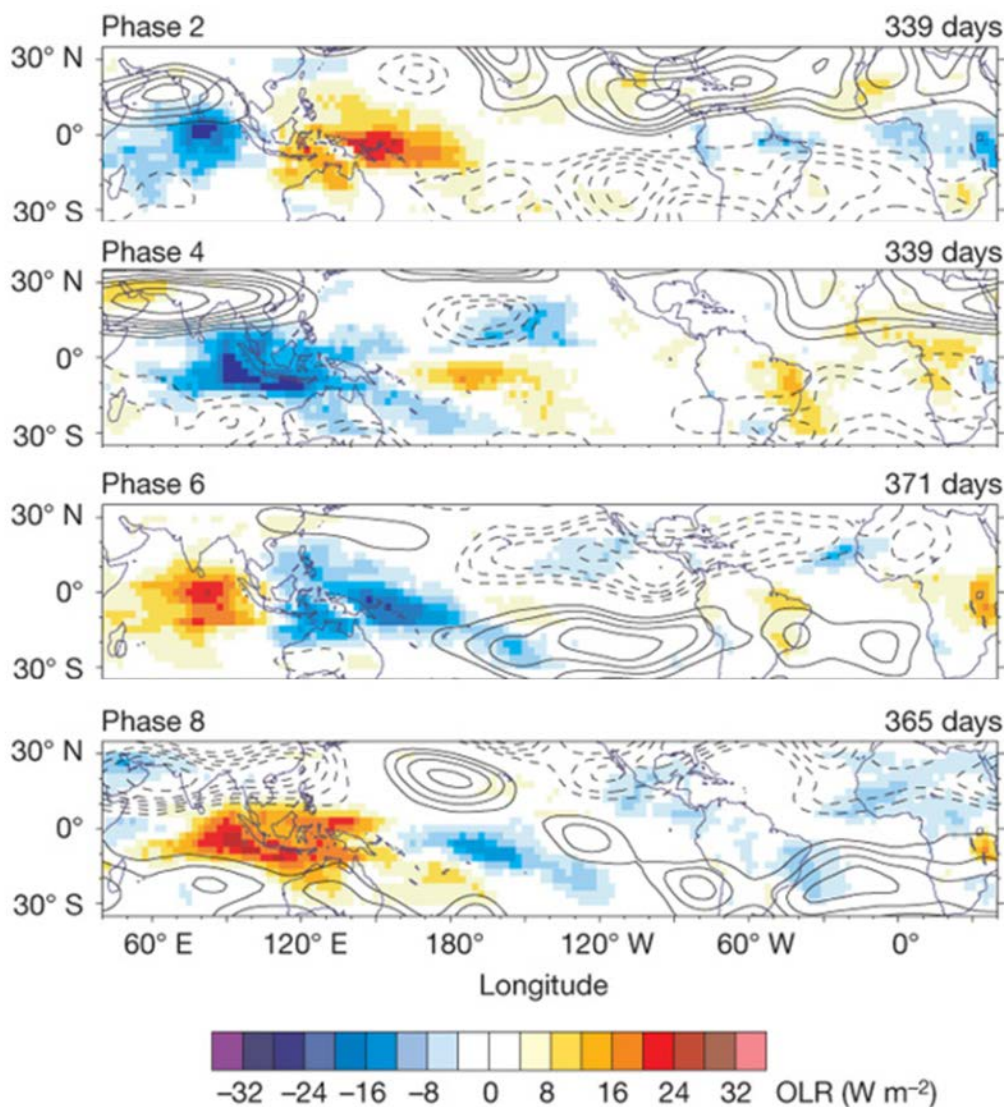


**Figure 1.1.** Composites of outgoing longwave radiation anomalies corresponding to even phases of the MJO. Positive anomalies indicate the MJO suppressed phase, and negative anomalies indicate the convectively active phase. Reprinted by permission from Macmillan Publishers Ltd: [Nature] (Intraseasonal interaction between the Madden-Julian Oscillation and the North Atlantic Oscillation), copyright (2008)

The MJO is an equatorial phenomenon most active from boreal late fall through early spring. Enhanced summer heating overland, and the resulting low pressure center, pulls convective activity northward off the Indian Ocean onto the Asian continent. The related summer monsoon, active June - September, dominates weather in the Indian

Ocean and Maritime Continent, seasonally overwhelming and weakening the equatorial eastward propagating mode of the MJO.

The MJO is the dominant mode of intraseasonal variability in the tropical Indian Ocean and the Western Pacific. As such, it has an important influence on global weather and climate systems, as well as socioeconomic significance for residents of affected regions. The MJO modulates weather in Southeast Asia and the Maritime Continent, with direct effects on coastal communities. In the Western Hemisphere, hurricane genesis in the Gulf of Mexico is four times more likely to occur during the MJO Westerly phase than the Easterly phase (Maloney & Hartmann, 2000).

Wheeler & Hendon (2004) developed an MJO index based on a multi-variable EOF regression using OLR anomalies, 850 mb winds, and 200 mb winds. The two leading principal components combined explain 30% of the variance of these variables. The two principal components of this analysis are called the Real-time multi-variable MJO indices (RMM1 and RMM2), which indicate the strength of the MJO signal, as well as the geographic location where deep convection is likely to be detected.

Figure 1.2 (courtesy of Jon Gottschalck, NOAA Climate Prediction Center) shows four time series of observed and modeled RMM1 and RMM2 indices. The indices were diagnosed from observations beginning on 2011 August 24 (Figure 1.2a) through November 11 (Figure 1.2d). Forecasts from weather models (yellow) extend 15 days beyond the most recent available observation (purple and orange) for each panel. Distance from the center represents the magnitude of MJO amplitude in the RMM indices, so points located outside of the circle indicate strong MJO amplitude. The single colored lines are observations, marked by the day of the month; thin yellow lines are

individual model predictions; the thick green line is the model ensemble average. 50% of the models fall within the dark grey area and 90% fall within the light grey area. Analogous to Figure 1.1, the regions where deep convection is expected are indicated on the sectors corresponding to different phases of the MJO. Phases 1 and 2, known as the initiation phases, generally exhibit deep convection over East Africa and the Western Indian Ocean. The MJO traverses the Indian Ocean and the Maritime Continent during phases 2-5. As the MJO progresses into the Central Pacific, the amplitude of the convective envelope tends to weaken over cool Central-Eastern Pacific SST; here the MJO propagates as a dry westerly wind burst. A reinvigoration of convection and westerly wind bursts are often observed over the warm SST in the Eastern Pacific Ocean.

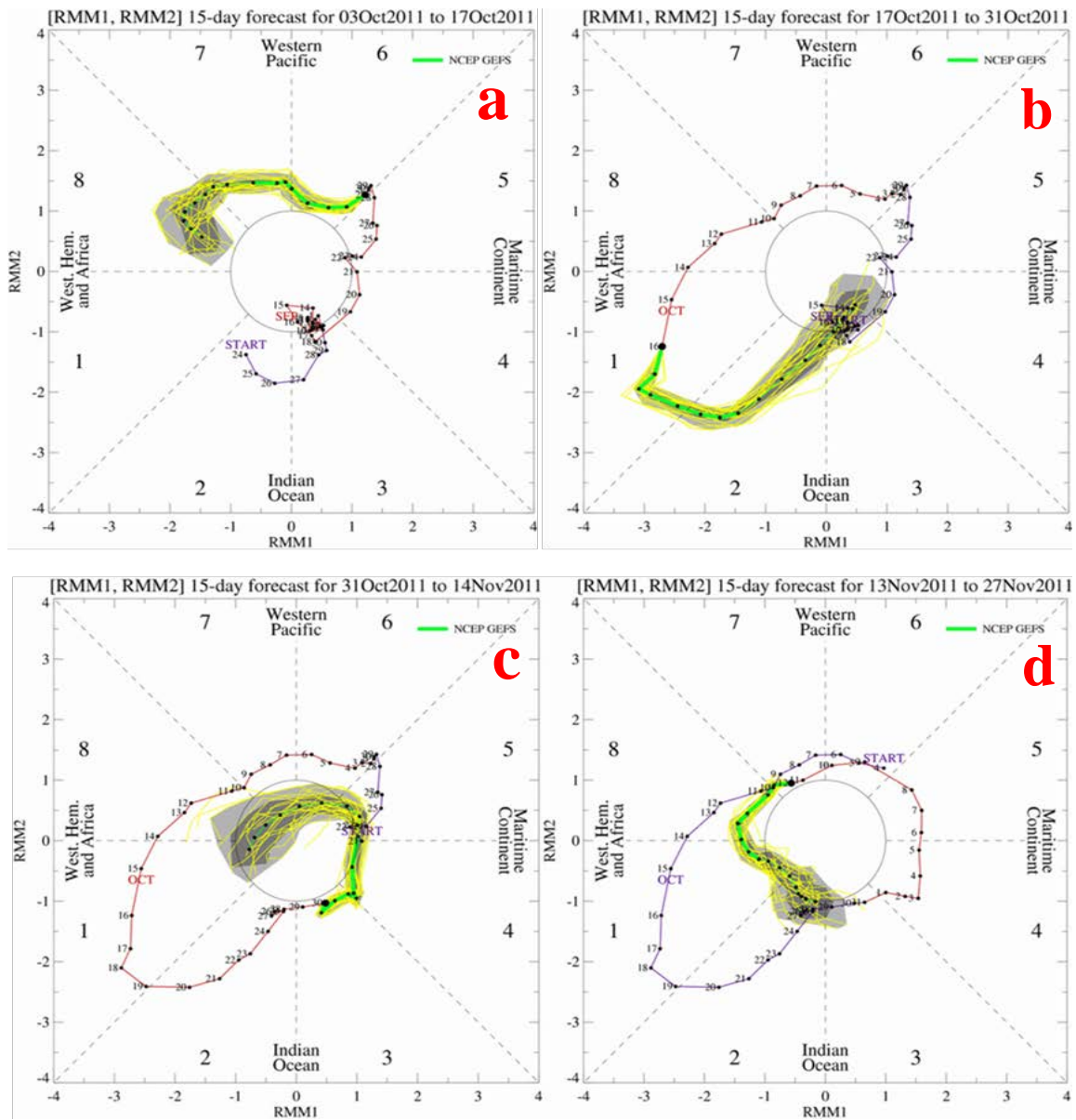


**Figure 1.2.** The MJO index indicates where the MJO is detected and the magnitude of the signal. Thin lines with numbers are observations and numbers are the day of the month. Yellow lines are individual model forecasts and the green line is the ensemble average. The grey area indicates 50% confidence, while the light grey is 90% confidence. Panels a-d show the progression of observed MJO indices from 2011 August 24 – November 12, along with successive 15 day forecasts from 2011 October 3 – November 27. [Figure credit: Jon Gottschalck, NOAA Climate Prediction Center].

The progression in Figure 1.2 shows the variability of models ability to forecast the MJO in these 4 realizations. The 15 day forecast in Figure 1.2a shows rapid progression

through phases 6-7, with increasing amplitude during week 1 followed by decreases in eastward propagation and amplitude in week 2 with MJO activity remaining in phase 8. Compared to the observed signal shown in Figure 1.2b, week 1 MJO activity was well captured by the models, but week 2 saw the opposite behavior than what was predicted by models. Amplitude and propagation speed increased well outside of the predicted range of all models, moving the MJO into phase 1 with uncommonly large amplitude. This indicates a limitation of models ability to accurately forecast MJO initiation. The 15 day forecast seen in Figure 1.2b correctly predicts the observed amplitude and propagation speeds seen in Figure 1.2c suggesting that once MJO activity is initiated, models are better able to predict MJO behavior. Comparing predictions and observations between Figures 1.2c and d illustrates a frequent underestimation of the MJO amplitude and a predicted decrease in the signal into the center of the circle (indicating no MJO activity). This is a common and documented problem with MJO forecast skill (Ling et al., 2014).

Improved MJO prediction could provide valuable information to the agricultural sectors in Asia, the Maritime Continent, and the Americas. The loss or degradation of crops due to strong late season precipitation related to the MJO can cause difficulties during harvest and spikes in agricultural prices globally (Donald, Meinke, Power, Wheeler, & Ribbe, 2004). Despite the well-known importance of the MJO, there remain substantial gaps in the understanding of physical processes that control MJO initiation and propagation speed. The 50 day MJO timescale portends improved 10-30 day forecasts, yet our lack of understanding of the processes generating the MJO presently

undermines our ability to predict it. Some numerical weather prediction models produce MJO-like disturbances and some do not, reducing our confidence in the predictions.

If general circulation models can reliably model the MJO, scientists will have higher confidence in the models and future climate projections. Schubert et al (2013) showed that MJO variance could increase significantly in the future. Maloney & Xie (2013) warned that the simulated MJO is highly sensitive to the spatial pattern of SST warming, which is largely uncertain as well. The IPCC AR5 working group 1 report on the MJO states that the highly variable skill of MJO simulation in climate models leads to low confidence in the future changes in MJO activity in a warmer climate. On a global scale, the RMM indices can assess the MJO simulation of GCMs with respect to amplitude, timing, and propagation speed (Ling et al., 2014). The European Center for Medium Range Weather Forecasting (ECMWF) forecasts of MJO activity are variable and often unskillful. In an evaluation of three MJO events observed in the Fall of 2011, forecast skill ranged from poor (correlations deteriorating to almost 0, and root mean square errors (RMSE) exceeding 1 standard deviation by a lead time of 10 days), to high (correlations remaining  $>0.8$ , and RMSE's  $<1$  for a lead time of 15 days) (Ling et al., 2014).

Vialard, et al., (2008) suggest the MJO is a coupled phenomenon with ocean and atmosphere coupling being important to general circulation model simulations. There are atmospheric models that produce MJO-like disturbances without air-sea coupling, which suggests that surface interactions may not be essential to the MJO. On the other hand, coupled dynamical models often improve the skill of MJO prediction, suggesting that air-sea interactions may be important, if not solely responsible for MJO activity. Accurate

understanding and depiction of the physics of air-sea interactions will likely improve climate and weather predictions on intraseasonal timescales and may improve the accuracy of 10-15 day forecasts.

The 5 m/s eastward propagation speed of the MJO is slower than can be explained by classical atmospheric dynamics. Several theories exist to explain the slow propagation speed, though none are universally accepted. Convectively coupled Kelvin waves are eastward propagating, but they occur with a shorter period and propagate ~3 times faster than the MJO (Straub & Kiladis, 2002). The theory that the MJO is a damped Kelvin wave has become unpopular since Kelvin waves are distinctly present during the MJO (Maloney & Sobel, 2004). A different theory involves the evaporation-wind feedback. Enhanced latent heat flux from stronger winds in background easterlies east of the main convective cell could cause the disturbance to propagate slowly eastward (Neelin, et al, 1987). Observations of mean *westerly* winds and maximum evaporation slightly west of the convective center in the region of strongest westerlies challenge this theory. The physical mechanisms for MJO propagation thus remain a scientific mystery.

During boreal winter, the net heat flux is typically positive, i.e. the ocean is warming, due to incoming solar radiation. However the convectively active phase of the MJO leaves a wake of anomalously cool SSTs as enhanced wind-driven mixing deepens the ocean mixed layer, and large negative net heat fluxes cool the upper ocean. Enhanced latent heat flux due to anomalously strong winds, large air-sea temperature differences, and weak insolation due to clouds during deep convection are found in the convectively active phase. With incoming solar radiation diminished, net outgoing longwave radiation, and latent and sensible heat flux cool the surface of the ocean. The ocean may act as a

heat capacitor between the suppressed and active phases, storing energy in the upper few tens of meters. With the help of strong westerly winds bursts, this heat is released to the atmosphere via enhanced evaporation, which may help to sustain the MJO in the active phase. Diminished latent heat fluxes over land leads to observed weakening of the MJO over the Maritime Continent (Maloney & Sobel, 2004). As the MJO signal crosses into the Western Pacific, where the mean SST is maximum, enhanced latent heat flux can again reinvigorate the MJO signal.

Questions regarding the initiation, propagation, and general dynamics of the MJO form the impetus for the intensive TOGA-COARE and DYNAMO field campaigns, summarized below, to gain insight into the governing physics of the MJO.

### **1.3 TOGA-COARE**

The Tropical Ocean Global Atmosphere (TOGA) Coupled Ocean Atmosphere Response Experiment (COARE), conducted from 1992 November 15 to 1993 February 15, was an intensive multi-scale effort to study the complexities of the dynamically coupled processes in the Western Pacific warm pool. The primary research goal of TOGA-COARE was to better understand air-sea coupling in the Western Pacific warm pool on intraseasonal to interannual time scales.

Figure 1.3 shows the Intensive Flux Array, including 4 buoys and 2 ships, centered east of Indonesia between  $150^{\circ}$  E and  $160^{\circ}$  E and ranging from slightly north of the equator to approximately  $5^{\circ}$  S. This region is of dynamical importance to the El Niño-Southern Oscillation (Webster and Lukas, 1992). In addition, weather and air-sea interaction over and within the warm pool respond to intraseasonal MJO events originating in the Indian Ocean (Lau and Chan, 1988).

During the Intensive Observation Period (IOP) of TOGA-COARE, researchers observed the passage of 2 distinct westerly wind bursts characteristic of the MJO. The team studied atmospheric and oceanic processes broadly using large scale data from satellite and reanalysis products, as well as micro-scale observations such as in situ high resolution bulk flux systems on buoys and covariance flux systems on ships. Rawinsonde data provided information on the vertical structure, and heating and cooling processes in the atmosphere. The TOGA-COARE dataset remains relevant to the scientific community over 2 decades later. This thesis uses fluxes measured aboard the research vessel *Moana Wave* to evaluate spatially resolved gridded flux products.

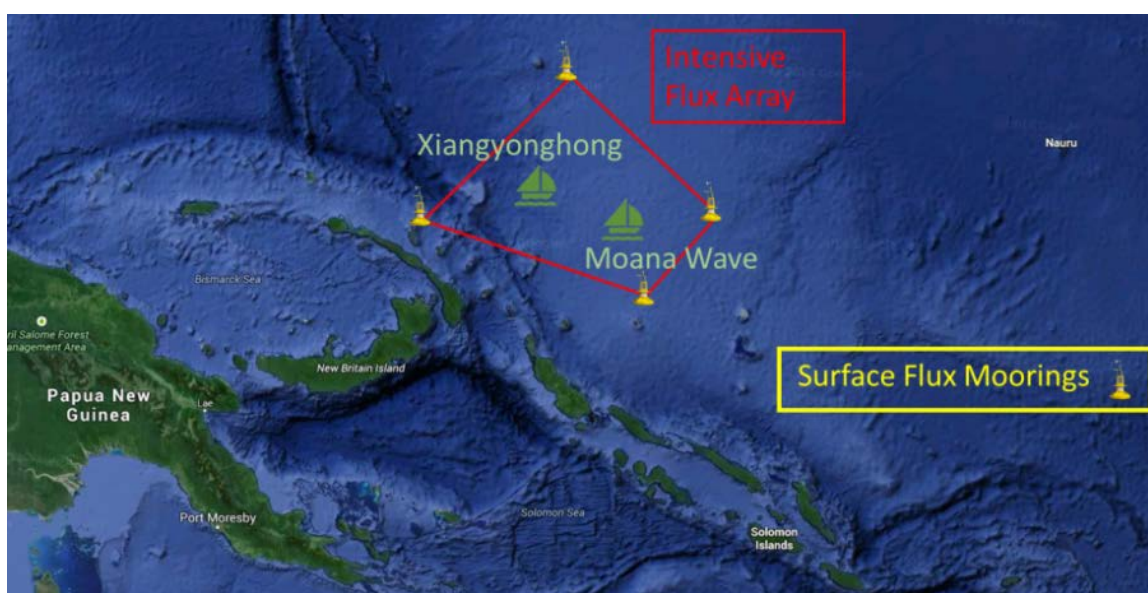


**Figure 1.3.** The intensive Flux Array included 4 buoys, and R/V's Xiangyonghong and *Moana Wave*.

One of the many prominent scientific results of TOGA-COARE was the development of the COARE bulk aerodynamic flux formulation from ship data collected on the *Moana Wave* (Fairall, et al. 1996b). The COARE algorithm was designed to match covariance flux estimates from TOGA-COARE. Air-sea fluxes are parameterized as functions of air temperature, sea surface temperature, relative humidity, solar and infrared

radiation, and wind speed. COARE introduced several new physical parameterizations to more accurately estimate turbulent fluxes, including warm layer and cool skin parameterizations that estimate an interfacial temperature (Fairall et al., 1996a) from subsurface ocean temperature gradients due to the effects of radiative warming and surface cooling. To date, COARE version 3.0 (Fairall et al., 2003) is a widely used bulk flux algorithm for computing air sea fluxes. This thesis uses COARE version 3.5 (Edson et al., 2013). A detailed description of COARE, and the warm layer and cool skin parameterizations will follow in chapter 2.3, and 3.3.

## 1.4 DYNAMO

In an effort to advance our understanding and representation of the MJO in GCMs, researchers carried out the DYNAmics of the Madden Julian Oscillation (DYNAMO) field campaign (2011 October 1 to 2012 January 15). DYNAMO was an international collaboration focused on meteorological and oceanographic processes of the MJO in the central Indian Ocean region. DYNAMO offered an exciting opportunity to observe processes in the MJO in detail for several months. During the DYNAMO IOP, researchers established an impressive array of data collection facilities in the Indian Ocean, including two ships, three moored buoys, three island stations, and an aircraft. The intent was to observe MJO initiation in the western and central Indian Ocean region. Figure 1.4 shows a map of the DYNAMO array. Waters west of 70° E are pirate-infested, therefore, observations were confined to the central Indian Ocean. The United States research vessel *Roger Revelle*, kept station at 0° N, 80.5° E, while the Japanese research vessel, *Mirai*, maintained 8° S, 80.5° E. A radar superstation hosted four radars and launched 8 radiosondes per day from Addu Atoll in the Maldives. Malé and Diego Garcia

Islands also provided radiosonde launch sites, and Diego Garcia hosted as home base for the National Oceanic and Atmospheric Administration (NOAA) P-3 aircraft.

Researchers purposefully withheld some data from this experiment from assimilation into reanalysis and model products. These independent observations are important for assessing the bias and root mean square error of reanalysis-based estimates of surface meteorological variables. These measurements can also help to evaluate the representation of air-sea interactions, the hydrologic cycle, ocean dynamics and other physical processes in the models and reanalysis products.

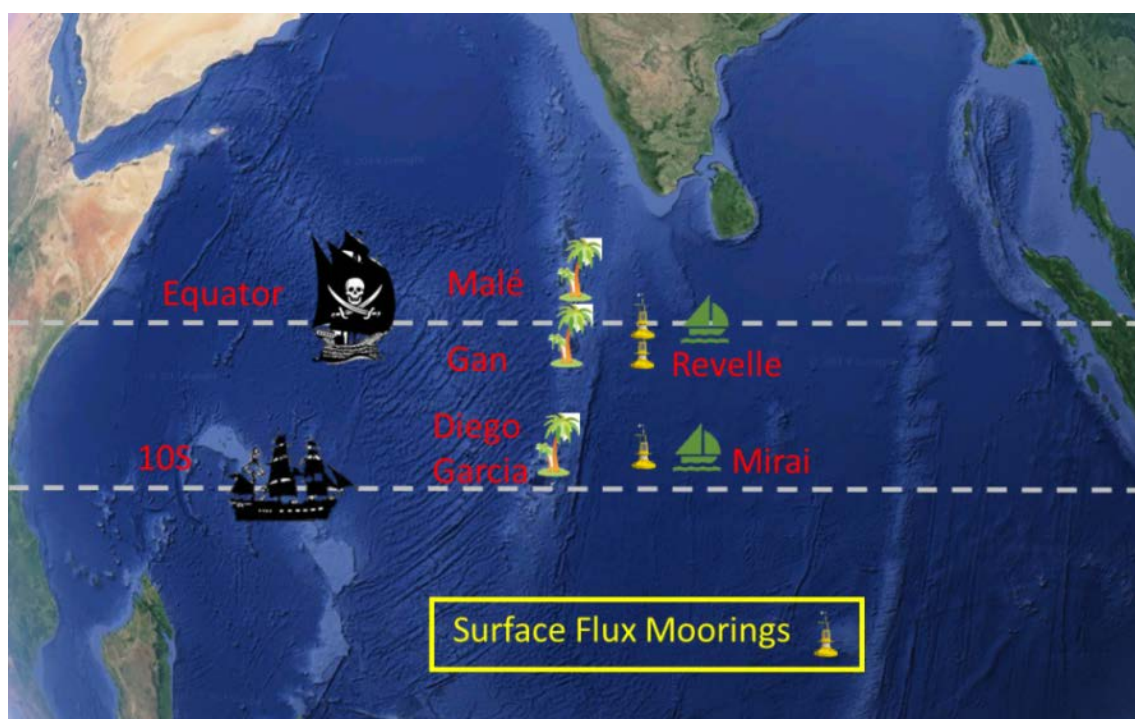


**Figure 1.4.** the R/V *Revelle* and *Mirai* station and APL buoy locations are shown. Also the island stations on Male, Gan, and Diego Garcia Islands are shown. Pirate infested waters prevented measurements off the coast of Somalia where MJO genesis is thought to occur.

Aboard the R/V *Revelle*, the Oregon State University (OSU) Ocean Mixing group conducted oceanographic research, performing round-the-clock ocean turbulence

profiling down to 300 m depth off the fantail using a specially designed ocean turbulence probe. Additionally, a temperature-conductivity chain deployed off the bow of the ship continuously resolved the upper ocean heat and salinity profile from the surface to ~20 m. A floating temperature probe measured near surface temperature, and infrared cameras measured the ocean skin temperature. Several research teams conducted atmospheric measurements on a multitude of scales. Large scale sampling included 8 rawinsondes per day, a wind profiler, W-band cloud radar, C-band precipitation radar, ceilometer, and scanning LIDAR system. High resolution direct covariance surface flux data was collected on the ship's forward mast. A total of 7 rain gauges mounted around the ship collected and estimated rainfall while the ship was stationary. Combined, these data sets shed light on the organization and intensity of convective cells, the upper ocean heat budget, and surface fluxes throughout the evolution of MJO events. In this thesis, DYNAMO data is used to quantify the turbulent exchange of heat, moisture and momentum at the air-sea interface during the passage of a few MJO cycles over the central Indian Ocean.

## **1.5 RESEARCH GOALS**

Turbulent fluxes can be computed from 10 or 20 Hz in situ data using direct covariance methods. Bulk fluxes can be computed from bulk variables averaged over temporal scales ranging from minutes to days, or over spatial scales ranging from in situ to hundreds of kilometers. Each of these scales provide a distinct and valuable scientific perspective. In this thesis, fluxes are computed using the direct covariance method with high precision in situ data from the OSU flux system deployed on the R/V *Roger Revelle*

during the DYNAMO field campaign. Additionally data collected during the DYNAMO and TOGA-COARE field campaigns are used to compute bulk fluxes with the COARE version 3.5 bulk aerodynamic algorithm. Goals of this thesis are to use these data sets to assess and potentially improve commonly used gridded flux products to quantify the spatial variability in the flux fields within the DYNAMO array, and to assess the importance of surface fluxes to the MJO. Steps taken toward this goal are summarized below:

- Describe in detail the OSU flux measurement system, data quality control, and direct covariance computation method used to compute OSU direct covariance fluxes.
- Compare direct covariance and bulk fluxes computed from the OSU, NOAA Physical Science Division (PSD), and University of Connecticut (UConn) flux systems.
- Assess the skill of gridded flux products with respect to independent in situ measurements collected during TOGA-COARE and DYNAMO. Estimate errors in gridded fluxes by comparing the mean, standard deviation, and correlation with the above in situ observations.
- Quantify the error in gridded products near and far from assimilated data sources using independent observations.
- Quantify the error introduced by substituting a 1 m ocean temperature for the ocean interface temperature using 10-minute resolution data collected during the DYNAMO cruise.
- Assess two new methods to include diurnally varying ocean interface temperature fluctuations in daily average fluxes: (1) a simple solar model approximates diurnally varying solar radiation from the daily average, and (2) tabulated values

of corrections to either the SST, or to the fluxes, account for the net effect of using a 1 m ocean temperature when computing fluxes.

## **CHAPTER 2:      TURBULENT FLUXES MEASURED IN DYNAMO**

Air-sea fluxes of momentum, sensible heat, and latent heat affect atmospheric convection and upper ocean thermodynamics and dynamics. In the marine boundary layer, turbulent fluxes are the dominant form of energy transfer from the ocean to the atmosphere. Turbulence is wind- and/or buoyancy-driven and far more effective than conduction and molecular diffusion at transporting heat, except very near the ocean surface. Strong winds enhance latent and sensible heat flux, and surface stress transfers momentum to the upper ocean. Buoyancy can drive turbulent eddies regardless of the wind, but the turbulent kinetic energy and net heat exchange is considerably greater when wind shear drives turbulence. In the absence of winds, buoyancy drives convection in the atmosphere through density gradients caused by sensible heat flux and evaporation.

The marine atmospheric boundary layer (MABL) is often turbulent and is capped by a statically stable layer of air (i.e. a temperature inversion). The MABL depth governed by the inversion height is variable in time and space, ranging from tens of meters in strongly statically stable situations, to several kilometers in highly convective conditions (American Meteorological Society, glossary of meteorology). Figure 2.1 shows a cartoon of the marine atmospheric boundary layer divided into 4 sub-layers. Within the surface molecular layer ( $O$  1 mm) the frictional no-slip boundary condition constrains the surface currents to have the same velocity as the air at the interface. In this

layer, the mean vertical velocity is equal to zero because air does not cross the interfacial boundary, though non-zero fluctuations exist in the presence of waves. Temperature and moisture differences at the interface drive diffusive heat exchange across the air-sea boundary. The surface layer lies directly above the molecular layer and comprises ~10% of the marine boundary layer. Data collected from ships and buoys sample fluxes from within this layer, where fluxes are nearly constant with height, and the dynamics are well parameterized by Monin Obukhov Similarity (MOS) theory (Monin and Obukhov, 1954). MOS relates gradients to fluxes and universal functions of a non-dimensional height scale. A logarithmic velocity profile is assumed for the special case of neutrally stable conditions within the surface layer, as per the “law of the wall” (Stull, 1988). The MOS stability functions are then used to describe modification of the log profile due to stratification and buoyancy in stable and unstable conditions, respectively. The mixed layer makes up ~80% of the marine atmospheric boundary layer and is characterized by weak vertical gradients due to strong turbulent mixing. The stable inversion layer, with a reversed gradient of temperature, occupies the upper 10% of the marine boundary layer, and caps the mixed layer. The stable nature of the inversion layer often causes negative buoyancy fluxes within the layer. (Fairall, et al., 1997).

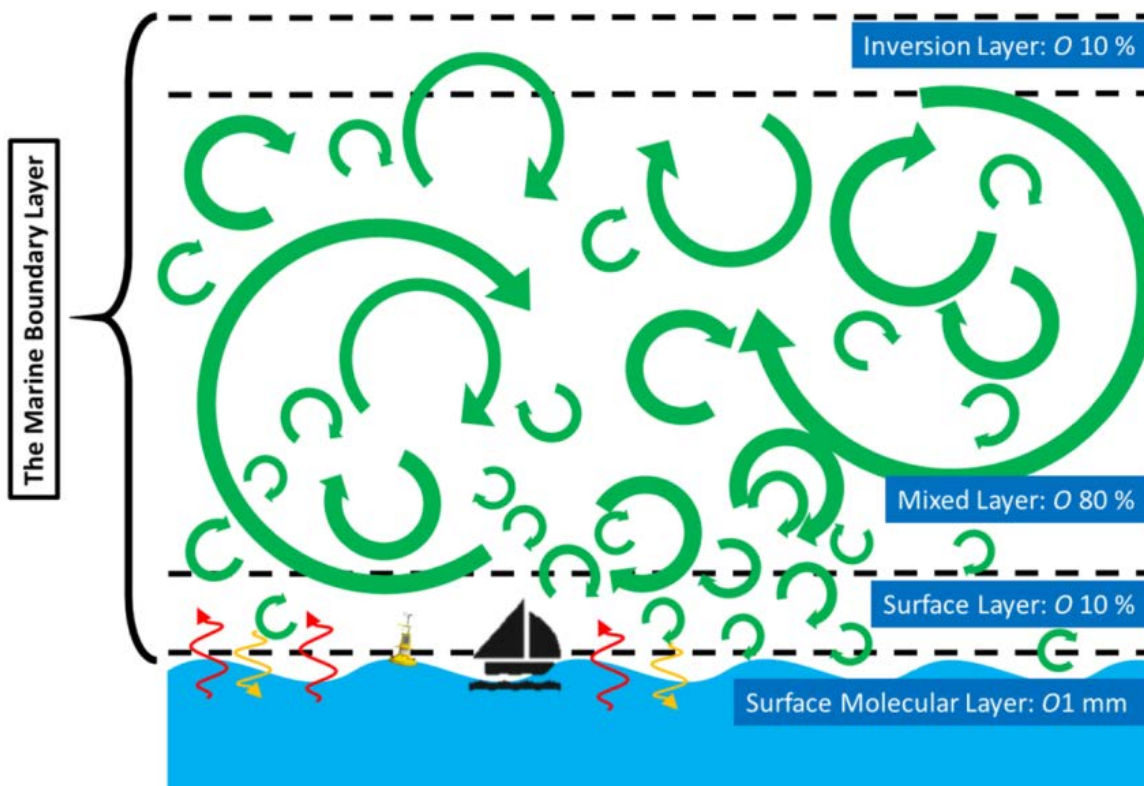


**Figure 2.1** Marine Atmospheric Boundary Layer (MABL): the surface molecular layer is a thin film in direct contact with the surface of the ocean. The turbulent boundary layer, ~ 10% of the MABL, is where ships and buoys make measurements. The mixed layer, on the order of 80% of the MABL, is well mixed due to developed turbulence. The inversion layer is characterized by reverse gradients and inhibits mixing beyond the MABL.

Turbulent air-sea fluxes of momentum, sensible heat, and moisture are the boundary conditions to the atmosphere and ocean, through which atmosphere-ocean interaction occurs. Turbulent fluxes of heat and moisture are important to surface water flux (evaporation minus precipitation) in the hydrologic cycle, and to the vertical structure of the atmosphere.

In this chapter, a direct flux measurement technique known as Direct Covariance or Eddy Correlation (hereafter EC), and a bulk approximation based on flux gradient similarity theory are described. EC methods are covered in sections 2.1 and 2.2. The

reader is referred to the Appendix for a complete description of the OSU instrumentation, deployment configuration, wiring, data collection procedures and quality control scheme. Bulk methods are described in section 2.3, including a qualitative description of COARE version 3.5, the bulk flux algorithm used by OSU. In the Results section (2.4) I compare fluxes computed with EC and bulk methods using data from the OSU system when available. Finally, I compare fluxes from three flux measurement systems deployed on the R/V *Revelle*.

## 2.1 EDDY CORRELATION FLUXES

### 2.1.1 Theory

Eddy Correlation measures turbulent fluxes directly by resolving turbulent fluctuations. A time varying scalar  $x(t)$  can be decomposed into the sum of the mean,  $(\bar{x})$ , and the perturbation  $x'(t)$  of the scalar so that  $x(t) = \bar{x} + x'(t)$ . The correlation (or covariance) of two time varying scalars follows as:

$$\overline{xy} = \bar{x}\bar{y} + \overline{x'y'}$$

where the terms in which mean and perturbation variables multiply are zero because the mean of the perturbation is zero over the averaging interval (Foken & Nappo, 2008). The mean is relative to the averaging interval, and the turbulent flux is attributed to the covariance or correlation of the perturbation variables  $\overline{x'y'}$ . In this definition, the variables  $x$  and  $y$  can represent a host of variables including wind velocity ( $u, v, w$ ), moisture, temperature, and trace gas concentrations.

The Eddy correlation methods characterize the kinematic vertical fluxes of heat, moisture and momentum as the instantaneous cross product of the perturbation vertical

velocity  $w'$  with perturbations in air temperature, moisture and horizontal wind speed respectively. Dynamic fluxes are equal to the kinematic fluxes scaled by density of air ( $\rho_{air}$ ); with latent heat scaled also by the latent heat of evaporation ( $\lambda$ ), and sensible heat scaled by  $C_{pa}$ , the heat capacity of air at constant pressure. Sensible heat (SHF), latent heat (LHF), and momentum flux (M) are defined as:

$$\text{SHF} = C_{pa}\rho_{air}\overline{w'T'} [W/m^2]$$

$$\text{LHF} = \lambda\rho_{air}\overline{w'q'} [W/m^2]$$

$$\text{M} = \rho_{air}\overline{w'u'} [N/m^2]$$

The fluxes thus depend on the covariance of fluctuations within the average indicated by the overbar. If the average is done over time, the choice of the averaging interval, hereafter  $\tau$ , may affect flux estimates. Eddy populations evolve throughout the day with changing stability regimes and convective conditions. The EC method can accurately resolve energy flux in a system so long as the changes of the emergent properties of the ensemble being sampled are relatively small; such a system is considered quasi-steady-state. Choosing  $\tau$  too large may give rise to averaging over non-quasi-steady-state conditions, which can lead to systematic and/or random bias in flux estimates. Under low wind conditions, eddies pass by a single sensor slowly and choosing  $\tau$  too short leaves large, stationary eddies systematically under-sampled.

Furthermore,  $\tau$  limits the maximum size of eddies that can be sampled. Taylor's Hypothesis relates variations in time and space through an average velocity (Foken and Nappo, 2008), such that  $T_e=L_e/U$  where  $L$  is the characteristic length scale of passing eddies and  $U$  is the mean translation velocity. Large eddies have larger  $L$  and take longer

to be advected through the sensors. Since large eddies contain the most energy, it is desirable to choose  $\tau$  long enough to ensure proper sampling of boundary layer scale eddies. When eddies are large, the choice of averaging window is limited (above) by non-stationary transitions such as passing fronts, and secular trends such as changes in solar forcing near sunrise and sunset. Choosing  $\tau$  too small may result in substantial underestimation of fluxes because the large eddies do not fit in or are inadequately sampled within the window. Conversely, small eddies have small  $L$  so  $L/U$  is small. These eddies are easily sampled as long as  $\tau$  is not too short.

The ability to sample small eddies is limited by the finite sampling path of the instruments. The sampling path can be either the distance between transducer heads of the sonic anemometer, which measure wind velocity; or the distance between the infrared source and detector of the Infrared Gas Analyzer (IRGA), which measures water vapor for LHF. Additionally, the ability to resolve the contribution of the smaller eddies is limited by the separation distance between the sonic anemometer and the IRGA. If the sonic anemometer samples an eddy but the IRGA samples it with a different phase or misses it entirely, the vertical velocity perturbation associated with that eddy will not be correlated with its water vapor perturbation, and LHF will be underestimated. Though eddies close to the ground are smaller, shipboard flux systems are generally far enough ( $\sim 10$  m) above the sea surface, that turbulence scales are large enough to be well captured by the path and separation of the sensors, even for moderate ( $\sim 1$  m) sensor separation.

### 2.1.2 Assumptions

Calculating eddy correlation fluxes requires that three strong assumptions are met within the averaging window: Horizontal homogeneity, stationarity, and ergodicity. Additionally it is assumed that there exists a region of the atmosphere in which vertical gradients of fluxes are negligibly small, so that within this region the fluxes are not sensitive to the measurement height.

Horizontal homogeneity requires that the surface over which fluxes are measured is continuous and homogeneous in the direction of prevailing winds. This requirement excludes sampling internal boundary layers which may be induced by changes in local surface properties. Normally, this is not an issue over the open ocean with the possible exception of the strong sea-surface temperature or current fronts associated with, e.g., western boundary currents. Unfortunately, changes in the local surface can also include contamination due to flow distortion by the measurement platform and supporting structures. However, the impact of flow distortion can be minimized through appropriate placement of sensors, e.g., on the bow mast of the research vessel. When these steps are taken, horizontal homogeneity over the open ocean can be assumed, and the eddies sampled are then representative of the ensemble generated by local conditions.

The assumption of stationarity governs the choice of averaging interval, and requires that the system may be approximated as quasi-steady-state. Though the state of the atmosphere changes throughout the day due to sunrise, sunset, passing fronts, and changes in convective conditions, it is often possible to partition the day into a series of windows when the flow is quasi-steady-state and approximately satisfies the requirement of stationarity. It is desirable to choose an averaging interval that is at most  $1/3$  of the

timescale of non-stationary changes to the system. The choice of  $\tau=10$  minutes is appropriate for mesoscale changes in the system that occur over timescales of 30 minutes or longer. Transition periods are often non-stationary, and stationarity tests should be done to exclude non-quasi-steady-state events.

In the third assumption, Boltzmann's ergodic hypothesis states that the time average of a long enough time series is representative of the statistical ensemble of conditions of the system (Von Plato, 1991). For the example of sampling turbulence, it is not possible to sample all eddies responsible for air-sea fluxes over a region of the ocean. Eddies randomly pass the sensor and are recorded in the time series. Over a sufficiently long time series the sampled population of eddies is assumed to be representative of the true population of eddies, so that covariances in the time series accurately approximate fluxes in the region.

Ship-based measurements meet the horizontal homogeneity and ergodicity requirements because the sea surface is continuous and homogenous in all directions, resulting in measured eddy covariance fluxes that are representative of local fluxes in the region. The caveat is that flow distortion must be minimized by deploying the sensors at optimal locations. However, even with these requirements met, the requirement of stationarity needs to be carefully addressed in the pre-processing.

## **2.2 EXPERIMENTAL SETUP**

As part of the DYNAMO Intensive Observation Period, three independent turbulent flux measurement systems belonging to the University of Connecticut (UConn), NOAA Physical Science Division (PSD), and OSU air-sea interaction groups were

deployed on the R/V *Revelle*. The UConn and PSD systems have been tested and honed to meet the needs of ship based flux measurements since TOGA-COARE in 1992, while the DYNAMO cruise was the maiden voyage for the OSU flux system.

Ship-board flux systems are comprised primarily of a 3-axis sonic anemometer, which measures the wind components in three dimensions and speed of sound; 3-axis linear accelerometers and angular rate sensors, which measure the earth relative ship motion; and an infra-red gas analyzer, which measures the specific humidity and mixing ratio of moist air. The speed of sound can be readily converted to sonic temperature, which closely approximates the virtual temperature necessary to compute the buoyancy flux. This conversion is often done internally and sonic temperature is output by sonic anemometer. The combination of virtual temperature and specific humidity provide estimates of sensible and latent heat fluxes. These instruments were mounted nominally 17 m above mean sea level on the forward mast of the *Revelle*.

OSU used a CSAT3 sonic anemometer to measure the travel time of sound in three orthogonally oriented dimensions, and the sonic air temperature. A pulse of sound is sent to a receiver and the time elapsed between transmitting and receiving the signal is measured. The spacing of the transducer heads is known, and the travel time of sound is measured in 3 directions, from which the speed of sound and the temperature are calculated. The difference in travel time between the three directions gives three dimensional wind components. Shorter travel times indicate winds traveling in the direction of the sound pulse, and longer travel times correspond to winds against the direction of the pulse. At the time of this experiment, the CSAT3 had the shortest path-length and least amount of path-averaging of any available sonic anemometer on the

market, with 10 cm between transducer heads. One source of error in the sonic anemometer data is water accumulation on the sensor heads during periods of heavy precipitation. The CSAT3 sonic anemometer has small mesh wicks attached to each transducer head which pull moisture off the sensors. This helped to reduce noise in sonic wind and temperature estimates, but heavy precipitation still compromised high frequency wind estimates with unphysical spikes.

The LI-COR7500 Infrared Gas Analyzer (IRGA) uses an optical detection method whereby a beam of light in two wavelength bands (reference and absorbing) is directed through the air and received by a sensor ~15 cm away. The absorption of the beam by water vapor and CO<sub>2</sub> along the path is measured by passing the absorbing wavelengths through appropriate filters. The amount of absorption is then used to determine the concentration of each constituent. Over time, the sensor heads collect dust, soot, salt, and hygroscopic aerosols which obscure the signal. There were two mitigation strategies in place for this problem: the IRGA has a built-in Automatic Gain Control (AGC), which amplifies the signal as the sensor gets dirty based on the reference wavelength. Additionally, the sensors were sprayed with water once per day to clean the heads. The IRGA does not function during cleaning, or during rain events as any water on the optics overwhelms the absorption by water vapor or CO<sub>2</sub>.

Other instrumentation used for EC flux calculations included a Gladiator vertical gyroscope/GPS accelerometer that measured the ship's translational acceleration and angular velocity in three dimensions on the forward mast; a Vaisala HMP155 humidity and temperature sensor, that measured air temperature and relative humidity; and an R.M. Young barometer that measured atmospheric pressure.

### 2.2.1 Eddy Correlation Flux Calculations

The processing of eddy correlation flux data proceeds along the following sequence. First, raw data passes through three distinct quality control (QC) phases. Quality control phases 1 and 2 were designed specifically to meet the needs of the OSU EC flux measurement system. In these phases the raw data is filtered for unphysical values and sensor failures. Phase 1 and 2 QC are described in detail in the appendix.

Phase 3 QC is performed in the main flux program prior to all other processing, and has three criteria for excluding data. Specifically, fluxes are not computed during times when:

- a) The ship heading changes substantially; large changes in the ship's heading indicate significant maneuvers that compromise the high frequency measurement of covariance variables.
- b) Large unphysical CO<sub>2</sub> spikes in the IRGA data. These spikes may indicate contamination by ship exhaust, rain, or washing. In light or meandering winds, or winds from the stern, ship exhaust can reach the flux system and contaminate CO<sub>2</sub> and H<sub>2</sub>O measurements. This contamination compromises latent heat flux estimates.
- c) The ship-relative winds are in excess of 60° port and 90° starboard of the bow. This condition pertains to flow distortion around the ship, a difficult problem associated with ship-based EC flux measurements. These relative wind directions are chosen to minimize this effect as the OSU system was deployed on the starboard side of the bow mast.

Flow distortion comes in two scales: turbulence-scale contamination of winds due to interference of the mast and instrumentation mounted on the mast; and large-scale laminar deflection of air over the ship superstructure. The first has a QC solution, while the second has a data processing solution described in section 2.2.1.1b.

Contamination due to blockage by instrumentation and the mast varies primarily with wind direction. During the experimental setup, the OSU, PSD, and UConn sonic anemometers were all mounted so they were least obstructed by the mast and other sensors. As winds are deflected over the ship, a vertical velocity is induced which scales with the wind speed. If the winds are from an unfavorable direction, air is deflected differently by nearby obstacles, and the ratio of vertical velocity to the wind speed changes. To determine the acceptable range of wind directions, the measured vertical velocity is divided by the mean horizontal wind speed (Figure 2.2). The mean vertical velocity is  $\sim 0.1$  of the mean wind speed between  $-60^\circ$  (port) and  $90^\circ$  (starboard). Deviations of the ratio outside this range indicate contamination due to blockage. In the QC of eddy covariance data, winds from unfavorable directions, specific to each anemometer, are filtered out. The analysis found that winds from port were substantially more compromised for the OSU system, as expected since this sonic was mounted to the starboard. Based on Figure 2.2, the wind directions are limited to  $60^\circ$  port, and  $90^\circ$  starboard of the bow.

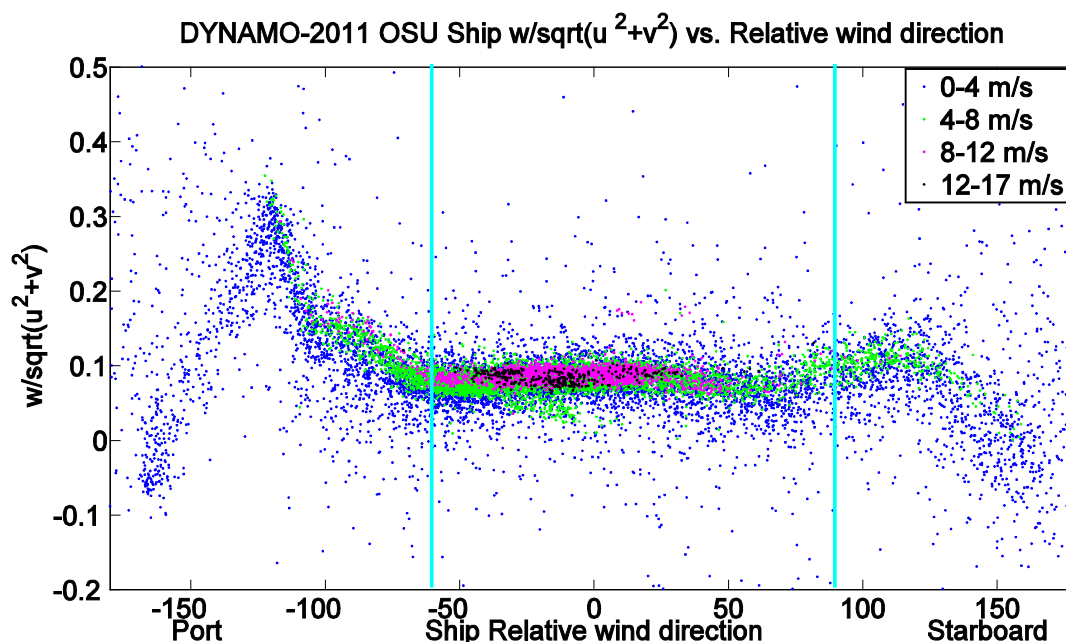


**Figure 2.2** Vertical wind speed divided by horizontal wind speed versus wind direction, binned by horizontal wind speed.

### 2.2.1.1 Data Corrections Required for EC Flux Calculations

#### a) Motion Correction

The covariance fluxes themselves are in principle quite simple, however, marine-based flux measurements are complicated by platform motion that appears in the wind measurements. High frequency accelerometers and angular rate sensors mounted near the sonic anemometers track translation and angular rotations of the ship platform near the anemometers. It is essential that the accelerometer and rate sensor measurements are synchronized with the sonic anemometer wind measurements, so that the appropriate high frequency ship motion is added to the corresponding wind measurement. The platform motion at the anemometer sampling volume is provided by the integrated accelerations and angular rates measured by the Gladiator. The mean translational and rotational motions are then added to the measured anemometer winds. In this way, the

flux processing program removes the platform motion from each hour of data using a series of functions written in MATLAB by James Edson:

- “angles.m” computes the angles needed for the transformation matrix between the accelerometer and the sonic anemometer.
- “accels.m” computes the linear platform velocity ( $uvw_{plat}$ ) from accelerations, low frequency drift is removed, and GPS speeds are added to platform velocities to estimate the ship motion relative to Earth.
- “sonic.m” corrects the measured sonic velocities by adding the angular velocities and the ship motion.

Figure 2.3 shows a short 17-second sample of measured sonic anemometer wind speed, platform velocity, and motion-corrected winds for  $u$ ,  $v$  and  $w$ . The measured vertical velocity,  $w$ , is anti-correlated with the platform velocity ( $w_{plat}$ ). Corrected  $w$  has no periodic low-frequency signal correlated to ship motion. Horizontal wind components  $u$ , and  $v$  have much more variability so that measured winds are weakly anti-correlated to platform velocity. Measured winds and corrected winds remain strongly correlated.

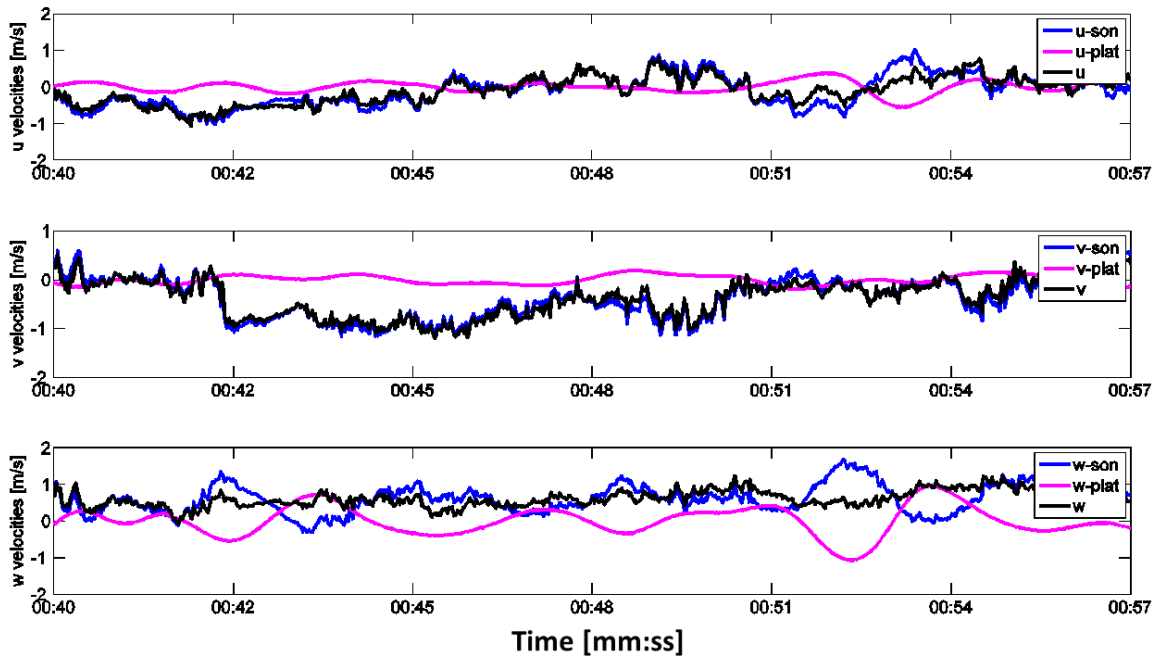


**Figure 2.3** Motion correction applied to  $u$ ,  $v$ , and  $w$ , where  $u$  is positive toward the bow,  $v$  is positive to the starboard, and  $w$  is positive up. Blue lines are the measured velocities as seen by the anemometer, pink lines are the platform velocities from the integrated platform accelerations, and black lines are the corrected wind vectors.

### *b) Rotate into the Mean Wind*

Air deflected around the main superstructure of the ship is assumed approximately laminar. According to the boundary condition at the air-sea interface, mean vertical velocity should be close to zero near the surface. As seen in Figure 2.4, flow distortion induces a persistent vertical velocity, the magnitude of which scales with the wind speed.

The ship was pointed into the mean current for ocean turbulence profiling on the fantail. Since the winds drive the upper ocean currents, the current was often aligned with the mean wind, though with the passage of some atmospheric fronts and strong storms, inertial persistence of the ocean currents caused systematic offsets in wind and current



*c) Detrending high-rate variables in the flux window*

Windows with abrupt changes or large tendencies in short periods should be excluded because they violate the assumption of stationarity. Small trends are still sometimes present in the data due to low-frequency variability. Detrending perturbations before computing covariances filters out some of the low frequency variability, and is not universally practiced by all who estimate eddy covariance fluxes. Figure 2.5 shows twenty minutes of winds detrended (blue) and with the mean only removed (pink); the differences are small, and smallest for  $w'$ , the variable used in all vertical covariance fluxes, suggesting that the covariances should be relatively insensitive to the choice to detrend. Differences induced due to this choice are discussed in section 2.4.

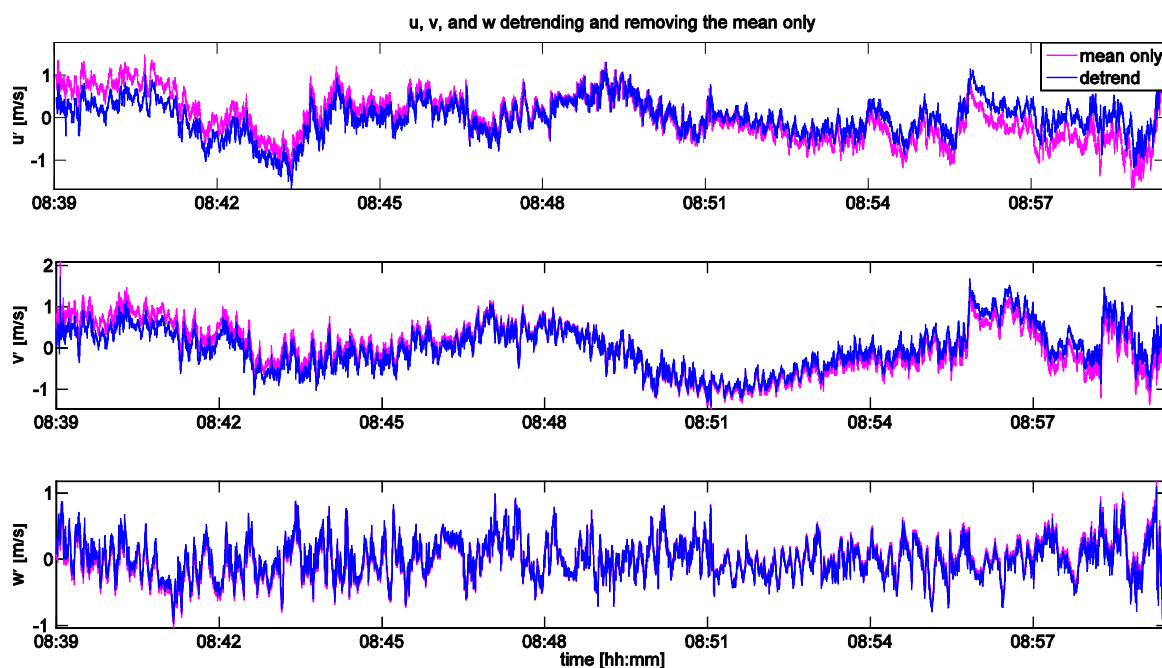


**Figure 2.5** Motion corrected sonic  $u$ ,  $v$ ,  $w$  with the trend removed (pink) and the mean only removed (blue) for 20 minutes.

### 2.2.1.2 Compute Covariance Fluxes

After all QC, motion adjustments, and rotations are done, kinematic vertical fluxes are easily computed as

$\overline{u'w'}$  is the along wind stress.

$\overline{v'w'}$  is the cross wind stress.

$\overline{w'T_s'}$  is the sonic temperature flux.

$shf = \rho_{moist} C_{p_{air}} (\overline{w'T_{sonic}'} - 0.51T_{air}\overline{w'\omega'})$  is the sensible heat flux where  $T_{sonic}$  is the high-resolution air temperature measured by the sonic,  $T_{air}$  is the slow response air temperature measured by the HMP 155 thermistor, and  $\omega$  is the mixing ratio.

$lhf = L_w \rho_{dry} \overline{w'\omega'}$ , is the latent heat flux. When mixing ratio is used in the latent heat flux covariance, no other correction is required to account for the variations of density with temperature and water vapor content (Webb et al. 1980) as long as the density of dry air is used to compute the flux.

## 2.3 METHODS: BULK FLUXES

Bulk methods are well suited for ship-based flux calculations. Compared to the high-rate three dimensional velocities needed for covariance fluxes, mean winds used in bulk fluxes are not as complicated by ship motion issue. Bulk methods indirectly estimate the fluxes by measuring the air-sea velocity, temperature and humidity differences, rather than directly measuring the ensemble of eddies. For bulk fluxes the coefficients of drag, heat flux, and moisture flux are parameterized. Verifying these parameterizations requires

high-quality independent flux measurements, such as made by the eddy covariance method.

### 2.3.1 Theory

Bulk aerodynamic formulae for calculating fluxes are based on flux gradient similarity theory, which states that the vertical flux of a scalar is proportional to its vertical gradient. The actual gradient is very difficult to measure on a moving ship (again primarily due to flow distortion). Instead, the air-sea differences in velocity, temperature and humidity are measured and these differences are related to the fluxes through transfer coefficients. The neutral value of the transfer coefficients are typical parameterized as a function of wind-speed (e.g., Large and Pond, 1981, 1982) or aerodynamic and thermal roughness lengths (e.g., Lui et al. 1979). The COARE algorithm uses the roughness length approach and using MOS to account for the impact of atmospheric stability on the transfer coefficients. For the air-sea differences, the surface of the ocean is taken as the lower height and values at the surface are assumed to extend up to the height of the roughness lengths, which are typically less than 1 mm over the ocean. At this boundary the average vertical velocity  $\bar{w}$  is assumed to be zero,  $\bar{u}$  at the surface is equal to the ocean current speed via the frictional no-slip condition, and the air at the interface is assumed to be saturated over sea water at the ocean interface temperature. The bulk aerodynamic flux equations for sensible and latent heat flux across the air-sea boundary are defined for average quantities as:

$$SHF = \rho_{air} C_{pa} C_h U (SST - T_{air}); [W/m^2]$$

$$LHF = \rho_{air} \lambda C_e U (0.98 q_{sat}(SST) - RH q_{sat}(T_{air})); [W/m^2]$$

where  $U$  is the average scalar wind speed, SST is the interfacial skin temperature,  $T_{air}$  is air temperature at 10 meters above the surface,  $q_{sat}(SST)$  is the saturation specific humidity at the sea surface temperature, RH is the relative humidity of the air at the interface, and  $q_{sat}(T_{air})$  is the saturation specific humidity at the air temperature, so that the air specific humidity is  $q_{air} = RH q_{sat}(T_{air})$ . Physical constants are  $C_{pa}$ , the heat capacity of air at constant pressure;  $\rho_{air}$  the density of air; and  $\lambda$ , the latent heat of evaporation.  $C_h$  and  $C_d$  are bulk transfer coefficients for sensible and latent heat known as the Stanton and Dalton numbers, respectively.

Surface momentum stress is a vector quantity defined as:

$$M_i = \rho_a C_d U (u_{ci} - u_i); [N/m^2]$$

Where  $u_{ci}$  is the  $i=1,2$  horizontal component of the surface current;  $u_i$  is the corresponding wind vector at the measurement height; and  $C_d$  is the transfer coefficient for stress, also known as the drag coefficient.

Such bulk flux algorithms were developed from the Liu, Katsaros, Businger (Liu and Businger, 1975; Liu et al. 1979; hereafter LKB) model, which parameterizes the surface flux of heat, moisture and momentum using the bulk transfer coefficients  $C_h$ ,  $C_e$  and  $C_d$ . The bulk transfer coefficients relate the fluxes to bulk measurements of wind speed, air temperature, SST, and moisture content (Liu et al., 1979). The LKB model is based on Monin-Obukhov Similarity (MOS) theory which states that turbulent processes can be described using the nondimensional height  $\zeta = z/L$  where  $z$  is the height of the measurement and  $L$  is known as the Obukhov length. The Obukhov length is the height at

which the generation of turbulence by buoyancy and shear are equal. Atmospheric stability affects the sign of  $L$  such that  $\zeta < 0$  indicates unstable conditions,  $\zeta = 0$  indicates neutral stability, and  $\zeta > 0$  indicates stably-stratified conditions. The stability parameter modifies the transfer coefficients  $C_h$ ,  $C_e$ , and  $C_d$  depending on atmospheric stability. The flux-gradient similarity relationships were tested and empirical relations for the stability dependence of these transfer coefficients was pursued in the Kansas wheat field experiments of the 1960s and 1970s (e.g. Businger et al., 1971, reviewed in Kaimal & Wyngaard, 1990) and thereafter extended to marine based bulk flux algorithms (Liu & Businger, 1975; Liu et al., 1979; Fairall et al. 1996, 2003). The stability functions used in the COARE algorithm (Fairall et al. 1996, 2003) were validated over the ocean by Vickers and Mahrt (1999) and Edson et al. (2013).

The bulk method shares the eddy covariance method's requirements of horizontal homogeneity, ergodicity, and stationarity. Additionally it is assumed that fluxes can be scaled by the transfer coefficients and the stability parameters.

### **2.3.2 COARE Version 3.5**

The COARE bulk aerodynamic algorithm for computing air-sea fluxes was developed based on the LKB bulk aerodynamic model during the TOGA-COARE experiment of 1992-93. The LKB model was expanded to scale the surface roughness length by the state of the ocean surface with the Charnock relation  $z_0 = \alpha u_*^2 / g$ . Charnock's constant  $\alpha$  can be parameterized as a function of the wind speed, the wave age, or the wave height. Values of Charnock's constant vary experimentally but usually fall between 0.01 and 0.035.

The COARE algorithm continues to be refined, updated and verified to suit bulk flux calculations in a wide range of conditions, including high and low wind speeds (Fairall, et al., 1996b, 2003). As of writing, COARE Version 3.5 (Edson et al., 2013) is the most recent revision, with improvements over COARE version 3.0 primarily related to the development of surface roughness parameters used to compute wind stress.

Corrections for the skin temperature due to a viscous layer cooled at the sea surface (cool skin) (Saunders, 1967), and a diurnal warm layer heated by absorption of solar radiation (warm layer) in the upper few meters to tens of meters of the ocean were developed for use with the COARE algorithm (Fairall et al. 1996a). A detailed discussion of the effect of the warm layer and cool skin corrections is presented in chapter 3.

### 2.3.3 Implementation of COARE

The computer code *coare35vn.m* is a vectorized MATLAB function that can be called independently or by the *coare35vnWarm.m* function, which will add the warm layer parameterizations ([ftp://dynamo.dms.uconn.edu/Warm\\_Layer\\_COARE\\_35/](ftp://dynamo.dms.uconn.edu/Warm_Layer_COARE_35/)). The cool skin correction is built into *coare35vn.m*, but can easily be turned off by setting the variable `jcool = 0`. Both functions include non-linear equations that require iterative solutions.

Without the warm layer, *coare35vn* has no diurnal forcing and therefore does not require any knowledge of the local time, so all fluxes can be computed in parallel. Basic inputs are wind speed relative to the current, height of wind measurement, air temperature, height of air temperature measurement, relative humidity (RH), height of

RH measurement, air pressure, sea surface temperature (SST), depth of SST measurement, downward short wave radiation, downward long wave radiation, latitude, inversion height and rain rate. Wind speed, air temperature, RH, and SST can be provided as a vector time series. Constant measurement heights are expected. Air pressure, downward short and long wave radiation, and latitude can be vectors, constants, or not-a-number (NaN), which is a flag indicating a missing value. If these variables are not provided, climatologically representative values are used.

COARE v.3.5 has three options for computing fluxes. The default is the wind-speed dependent formulation, which has proven robust at reproducing EC fluxes in a wide range of surface conditions up to wind speeds of 25 m/s (Edson et al., 2013) (This option is chosen by setting set both phase speed and significant wave height of dominant waves to not-a-number in MATLAB). The second option is a wave-age dependent formula, which requires the user to specify the phase speed of the dominant waves, but not the significant wave height. Finally, there is a sea-state dependent formulation which requires both the phase speed and the significant wave height of dominant waves. In this thesis, the wind-speed dependent formulation is used because it is best suited for ship based measurements (Edson et al., 2013). A thorough analysis of the different parameterization options and assessment of the improvements in COARE 3.5 can be found in Edson et al. (2013).

The bulk transfer coefficients  $C_p$ ,  $C_e$  and  $C_d$  are nonlinear functions of the surface roughness length and atmospheric stability and must be determined iteratively (Fairall et al., 1996b). Furthermore, heat flux and the modeled interface sea surface temperature also must be numerically integrated if the warm layer code is utilized. Ten iterations are used

to achieve convergence for all variables in the flux code. The warm layer requires the diurnally resolved solar forcing and hence must be run using hourly or higher temporal resolution. Additional inputs to the warm layer code include the year-day timestamp and longitude for computing local solar time, and SST measurement depth.

Additional instruments deployed during DYNAMO to supplement bulk flux calculations include a floating SBE-56 thermistor and a sea-snake thermistor that both measured SST at 0.05 m depth. A pyranometer and pyrgeometer that measured short and long wave radiation, respectively, were mounted on top of the PSD shipping container on the 02 deck and their data was logged by a CR1000 data logger located inside the container. Air pressure, temperature, GPS and compass data from the ship computer system, were all logged at 10 Hz by a CR3000 data logger used to log the OSU flux system. Surface ocean currents were measured by a hull-mounted Acoustic Doppler Current Profiler (ADCP), and the OSU ocean mixing group processed and provided the surface current data.

## **2.4 RESULTS**

### **2.4.1 OSU Fluxes**

The covariance fluxes are computed using data exclusively from the OSU instrumentation and a covariance flux procedure adapted from the University of Connecticut methods, courtesy of Dr. James Edson. OSU data was supplemented with PSD data for radiative fluxes, SST, and rain rate to calculate bulk fluxes using the COARE version 3.5 bulk algorithm. Figure 2.6 shows a time series of the OSU sensible and latent heat fluxes using covariance and bulk methods.

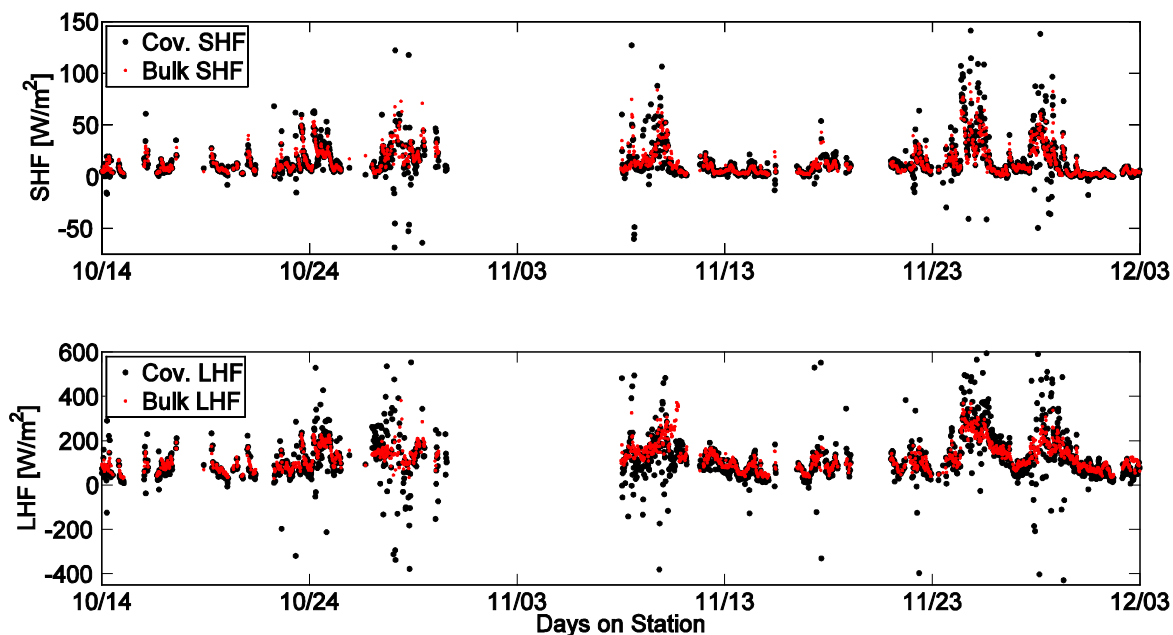


**Figure 2.6** Sensible (top) and latent (bottom) heat flux for legs 2-3 of DYNAMO. Black are covariance fluxes and red are bulk.

Bulk fluxes are less erratic than covariance fluxes by nature, and suffer less from data spikes, as seen in Figure 2.6. While very large negative fluxes can be physical, the possibility remains that these may be artifacts of the averaging window or insufficient quality control. These occasional large fluxes are suspicious and warrant reexamining the QC scheme. The OSU HMP155 humidity and temperature probe was dropped on deck at the beginning of leg 2 and un-physical spikes in the temperature reading throughout the DYNAMO IOP suggest that the sensor may have been compromised. Air temperature from the HMP is only used to calculate air density over the averaging window, and is therefore, unlikely responsible for the large fluxes seen in Figure 2.6. The HMP155 was also not actively aspirated with a fan, so suffers from solar warming on calm sunny days.

## 2.4.2 OSU Bulk vs. Covariance, & Removing the Mean or the Trend

I experimented with 10 min and 20 min windows when computing covariance and bulk fluxes. A longer averaging window can serve to decrease random errors associated with a limited sample size of large eddies. However non-stationary conditions during transitions in the flow, or changes in exposure of the ship and sensors to the flow, can introduce systematic errors in the fluxes. Figure 2.7 shows scatter plots of OSU bulk and covariance fluxes computed with 10 and 20 minute averages, and the slopes of linear fit lines. The variability in both 10 and 20 minute fluxes is primarily in covariance fluxes, and changing the averaging window increases to slope of linear regression lines from  $\sim 0.9$  to close to 1 indicating that the 20 minute averaging window is a better choice.

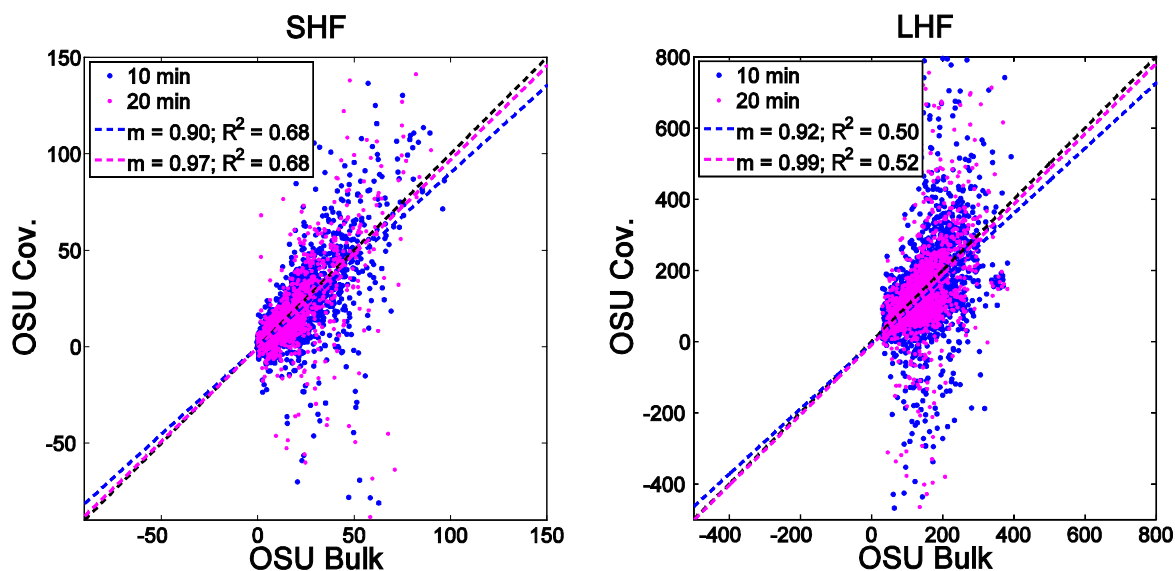


**Figure 2.7** OSU bulk fluxes vs. detrended covariance computed for window lengths  $\tau$  of 10 (blue) and 20 minutes (magenta). The black dashed line is a one-to-one reference. The slope  $m$  of the linear regression lines indicated in the legend.

Removing the trend vs removing the mean only before taking the covariance of the perturbations can affect the mean fluxes. The UConn flux algorithm detrends while PSD subtracts the mean only. In Figure 2.8, scatter plots of covariance fluxes computed

with removing the mean only, or removing the mean and the trend do not suggest any systematic error induced by either option.

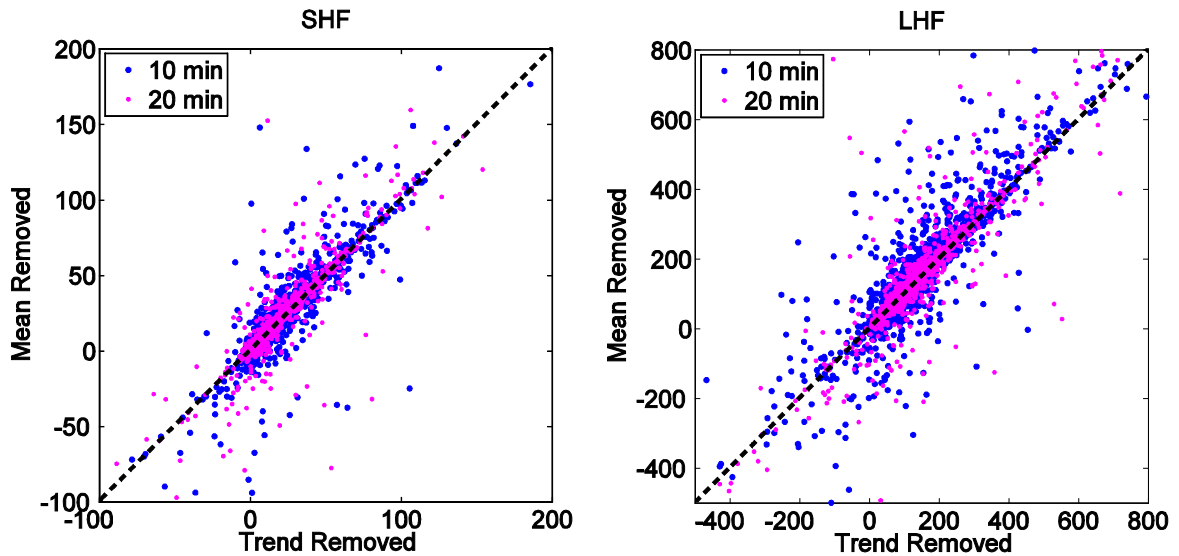


**Figure 2.8** OSU covariance fluxes with the trend removed, and the mean only removed computed with  $\tau = 10$  and 20 minutes.

The mean and standard deviation of the OSU bulk and covariance fluxes computed with 10 and 20 minute averaging windows, and detrending or removing the mean only, are listed in Table 2.1. In the mean over legs 2 and 3, OSU covariance and bulk sensible heat fluxes agree for both 10 and 20 minute averaging windows. The 10-minute window does not capture the mean latent heat flux very well regardless of the perturbation isolation method. Most likely, this is because large eddies are under sampled by the 10-minute window, resulting in flux underestimation, when compared to the bulk estimate. Considering the 20 minute fluxes, detrending gives closer agreement with the mean bulk estimate for both sensible and latent heat flux ( $0.0 \text{ W/m}^2$  and  $+0.2 \text{ W/m}^2$  bias respectively) than removing the mean only ( $+2 \text{ W/m}^2$ , and  $-5.4 \text{ W/m}^2$  bias respectively).

Furthermore, detrending decreases the standard deviation of the fluxes by approximately 10-25%, bringing the estimates closer to the bulk standard deviation values. When only the mean is removed, disagreements between covariance and bulk fluxes may be related to nonphysical large scale contamination associated with non-stationary events. From sampling variability one expects 10-minute fluxes to have higher variability than 20 minute fluxes, however, as seen in Table 2.1, the standard deviation actually increases slightly for the 20 min fluxes. Both LHF and SHF standard deviations are appreciably larger for covariance fluxes than bulk, whether computed with a 10 or 20 minute window.

**Table 2.1** OSU sensible and latent heat flux mean and standard deviation computed with  $\tau = 10$  and 20 minutes using covariance and bulk methods.

	Mean		STD	
	10 min	20 min	10 min	20 min
Sens. Cov. trend removed	10.1	10.8	16.2	17.4
Sens. Cov. mean removed	12.6	12.8	22.6	23.6
Sens. Bulk	10.7	10.8	11.3	11.4
Latent Cov. trend removed	109.6	115.6	96.3	102.0
Latent Cov. mean removed	108.5	110.4	112.7	111.6
Latent Bulk	115.5	115.8	54.7	54.9

### 2.4.3 Comparisons Between OSU, PSD, and UConn Fluxes

The OSU, PSD, and UConn eddy covariance flux systems were nearly collocated on the forward mast of the R/V *Revelle*. Presumably these systems should measure close to the same flux. There is the potential for flow distortion artifacts to cause variations from one system to another. The different positions of the three systems could be advantageous if fluxes were preferentially selected from the optimal system for each

wind direction to maximize coverage and minimize flow distortion effects. In the event of blockage of one set of sensors, fluxes can be computed from measurements of another better-exposed set of sensors. The UConn sonic was mounted on the port side, PSD in the middle and OSU starboard. Combined, these systems should adequately resolve fluxes for oncoming relative winds in an  $180^\circ$  sector or greater.

#### ***2.4.3.1 OSU, PSD and UConn Covariances***

Section 2.4.2 indicated a 20-minute averaging window and detrended times series produced the best estimate of covariance fluxes from OSU data. 20-minute detrended OSU EC fluxes are compared with the PSD (not detrended) and UConn (detrended) 20 minute EC fluxes. Figure 2.9 shows scatter plots of each comparison along with a black, dashed one-to-one reference line and a red, dashed regression line. The slope of the regression line and correlation coefficient are listed on each panel. The comparisons of OSU and UConn with PSD (Figure 2.9a, b, c and d) have more common data points that passed the quality control tests because the PSD system was centrally located between the OSU and PSD systems. The OSU and UConn comparison is limited because the wind direction filters different points from these systems located on opposite sides of the mast. Panels b and d suggest that PSD covariance latent heat flux is biased low. Though PSD appears to underestimate latent heat flux, fluxes are all correlated at 0.5 or greater with respect to OSU and UConn. The only correlation less than  $\sim 0.5$  is between OSU and UConn LHF. This is likely attributed to differences in wind, and moisture measurements due to the orientation of each respective flux system on the mast. Table 2.2 shows the mean values for all covariance fluxes compared here. It is apparent from the consensus

bulk flux estimate that OSU and UConn covariance fluxes capture the mean of latent and sensible heat fluxes, while PSD LHF is indeed low.

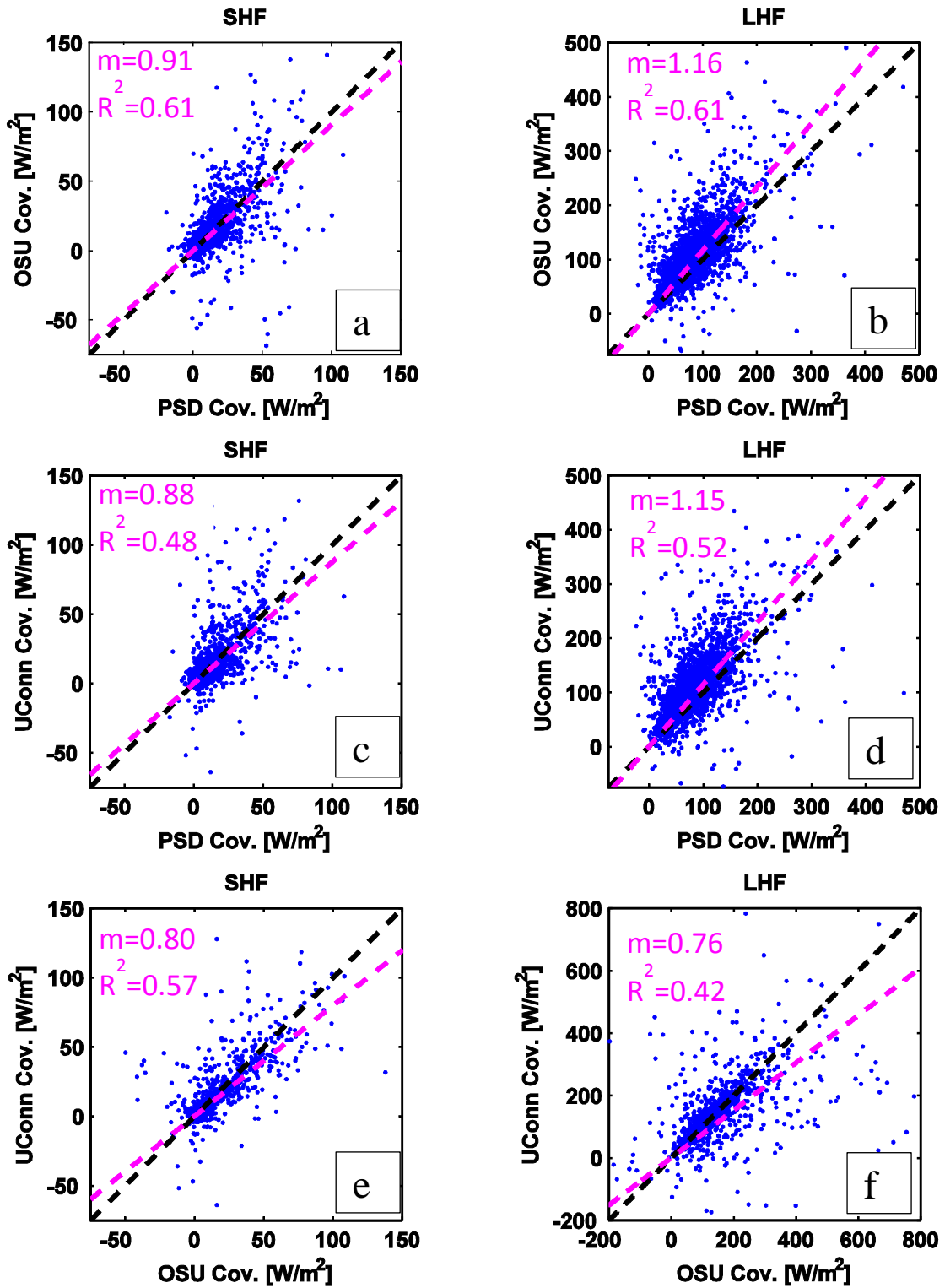


**Figure 2.9** (a,b) OSU versus PSD, (c,d) UConn versus PSD, (e,f) UConn versus OSU covariance fluxes, all computed with covariance windows of 20 min. A black, dashed

one-to-one line is shown for reference along with the linear regression (magenta dashed) of each pair compared; slopes (m) and correlation coefficients ( $R^2$ ) are listed.

Table 2.2 shows the mean, standard deviation and correlation coefficients of OSU, PSD, UConn, compared with the consensus bulk fluxes. Correlation coefficients are reported with respect to the consensus bulk fluxes. PSD fluxes are closely correlated with the consensus fluxes yielding correlation coefficients of 0.80 or greater, except the eddy covariance latent heat flux, which is 0.72. For sensible heat flux, the OSU bulk flux is extremely well correlated at 0.96, while covariance flux is correlated at 0.71. OSU latent heat flux shows the opposite trend with the covariance fluxes (0.80) slightly higher correlated to the consensus fluxes than the bulk (0.77). UConn bulk fluxes are correlated at greater than 0.9 for both sensible and latent heat fluxes, while UConn covariance fluxes are least well correlated, less than, 0.47 (LHF), 0.57 (SHF).

**Table 2.2** Mean and standard deviation of bulk Consensus, OSU and PSD and UConn covariance and bulk fluxes. Correlations are with respect to bulk Consensus fluxes.

		Mean W/m <sup>2</sup>	STD W/m <sup>2</sup>	Correlation W/Consensus
Sensible Heat	Consensus Bulk	9.9	10.8	1.00
	OSU Covariance	10.1	16.2	0.71
	OSU Bulk	10.7	11.3	0.96
	PSD Covariance	11.2	15.5	0.80
	PSD Bulk	10.0	10.7	0.98
	Uconn Covariance	10.3	23.3	0.57
	Uconn Bulk	9.6	10.4	0.95
Latent Heat	Consensus Bulk	105.5	46.7	1.00
	OSU Covariance	109.6	96.3	0.80
	OSU Bulk	115.5	54.7	0.77
	PSD Covariance	81.7	50.9	0.72
	PSD Bulk	101.0	45.4	0.98
	Uconn Covariance	104.5	103.8	0.47
	Uconn Bulk	105.6	45.9	0.95

### **2.4.3.2 OSU, PSD, and UConn Covariance vs. Consensus Bulk**

OSU, PSD and UConn eddy covariance fluxes are compared to the combined best estimate of bulk fluxes that use cross-calibrated sensors from all three systems (de Szoeki, 2014, submitted), hereafter referred to as *consensus* bulk fluxes. The consensus bulk fluxes were computed for 10-minute averaged bulk quantities in equations (p.46). OSU, PSD, UConn eddy covariance fluxes versus consensus bulk fluxes (Figure 2.10) show that OSU and UConn covariance fluxes have larger variability than PSD bulk fluxes. Though it is expected that the 20 Hz data of the OSU system will have more variability than the 10 Hz data of PSD or UConn, the covariance over the window ought to be nearly the same, so differences in PSD, OSU and UConn fluxes are likely related to sampling and data processing differences. As in the previous comparison, the PSD covariance latent heat flux is lower than the consensus bulk estimate. The OSU and UConn bulk vs covariance flux comparison are similar, with higher variability seen in covariance fluxes than bulk, and in general, PSD has less variability than OSU and UConn.

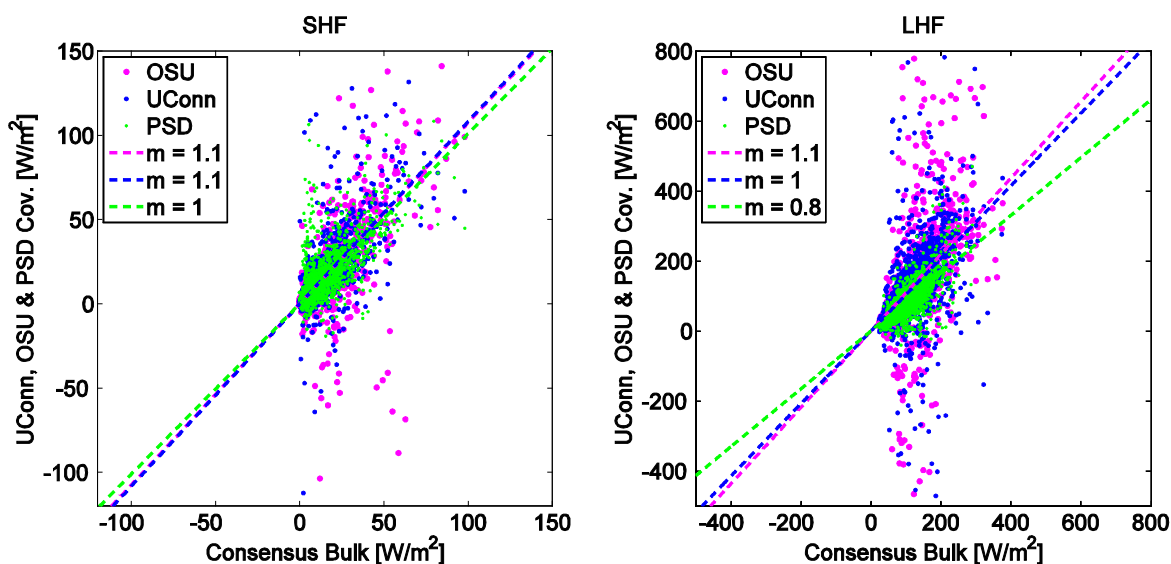


**Figure 2.10** UConn, OSU, and PSD eddy covariance heat fluxes (window length of 20 minutes) versus bulk consensus fluxes. Regression lines and slopes are shown in corresponding colors.

#### 2.4.3.3 OSU, PSD, and UConn Bulk vs. Consensus Bulk

Finally, bulk fluxes from the three systems are compared to the consensus bulk fluxes (Figure 2.11). OSU and PSD fluxes show considerably higher agreement with consensus fluxes than the comparison with covariance fluxes. OSU has suspiciously high latent heat fluxes, notably in a cluster more than twice as large as the consensus fluxes when consensus fluxes are low. This could be related to unphysical air temperature and relative humidity estimates because of poor performance related to lack of aspiration of the OSU temperature and humidity sensor.

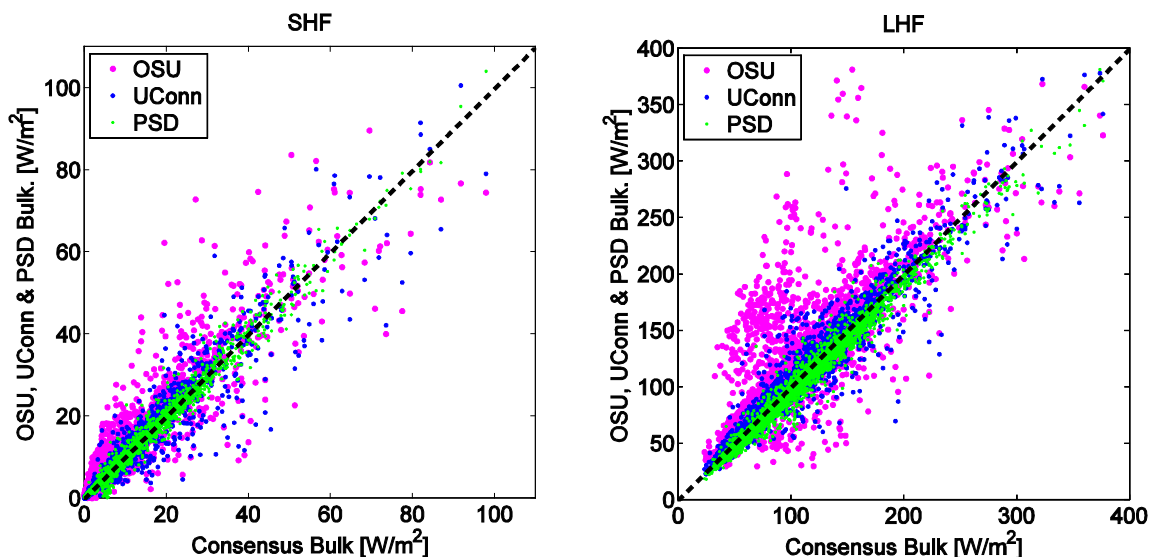


**Figure 2.11** OSU and PSD bulk fluxes computed for 10-minute averaged bulk quantities versus bulk consensus fluxes.

## 2.5 DISCUSSION

Covariance fluxes were calculated using the OSU data stream and subtleties of the covariance calculation were examined. The choice of averaging window did not seem to affect the sensible heat flux calculation substantially. Increasing the averaging window from 10 to 20 minutes brought the OSU covariance and bulk latent heat estimates closer (reducing the bias from  $\sim 10\%$  of the mean to 0% for both sensible and latent heat fluxes). The larger averaging window could capture more of the large scale eddies; whereas the 10 minute window may be missing some of the flux associated with these larger eddies.

Two methods can be employed when isolating perturbation variables for the computation of covariances. One method is to subtract the mean over the averaging interval; another method is to detrend the data by subtracting the mean and the trend.

Both methods yield perturbations from the background state, but the background is defined differently in each case. For both sensible and latent heat fluxes, detrending produces more robust fluxes that vary less, and agree better with the OSU bulk estimate, in the mean and standard deviation, as compared with removing the mean only. Since 20 minute window detrended fluxes agree consistently with the bulk consensus fluxes, I advocate computing covariance and bulk fluxes using window length  $\tau$  of 20 minutes and detrending all time series within the covariance flux calculations.

Fluxes from the OSU, PSD and UConn covariance flux measurement systems are compared. The anemometers were mounted so that the UConn system was slightly port side, PSD was in the center, and OSU was slightly starboard. Hence, flux estimates could potentially be filtered for wind direction such that the optimally oriented system with respect to flow distortion could be used preferentially, or assigned higher weight in an average. A detailed comparison of the three systems as a function of relative wind direction would be useful, but is beyond the scope of the present work.

This analysis revealed that individual realizations of either covariance or bulk fluxes computed from the OSU and UConn systems have substantially more variability than those computed from the PSD system. However, in the mean over legs 2 and 3, neither the OSU nor UConn flux estimates appear compromised. Figure 2.12 summarizes sensible and latent heat flux means and standard errors. Overlapping error bars indicate that OSU covariance, PSD bulk, and UConn covariance sensible heat flux (SHF) are in agreement with consensus bulk SHF. Only the UConn bulk and covariance latent heat flux (LHF) agree with consensus LHF, though the OSU covariance estimate comes close. OSU bulk fluxes tend to overestimate the consensus fluxes by less than 10% for both

latent and sensible heat flux computed with either bulk or covariance methods. PSD covariance sensible heat flux is high by ~12%; PSD bulk sensible heat agrees remarkably well. PSD covariance latent heat flux is  $\sim 80\text{W/m}^2$  compared to other latent heat flux estimates  $>100\text{ W/m}^2$ . The PSD bulk flux is only slightly lower (-4.3%) than the consensus bulk flux. It is possible that the considerable underestimation of the PSD latent heat flux could be due to the neglect of the Webb water vapor flux correction. The Webb correction accounts for a mean vertical velocity induced by air density fluctuations associated with temperature and water vapor fluctuations, while requiring zero mass flux of dry air across the air-sea interface (Fuehrer & Friehe, 2002).

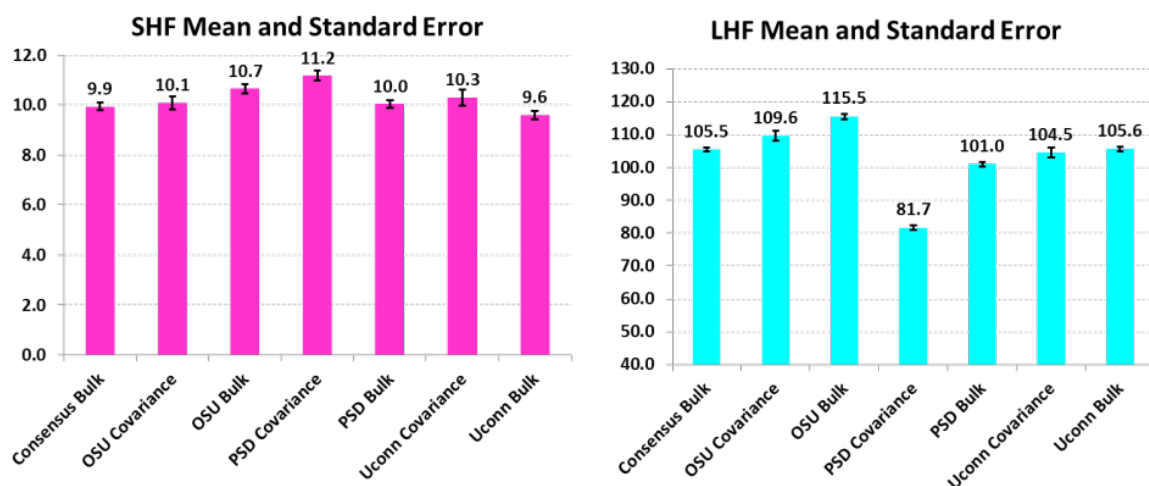


**Figure 2.12** Bulk and covariance mean and standard error for sensible and latent heat flux. Consensus bulk are considered the most reliable. For Sensible heat, OSU covariance, PSD bulk, and Uconn Covariance estimates agree with the consensus bulk fluxes. For latent heat, only the Uconn estimates are in good agreement with the consensus bulk estimate, though OSU covariance is close.

## **CHAPTER 3:        GRIDDED FLUX PRODUCT EVALUATION**

Gridded flux products provide valuable spatial and temporal coverage not available from in situ observations. Two gridded flux products are evaluated in this thesis: OAFlex and TropFlux. Both products compute fluxes with a bulk formula using data from numerical weather prediction reanalyses. These reanalyses ingest millions of observations daily with weather model predictions to produce optimal estimates of surface meteorological variables. An internationally coordinated array of 106 buoys in the tropical oceans provide in situ near-surface observations which help to constrain the reanalyses.

Gridded flux products provide coverage of global ice-free oceans for several decades. These spatially resolved estimates are verified using independent in situ observations and report a quantitative estimate of the related uncertainty, so that scientists can use these products with confidence. Six data sets are used in this analysis with the goal of assessing the confidence in gridded surface heat flux data available for use by DYNAMO investigators. These data sets are described in the following sections.

### **3.1        OBSERVATIONS INGESTED INTO THE GRIDDED PRODUCTS**

The Global Tropical Moored Buoy Array (GT MBA) is an international effort to provide freely available oceanographic and atmospheric data for tropical ocean basins. The array consists of the three sub arrays in the Pacific, Atlantic and Indian Ocean basins known by the acronyms TAO, PIRATA and RAMA (TPR), respectively. The Tropical

Atmosphere Ocean/Triangle Trans-Ocean Buoy Network (TAO/TRITON) consists of 67 buoys deployed in the Pacific Ocean. This array was established to attain better understanding of the El Niño Southern Oscillation; it became fully operational in 1994. The Prediction and Research Moored Array in the Tropical Atlantic (PIRATA) in the Atlantic Ocean followed with 10 sites installed in 1999, and was extended to 17 ongoing sites by 2006. Finally, 25 of the proposed 46 buoys in the Research Moored Array for African-Asian-Australian Monsoon Analysis and Prediction (RAMA) array have been successfully deployed in the Indian Ocean as of the time of writing. Figure 3.1 shows the locations of all active (as of the time of writing) TPR buoys in the tropical Pacific, Atlantic and Indian Oceans.

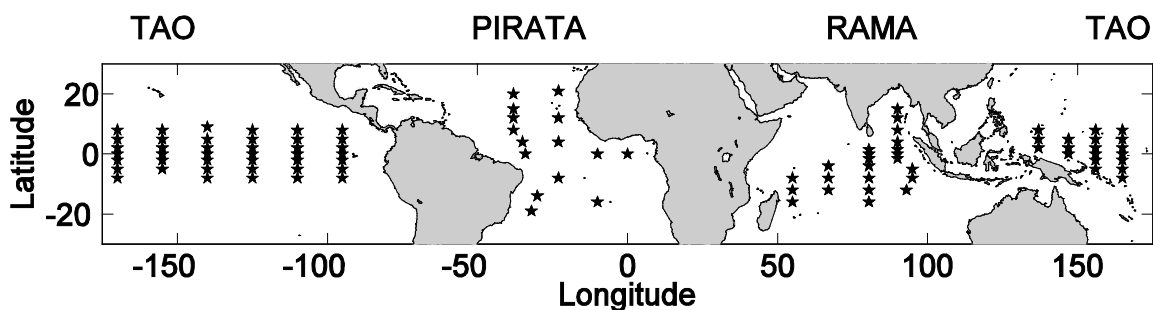


**Figure 3.1.** Stars indicate the locations of existing TAO, PIRATA and RAMA buoys in the Pacific, Atlantic and Indian Oceans respectively.

Buoys transmit daily average data via satellite, which is made freely available in real-time through the TAO Project Office of NOAA/PMEL. High frequency data, from minutes to hours, is stored aboard the buoy and available upon periodic servicing of the buoys. Data is often sparse due to vandalism damage to the buoys, and sometimes high frequency data cannot be recovered. All buoys collect surface meteorological data including air temperature, wind speed, relative humidity, etc. Most buoys are equipped

with radiometers to measure downwelling shortwave radiation. Select buoys (10 in the Pacific, 7 in the Atlantic, and 6 in the Indian Ocean) are equipped with pyrgeometers to measure longwave radiation. All of these buoys measure SST at 1 m depth, and air temperature, wind speed and relative humidity between 3-4 m height.

Buoy data include a quality control flag rating from 0-5. This thesis uses only data with quality flags 1 and 2, signifying respectively, the highest (pre and post deployment calibrations are within sensor specifications) and the default (assigned to sensors prior to recovery and calibration checks) quality. Compromised data are excluded from all analyses.

The NOAA/PMEL ftp site offers flux data in monthly, daily and sub-daily resolution (<http://www.pmel.noaa.gov/tao/oceansites/flux/main.html>). Fluxes are computed with the COARE version 3.0 algorithm. The high resolution sub-daily fluxes are computed with the warm layer and cool skin corrections described in chapter 3. Daily resolution fluxes turn both corrections off due to the inability of the daily data to resolve diurnal variability in the warm layer. However, more daily than sub-daily data are available because the 10-min and hourly data is stored on the buoy, and must be successfully recovered; while the daily average data is telemetered by satellite, and so has less chance of being lost.

### **3.2 INDEPENDENT DATASETS FROM THE DYNAMO AND TOGA-COARE FIELD CAMPAIGNS**

DYNAMO data used in this analysis is from the research vessel *Roger Revelle* and the University of Washington Applied Physics Laboratory (UW/APL) buoys. The R/V *Revelle* deployment in DYNAMO consisted of four legs interrupted by shore leave in

Thailand. In leg I between Darwin, Australia and Phuket, Thailand, the OSU, PSD and UConn flux systems were tested and the APL moorings were deployed. Hourly resolution data collected on the research vessel *Moana Wave* during the TOGA-COARE intensive observation period (1992 November 11 to 1993 February 15) is used as an additional independent data set for gridded flux product evaluation. Red dots in Figure 3.2 show the locations of the 5 independent time series used to evaluate gridded flux products. A brief description of each follows.

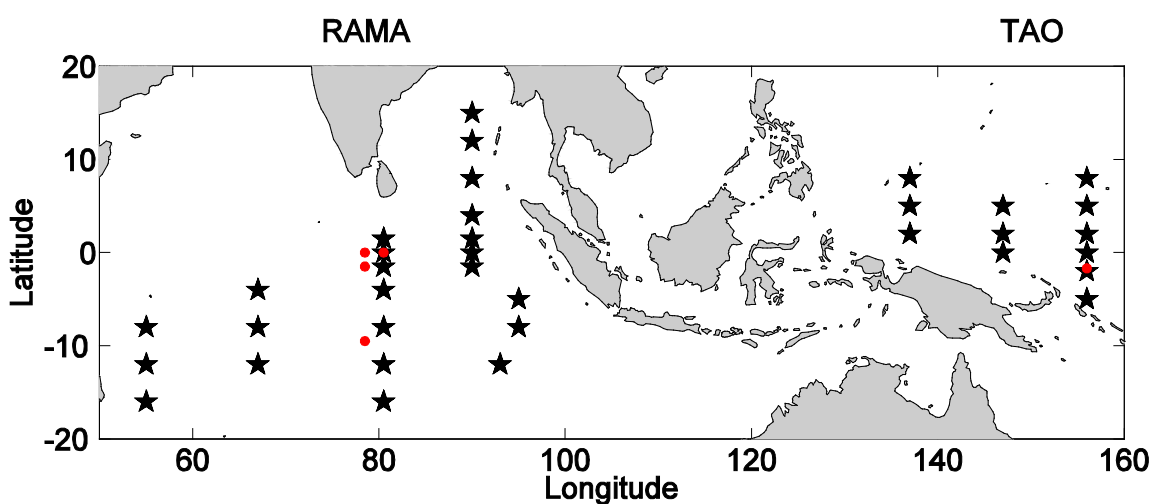


**Figure 3.2.** Black stars are the locations of RAMA and TAO buoys in the Indian and west Pacific Oceans. Red dots at latitude  $79^{\circ}$  E, longitude  $0^{\circ}$  N,  $1.5^{\circ}$  S, and  $9.5^{\circ}$  S are the APL buoys. The R/V *Revelle* and R/V *Moana Wave* are shown as red dots at  $80.5^{\circ}$  E,  $0^{\circ}$  N and  $156^{\circ}$  E,  $1.7^{\circ}$  S respectively.

### 3.2.1 *Revelle* fluxes and Meteorological Data

The R/V *Revelle* was stationed at  $80.5^{\circ}$  E on the equator for a total of 52 days during the intensive observation period (IOP). The IOP was conducted during Legs II and III with each leg lasting  $\sim 30$  days. During the IOP, the scientific party aboard the R/V *Revelle* made in situ and remote sensing measurements while the R/V *Revelle* was in

international waters. At the beginning and end of periods on station, the R/V *Revelle* conducted east-west transects along the equator and north-south transects to  $\pm 2^\circ$  along the  $80.5^\circ$  E meridian. High resolution ocean turbulence profiling was terminated at the end of leg III. However, surface flux measurements were continued on leg IV through 2012 Jan 1. Figure 3.3 shows the location of the R/V *Revelle* for the duration of the DYNAMO experiment. For all flux comparisons with the buoy and gridded products, the 10 minute R/V *Revelle* consensus data (described in section 2.4.3.2) is used to compute bulk fluxes with the COARE version 3.5 bulk algorithm.

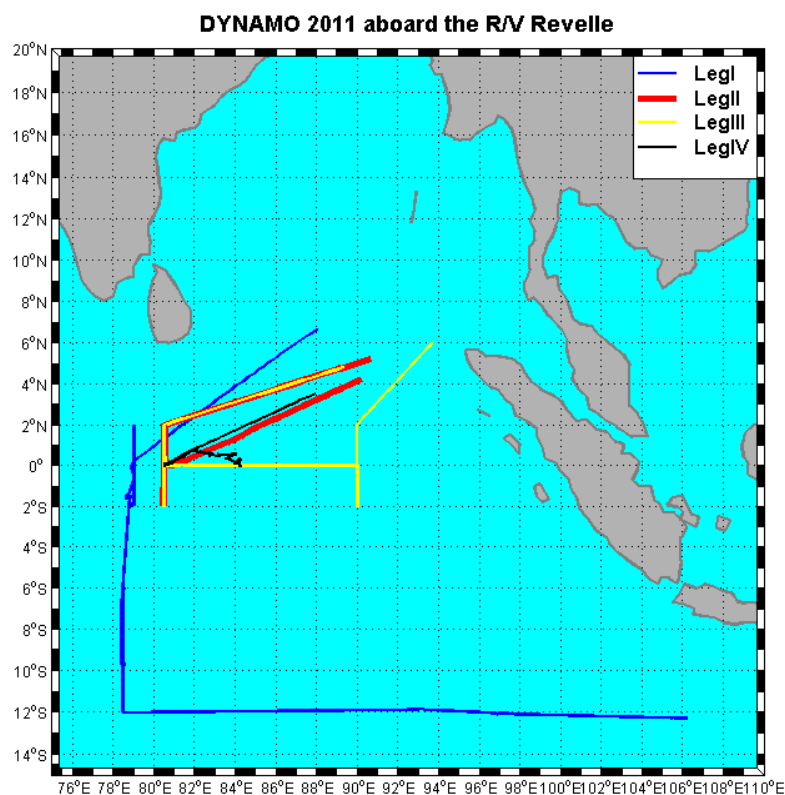


**Figure 3.3** Legs I-IV of the DYNAMO campaign. Leg I departed from Darwin Australia, while all other legs docked in Thailand. Transect paths during legs II & III are seen. All gridded flux data compared to the *Revelle* was interpolated to the nearest grid point to the daily average location of the ship. This map shows a  $2^\circ$  grid. OAFflux and TropFLux use

1° grid centered on the 0.5°. [Figure credit: Ludovic Bariteau, NOAA Physical Science Division]

### **3.2.2 APL Buoys**

The APL buoys (R-C Lien, University of Washington, Applied Physics Laboratory) provided pressure, air temperature, wind speed, humidity, rain, shortwave and long wave radiation and 1 m ocean temperature observations for this analysis. The APL buoys were deployed at a latitude of 78.5° E and longitudes of 0° N, 1.5° S, and 9.5° S in September 2011, and recovered in January 2012. The 0° N buoy has a limited data record because it was vandalized in mid-November. Data from these moorings was withheld from reanalysis and provides an opportunity to independently evaluate gridded flux products at locations relatively far (>100 km) from locations where RAMA buoy data is ingested into the reanalysis.

### **3.2.3 *Moana Wave* data from TOGA-COARE**

The R/V *Moana Wave* was stationed approximately 188 km south of the 156 W, 0° N TAO buoy for 69 days during the TOGA-COARE experiment. A description of the TOGA-COARE experimental goals and intensive flux array is provided by Webster and Lukas (1992) and Lin and Johnson (1996). The COARE bulk aerodynamic flux algorithm was developed and verified for the TOGA-COARE observations from the R/V *Moana Wave* (Fairall et al. 1996a, Fairall et al. 1996b).

### **3.3 GRIDDED PRODUCTS ON A 1° X 1° SPATIAL GRID**

This section describes the two gridded flux products, OAFlux and TropFlux, assessed in this analysis. Both use global atmospheric reanalyses and in situ observations to produce estimates of surface heat and momentum flux. The section provides a description of how the two flux products use the observational and reanalysis data.

#### **3.3.1 OAFlux**

OAFlux (Yu & Weller, 2007) is a global flux product produced by Woods Hole Oceanographic Institute (WHOI) using optimal blending of satellite retrievals, three atmospheric reanalyses, and in situ buoy observations to produce bias free estimates of surface meteorological variables (Jin & Weller, 2008b). Monthly fluxes are available from 1958-present; daily fluxes are available from 1985-present. The optimal analysis technique used by OAFlux is one of several data assimilation algorithms used for making the best state estimate of the atmosphere using various data sources (Daley, 1997). A brief description of the data sets assimilated into the OAFlux algorithm follows.

OAFlux assimilates NCEP-1, NCEP-2, and ERA-40 reanalysis data. Reanalyses also assimilate data from observations and operational weather model forecasts (based on past observations) used to produce a best estimate of global gridded data at common synoptic times. The models are initialized with a combination of previous forecasts and observations at regular intervals to optimally approximate the true state of the atmosphere, and then run forward in time. This creates a complete gridded estimate of the state of the atmosphere that fills in spatial and temporal gaps between the observations. The weight of satellite and reanalysis estimates for state variables is inversely

proportional to the error covariance; i.e. if the errors are large, the weight of the observation is small and vice versa. Observations are down-weighted in the data assimilation procedure so that the model is not skewed too heavily toward well sampled regions. A unique feature of reanalysis is that the estimated state must not only approximate observations, but the algorithm is also constrained by computer approximations of the laws of physics. Therefore unobserved or spatially coarse variables may be inferred through physical coherence of better resolved variables and model constraints (Dee et al., 2011).

The NCEP/NCAR reanalysis (NCEP-1) is a 40 year reanalysis developed jointly by the National Center for Environmental Prediction (NCEP) and the National Center for Atmospheric Research (NCAR). NCEP-1 provides 4 times daily estimates of surface variables from 1957-present (Kalnay et al., 1996). The NCEP-1 reanalysis was run continuously for 1957-present without updates of the model coding or assimilation procedure in order to not introduce artificial variability owing to changes in model developments or assimilation algorithms that appear as climate changes. The DOE/NCEP (NCEP-2) reanalysis is a reanalysis developed by NCEP and the Department of Energy (DOE), which is more automated and more consistent, and incorporates solutions to documented errors in NCEP-1 (Kanamitsu et al., 2002).

The European Center for Medium-range Weather Forecasting (ECMWF) released a second generation reanalysis product, ERA-40 (the first generation version was ERA-15), in 2003 that spans 1957-present. Observations are assimilated at 6-hour intervals, and an optimal interpolation procedure is employed to produce complete spatial coverage of limited input variables on a  $1.25^\circ$  latitude-longitude grid. The average number of

observations assimilated into ERA-40 increased from less than 20,000/day for the earlier reanalyzed periods to more than  $10^6$  observations in the later years that include extensive satellite data.

OAFlux also uses estimates of 10 m neutral winds that come from three satellite products: Special Sensor Microwave Imager (SSM/I), AMSR-E, and QuikSCAT. Surface humidity is estimated from an EOF analysis (Chou et al. 1995) of SSM/I precipitable water. Satellite SST comes solely from the Advanced Very High Resolution Radiometer (AVHRR) infrared (IR) dataset, to ensure consistency throughout the OAFlux data set. Estimates of near surface air temperature are based solely on reanalysis from ERA40, NCEP1, and NCEP2 (Jin & Weller, 2008b).

OAFlux uses high-accuracy WHOI and TPR buoy data in the weighting parameters of the input variables, and in the error analysis for reanalyzed variables. Consequently, the WHOI and TPR buoy data are not considered independent of OAFlux. Since the input variables are designed to be unbiased with respect to these buoys, the resulting fluxes will, by design, have low bias as well.

### **3.3.2 TropFlux**

TropFlux (Kumar et al. 2012) is a joint effort between the National Institute of Oceanography (NIO-CSIR, India) and the Institut Pierre Simon Laplace (IPSL, Paris, France). This product aims to produce the best estimate of fluxes in the tropical oceans between  $\pm 30^\circ$  latitude with daily resolution from 1979-present.

Data from decades of ship observations from the International Comprehensive Ocean-Atmosphere Data Set (COADS) and independent data from five Woods Hole

Oceanographic Institute buoys at climatologically distinct locations was used to analyze several available flux products (Kumar, Vialard, Lengaigne, Murty, & McPhaden, 2012b). TropFlux uses reanalysis fields from the ECMWF Reanalysis-Interim (ERA-I), released in 2006. ERA-I offers better representation of the hydrologic cycle, improved quality of stratospheric circulation, and consistency in time of reanalyzed geophysical fields compared to ERA-40. Reanalyzed fields are available on a  $0.75^\circ$  grid, with surface variables available at 3-6 hour resolution. More than  $10^7$  observations are assimilated into ERA-I daily to constrain the model (Dee et al., 2011, p. -).

Kumar et al. (2012) determined that ERA-I performed better than NCEP1 and NCEP2 in terms of phasing with observations, despite systematic biases. Therefore, bias and amplitude corrections were applied to ERA-I wind speed, air temperature, sea surface temperature, specific humidity, and long wave radiation to produce TropFlux. This procedure yields fluxes which are temporally well correlated with the independent observations. Fluxes have low bias and comparable standard deviation with respect to independent in situ observations.

Short wave radiation (SWR) is calculated with the NASA Goddard Institute for Space Studies radiative transfer model 2001 and data from the International Satellite Cloud Climatology Project (ISCCP) for the period 1983-2009 when data is available (Zhang et al., 2004). Beyond the time period of available ISCCP data, SWR is computed using the seasonal cycle and an empirical parameterization based on outgoing longwave radiation.

Cronin et al. (2006) determined that daily vector averaged wind speed from TPR buoys is often biased low in comparison with the average of hourly wind speed from

these same buoys. A gustiness correction was developed to include the effects of enhanced mesoscale convective activity observed in regions of high SST. Kumar et al. (2012) added 1-2.1 m/s to the wind speed, prior to processing in COARE, based on the ten-year bias corrected ERA-I SST (wind speed data provided on the TropFlux data portal [[http://www.incois.gov.in/tropflux\\_datasets/](http://www.incois.gov.in/tropflux_datasets/)] does not include this gustiness correction).

Since the TPR buoy data is ingested into ERA-I, and it is used to develop the bias and amplitude corrections, data from the TPR array is not independent of TropFlux, and statistical agreement between these data sets is expected by design.

### **3.4 OAFUX AND TROPFLUX DIFFERENCES**

Differences between OAFux and TropFlux give us a very rough estimate of the confidence of the flux products. Note, however, that any systematic errors common to both flux products are not detectable in the differences. OAFux and TropFlux use different data as described in section 3.3, and different processing of surface meteorological variables required by COARE, both of which lead to differences between the two products. Daily differences between OAFux and TropFlux sensible and latent heat flux estimates are at times the same order of magnitude as the fluxes themselves. Figure 3.4 shows the difference of OAFux – TropFlux on 2011 November 27, which has representative differences among these data sets, though their locations change.

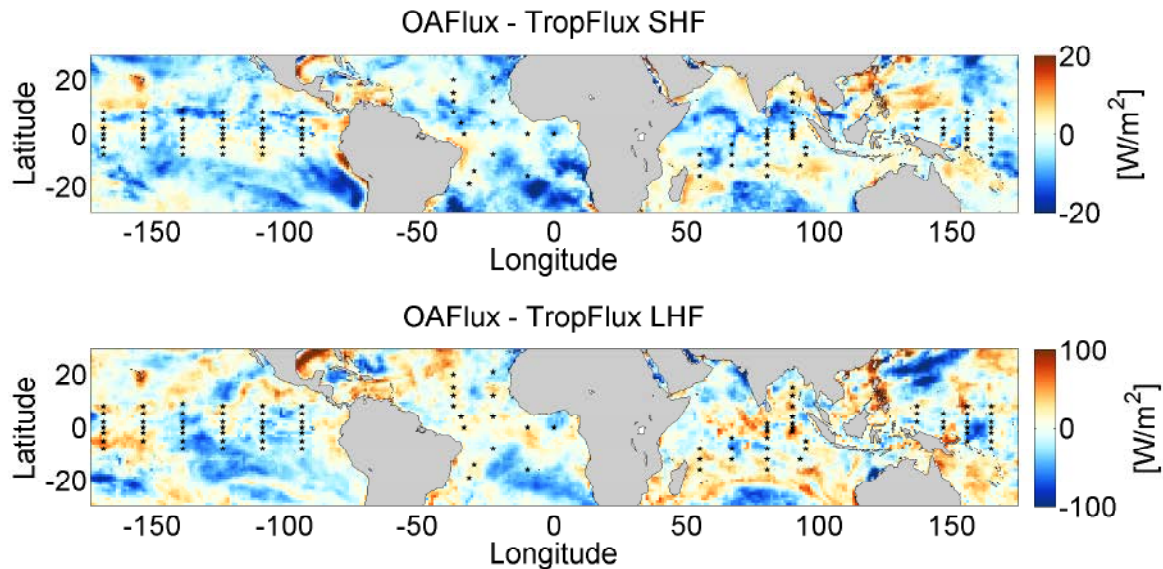


**Figure 3.4.** The difference between OAFlux and TropFlux for 27 November 2011. Black dots are the locations of all currently active TPR buoys.

The magnitudes of the differences are reduced in the annual average as seen in Figures 3.5a (SHF) and 3.6a (LHF) which show the difference in OAFlux and TropFlux averaged over 2011, and the locations of 106 TPR buoys that were transmitting data that year. Large differences still exist, especially near coastal regions. As expected, agreement is improved near TPR buoys where the buoy observations help constrain the models that provide input data to both OAFlux and TropFlux.

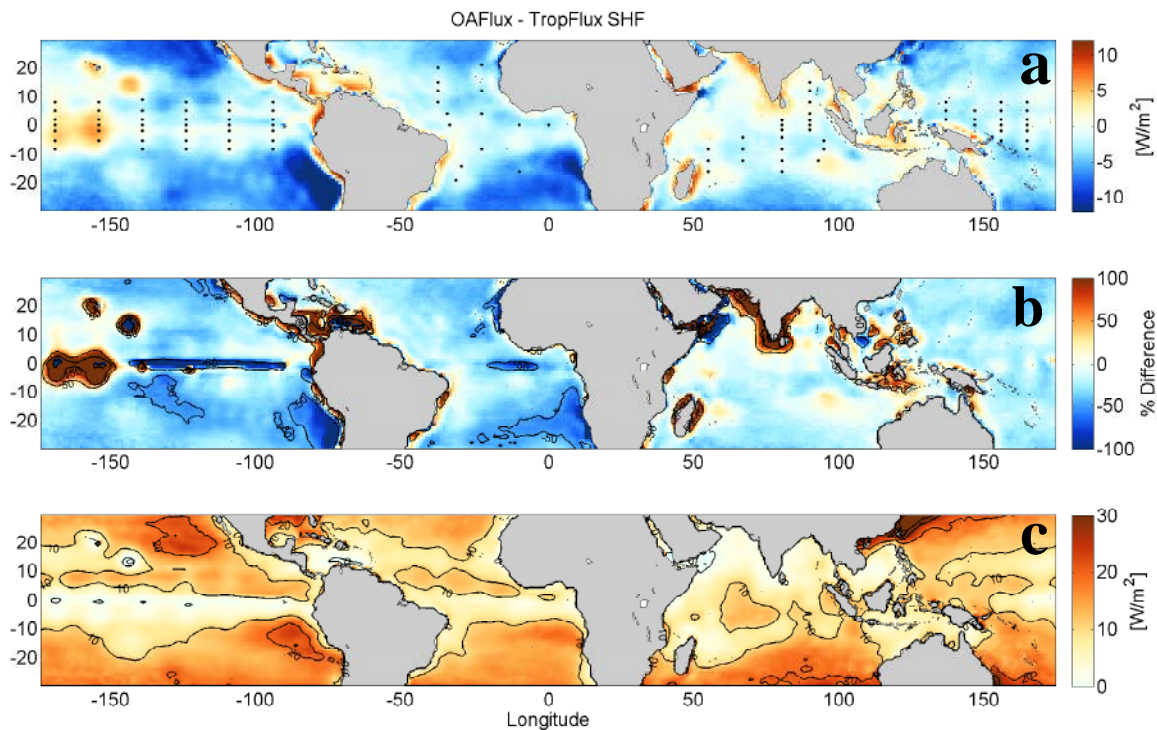


**Figure 3.5.** (a) The annual average of the difference of OAFlex – TropFlux SHF for the year 2011. (b) the % difference between OAFlex and TropFlux SHF relative to the TropFlux mean SHF, contours are -50, 50, and 150  $\text{W/m}^2$ . (c) the TropFlux mean SHF contours are 0 to 40  $\text{W/m}^2$  in steps of 10  $\text{W/m}^2$ . Black dots are 106 TPR buoys that are ingested into reanalyses used by both products and are also used in both flux algorithms.

Figures 3.5b and 3.5c show the difference between OAFlex and TropFlux SHF plotted as the percent of the mean TropFlux SHF estimate, and the mean TropFlux SHF during the year 2011 respectively. Since the mean SHF is small in many places, the percent difference exceeds 100% of the mean in these regions. Off the west coasts of South America and Africa, large differences remain (with OAFlex higher than TropFlux) despite relatively large mean fluxes ( $\sim 10 - 20 \text{ W/m}^2$ ). Differences in the % of the mean of latent heat flux estimates (Figure 3.6b) are not confounded by the near zero flux

problem of sensible heat flux, and it is clear that OAFlux and Trop Flux often disagree by  $> 20\%$  of the mean LHF.

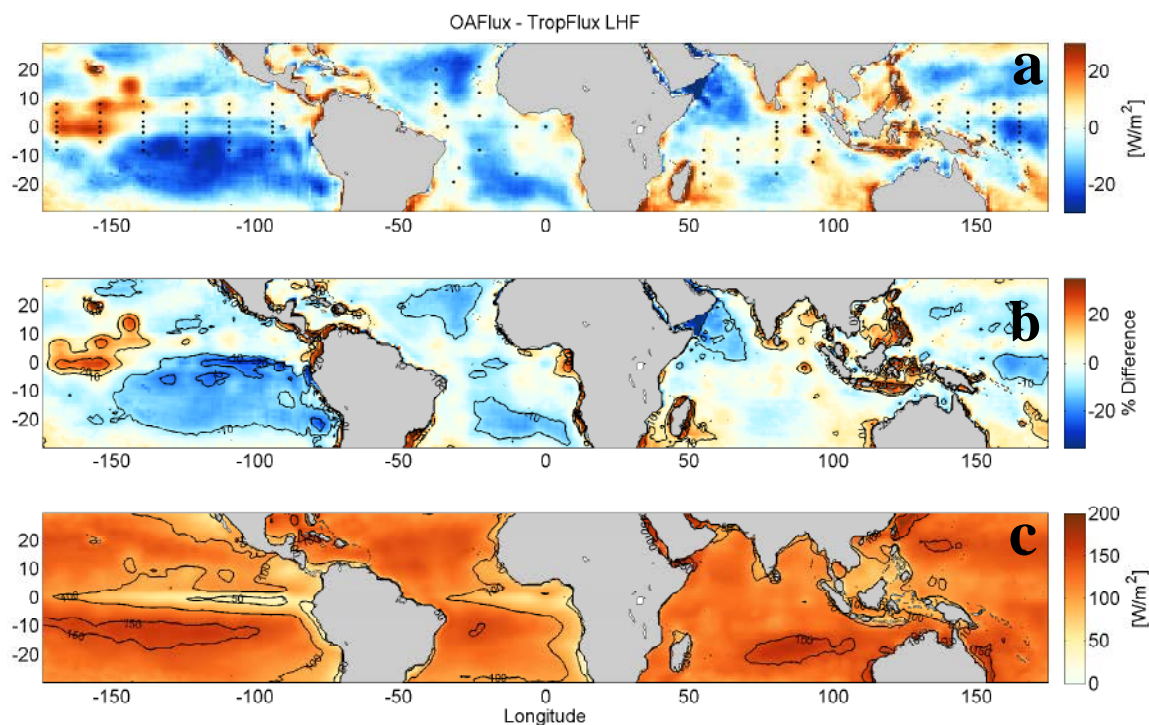


**Figure 3.6.** As in Figure 3.5 but for latent heat flux

To see the effect of assimilating sparse observations over the tropical Oceans, the following analysis compares TropFlux and OAFlux differences both near and far from TPR buoys. Figure 3.7 shows normalized histograms of the root mean square difference (RMSD) between OAFlux and TropFlux sensible and latent heat flux at buoy locations and all locations, (the contribution of buoy locations to the statistics is assumed small when all grid points are considered). The RMSDs are computed for the spatial variability for each day of 2011. Each realization in the histogram is the spatial RMSD computed for one day; there are 365 realizations in the histogram. The RMSD represents the spatial pattern of differences between OAFlux and TropFlux at buoy locations (top) and all

locations (bottom) for one day. The RMSD is intrinsically normalized by the square root of the number of points, by dividing by the number of realization before taking the square root. The number of buoy locations ( $n_b$ ) is 106, and the global number of grid cells ( $n_g$ ) is 16351. The equation for the RMSD is shown below where  $i$  represents either buoy locations ( $b$ ) or all common grid ( $g$ ) cells between OAFlex and TropFlux.

$$RMSD = \sqrt{\frac{\sum(OAFlux_i - TropFlux_i)^2}{n_i}}$$

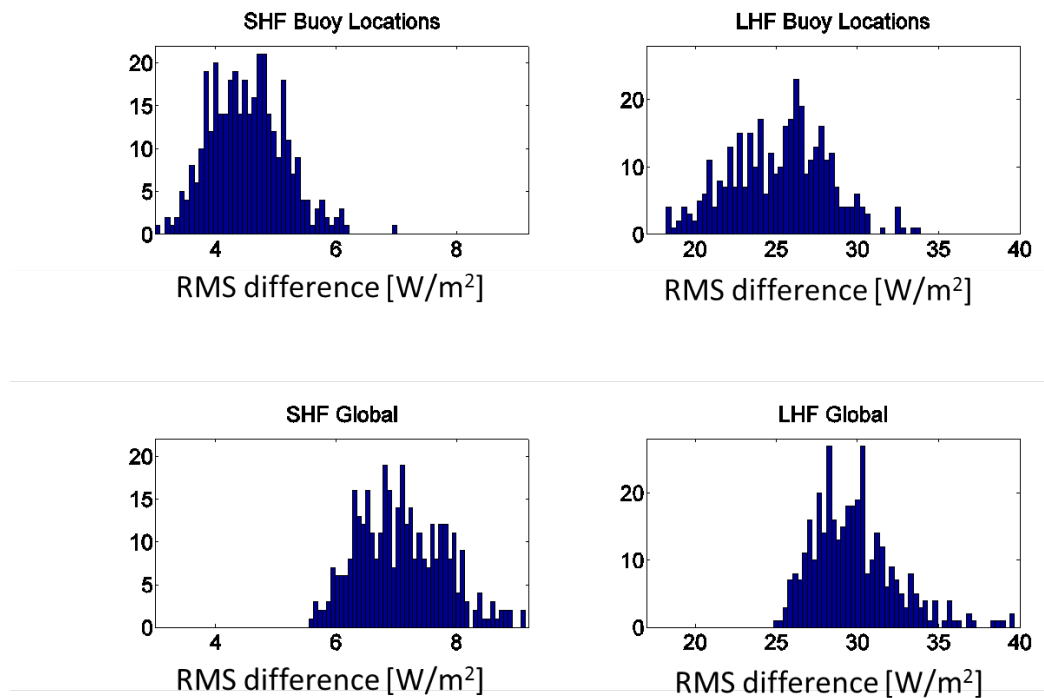


**Figure 3.7.** OAFlex and TropFlux SHF (left) and LHF (right) root mean square difference (RMSD) at  $n_b=106$  buoy locations for 365 days (top) and non-buoy locations (bottom). Each plot shows the histogram of RMSD for 365 days of data. Each realization is an RMSD over the spatial pattern of buoy locations, or all locations ( $n_g=16351$ ) for one day. Each plot contains 50 bins and the sum of realizations in all 50 bins equals 365.

Gridded fluxes agree better at buoy locations indicated by a  $\sim 4-6 W/m^2$  lower rms difference versus non-buoy locations. The maps of the daily and annual differences, and the histograms of the increased rms difference at non-buoy locations make it difficult to

determine confidence in either estimate. Large differences between the flux estimates of OAFlux and TropFlux motivate comparisons of these data sets with the in situ observations from TOGA-COARE and DYNAMO.

### **3.5 NEAR SURFACE OCEAN TEMPERATURE**

The interfacial ocean temperature is required as the lower boundary to the atmosphere in bulk aerodynamic flux calculations. This temperature is difficult to measure because there can sometimes be large gradients in the upper few meters of the ocean. These temperature differences can be modeled in the COARE algorithm, as described in section 3.3.1 and 3.3.2. First we briefly introduce and describe the effect of these near-surface gradients, especially on the surface fluxes.

#### **3.5.1 Cool skin**

Long wave radiation, sensible heat flux and evaporation cool the surface of the ocean at all times of day (but for rare cases such as beneath coastal fog). This results in a thin (~1 mm) skin of cool water, which rests atop warmer water (Figure 3.8a). Though this configuration appears buoyantly unstable, viscous forces are stronger than buoyancy. On these scales, the heat is transferred chiefly by molecular diffusion. This cooling effect of the sea surface interface in the tropics is usually slightly less than 0.3 K (Saunders, 1967). The surface cooling (mostly evaporation and long wave radiation) is slightly compensated by solar absorption during the day, so the cool layer is slightly weaker (0.2 K), and it may be up to 0.4 K at night (Fairall et al., 1996a).

The cool skin correction can be derived from the surface energy balance given by

$$\frac{\partial T}{\partial t} = \kappa_H \frac{\partial^2 T}{\partial z^2}$$

where  $\kappa_H = 0.6$  is the thermal conductivity of seawater. Assuming steady state and integrating once gives:

$$0 = \kappa_H \frac{\partial T}{\partial z} + C$$

The constant of integration  $C$  matches the net heat flux at the surface  $C = Q_{net}$ .

Integrating again from 0 to  $h$  gives:

$$\Delta T_{cool} = \frac{h(LWR + SHF + LHF - SWR_a(h))}{\kappa_H}$$

where  $\Delta T_{cool}$  is the cool skin temperature depression;  $Q_{net}$  has been expanded as the sum of radiative and turbulent surface fluxes: LWR is long-wave radiation, SHF and LHF are sensible and latent heat flux respectively,  $SWR_a$  is the absorbed short wave radiation over the cool skin thickness,  $h$ , determined as:

$$h \sim \nu / u_*$$

where  $\nu$  is the kinematic viscosity of water and changes only slightly with temperature through a density dependence.  $\nu$  is a physical, fluid specific, attribute of a fluids ability to resistance motion.  $u_*$  is the friction velocity in the water which is a measure of the surface momentum stress. Within this layer of depth  $h$ , the frictional component of the wind stress is communicated viscously (Saunders, 1967).  $\Delta T_{cool}$  is determined iteratively because shortwave radiation is a non-linear function of  $h$ . The first guess for  $\Delta T_{cool} = 0.3$ , and  $h$  is 1 mm.  $\Delta T_{cool}$  varies little throughout the day, so it is of little consequence to bulk flux calculations to use a daily average value for the cool skin (usually 0.2-0.3 K).

The inverse relationship of  $h$  to wind, combined with the direct relationship of surface flux cooling to wind, help to reduce the variability of the cool skin correction under different wind stress conditions. On calm days,  $u_*$  is small and the cool skin depth is relatively large, but weak fluxes modulate the magnitude of cooling at the surface. Conversely during high wind events,  $u_*$  is large and the cool skin depth is shallow, but large surface fluxes enhance the cooling at the surface.

### 3.5.2 Warm Layer

Short wave radiation absorbed in the upper few meters of the ocean warms the surface layer, and in the absence of sufficient wind shear, a stably stratified warm layer develops. Mechanical mixing required to distribute this heat to deeper depths comes mostly from wind shear at the surface. The correction is based on a simplified version of the ocean warming model described by Price et al. (1986), which accumulates solar heating and surface wind stress over time to determine the development of a warm layer. Peak afternoon warming between the surface and a 1 m bulk temperature measurement can exceed 3 K, and measurable warming can be detected well past sundown. A critical bulk Richardson number of  $R_{ic} = 0.65$  is used to determine  $D_T$ , the depth of the warm layer.

$$D_T \propto (2R_{ic})^{1/2} \frac{\int Shear}{(\int Heat)^{1/2}}$$

Heat input limits the warm layer depth through stratification that resists mixing; conversely, shear increases the depth through enhanced mechanical mixing. The warm layer depth is directly proportional to the integral of shear, but inversely proportional to

the square root of the integral of heat. The warm layer depth is therefore more responsive to changes in shear than heat. The warm layer correction accumulates integrals of heat and stress across the warm layer depth at each time step. Predawn warming is assumed to be 0 K and a warm layer does not begin to develop until absorbed solar radiation exceeds heat loss through evaporation, long wave radiation, and sensible heat.

A schematic of sea surface temperature with depth is shown in Figure 3.8. The viscous sub-layer (visible as a slight temperature depression at the surface in both panels) is a region in which the viscosity of the fluid dominates the dynamical processes. This layer is on the order of 1 mm deep. Within this surface skin, evaporative, sensible and radiative cooling processes depress the surface temperature by ~0.18 K-0.35 K (Fairall et al. 1996a). The cool skin phenomenon that affects SST is relatively constant over the course of a day under all convective conditions. Therefore, it is easily included in bulk formulae calculations with little error for short or long time averages.

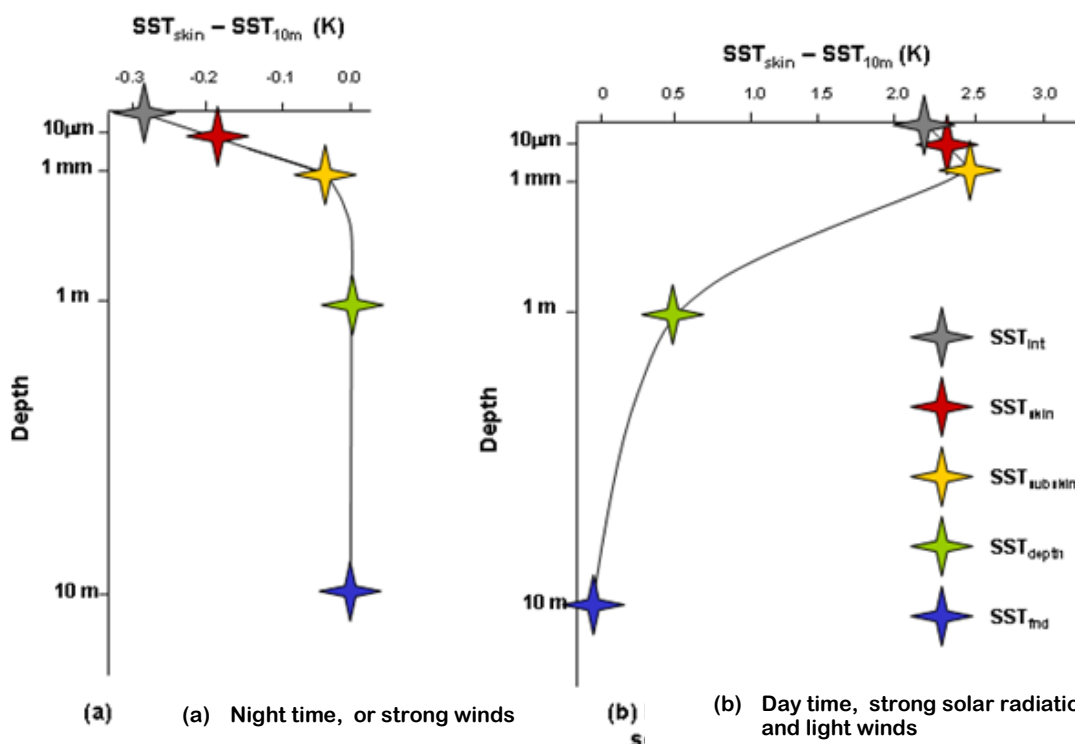


**Figure 3.8.** Sea surface temperature profile with depth. Cool skin and warm layer shown. [Figure credit: Craig Donlon, European Space Agency/ESTEC]

Conditions of a well-mixed surface layer are shown on the left, and a well-developed warm layer on the right. Figure 3.8a shows the case of persistent strong winds and nighttime conditions, where heat is continuously mixed down, and the upper layer of the ocean is of uniform temperature with depth (i.e., well-mixed) below the viscous sub-layer. This is always the scenario at night after the solar-warmed layer has been mixed out, during periods of high winds, or in the presence of deep convection that weakens the solar radiation. Light winds and strong solar warming lead to a shallow mixed layer with a large temperature gradient as seen in Figure 3.8b. Thermal stratification creates a stably stratified layer, and wind shear is required to mix heat to deeper depths. The depth of the diurnal warm layer is governed by the magnitude of surface winds and stability of the layer. Unlike the cool skin, the diurnal warm layer changes throughout the day. Warming

can occur quickly and can persist well after sundown (Fairall et al., 1996a). Commonly, warming is on the order of 2-3 K, though local surface temperatures can occasionally reach 7-8 K above pre-dawn surface temperatures (Clayson & Bogdanoff, 2013).

When daily and ( $1^\circ \times 1^\circ$ ) spatial averages are considered, the magnitude of warming is significantly diminished. Often, the warming between the surface and 1 m is zero, but it commonly exceeds 0.3 K, a typical cool skin correction for DYNAMO. Daily average warm layer corrections as high as 1.2 K are occasionally seen in the Indian Ocean during the DYNAMO field campaign. Clayson and Bogdanoff (2013) showed that using a nighttime bulk temperature for computing daily average fluxes (which is frequently done) can lead to localized errors in net heat fluxes as high as  $+12 \text{ W/m}^2$ , and that instantaneous errors in flux estimates due to ignoring the warm layer can exceed 100% during peak afternoon warming events.

It is hypothesized that ignoring the warm layer and cool skin corrections when calculating fluxes with a 1 m ocean temperature artificially increases the range of the flux estimates. Fluxes scale with the wind and the sea-air temperature and humidity differences at the interface. When winds are high, and thus fluxes are high, the surface layer of the ocean is well mixed. Under these conditions the 1 m temperature used for routine bulk flux calculations is warmer than the surface by  $\sim 0.3 \text{ K}$  as seen in Figure 3.8a, resulting in flux overestimation. Conversely, when winds are weak and insolation is strong, fluxes are low and the 1 m temperature is colder than the interface temperature (Figure 3.8b). In this case, use of the 1 m temperature in the sea-air temperature difference is expected to underestimate the heat fluxes. Using the 1 m temperature without adjusting for the warm layer and cool skin effects underestimates fluxes when

fluxes are low in calm winds and overestimates fluxes when fluxes are high in strong winds.

Solar radiation forces the warm layer through the absorption of sunlight in the upper 1 to 10s of meters. The intensity of sunlight depends on the latitude, time of year and local convective conditions. The cool skin correction, on the other hand, is primarily due to the cooling of the ocean by the air-sea temperature and humidity difference which varies little with solar forcing. Since these processes have opposite effects it is common practice not to implement one without the other.

Times series of observed ocean temperature at 0.05 m and 4 m depth during the DYNAMO 2011 field campaign (Figure 3.9) show several consecutive calm days with very light winds were observed during the suppressed phase of the MJO (~Oct 7-16, and Nov 12-19) where the sea state was nearly flat. During these periods, a daily average warm layer of up to  $0.5^{\circ}\text{C}$  was observed between the 0.05 m and 4 m depths. Hourly resolution temperatures show as much as  $2^{\circ}\text{C}$  peak difference on days with diurnal warming. These observations reinforce our observations that the warm layer strongly affects daily averages, and has seasonal and intraseasonal modulation when the daily average diurnal warming overwhelms the cool skin effect. In the Indian Ocean, this effect is modulated on intraseasonal time scale that is linked to the MJO. During the convectively active phases of the MJO (~Oct 22-29, and Nov 22-Dec 1), SST was cools, and the warm layer is non-existent.

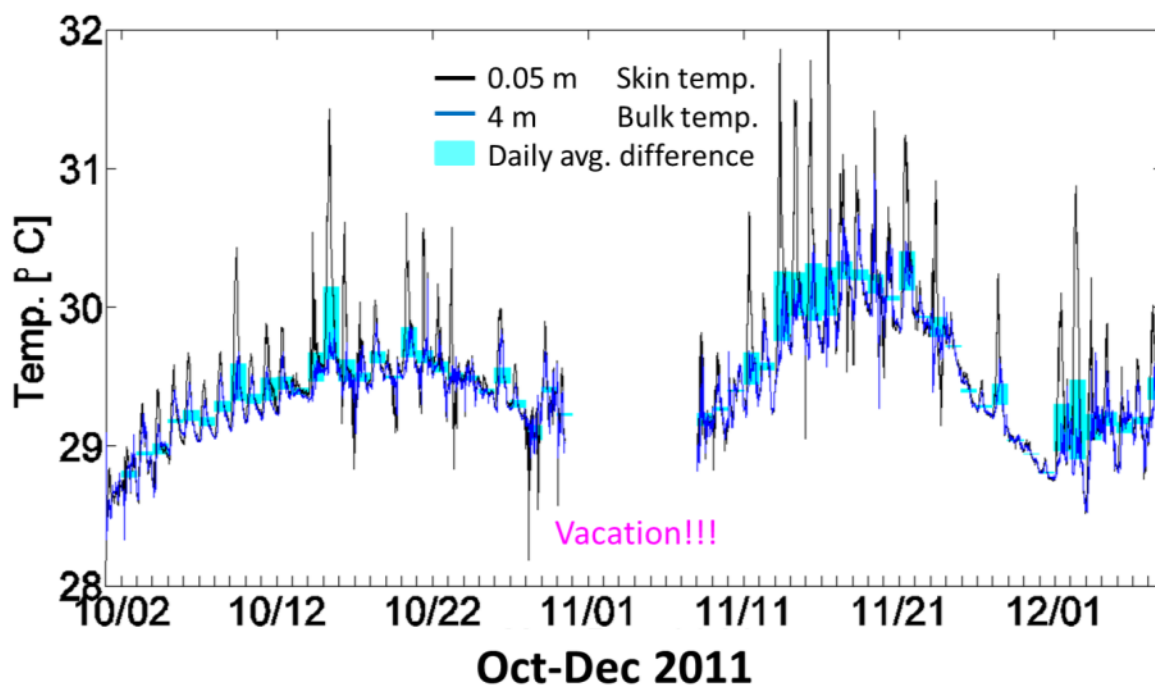


**Figure 3.9.** Observed 0.05 m skin temperature, 4 m thermosalinograph temperature, and the daily average difference between temperatures at these two depths. An intraseasonal signal in the daily average warm layer is apparent in the observations.

A histogram of the daily average observations from Figure 3.10 illustrates the difference between the 4 m deep Thermosalinograph, and the interface temperature modeled in COARE from the 0.05 m sea snake (Figure 3.9). While the warm layer and cool skin corrections almost always have opposite signs, it is rare that the daily average values balance exactly so that the 4 m temperature is representative of the air-sea interfacial temperature. In fact, most often the 4 m temperature is actually warmer than the interface temperature because of the prolific cool skin and the tendency for the warm layer to mix out in the presence of winds greater than a few m/s. Though a 1 m or 0.5 m temperature is commonly used for daily average fluxes, the 4 m temperature is a direct observation, while the 1 m or 0.5 m temperatures must be modeled in COARE with the

warm layer code. The 4 m temperature illustrates the same principle and differences cannot be attributed to warm layer model uncertainties.

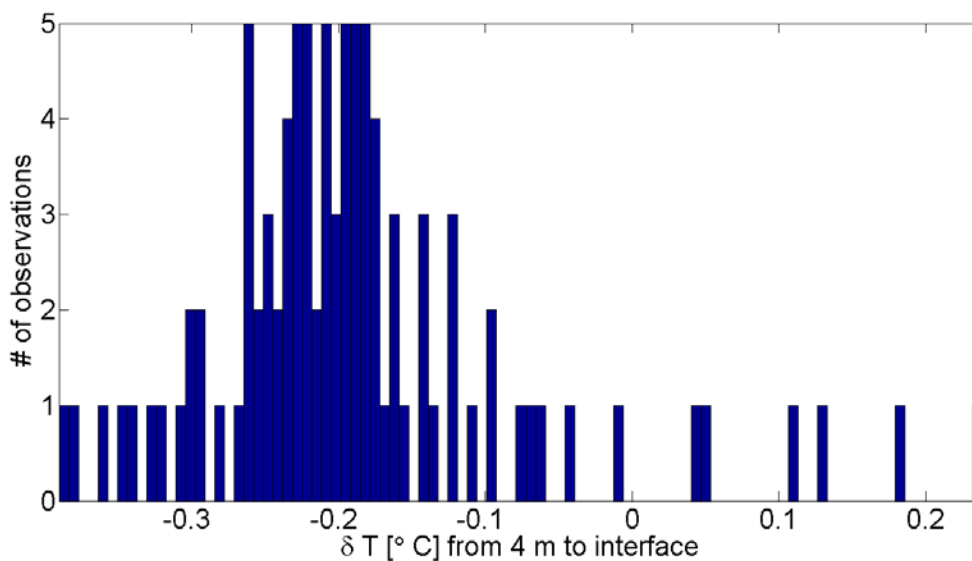


**Figure 3.10.** Histogram of the temperature correction required from the observed 4 m thermosalinograph and the skin temperature modeled in COARE from the 0.05 m sea snake observations. There are 95 realizations and 95 data bins.

### 3.5.2.1 *Satellite Sea Surface Temperature Retrievals*

Gridded flux products use a subsurface sea temperature to compute fluxes that has been adjusted from satellite measurements of SST to approximate the buoy measurements at  $\sim 1$ m depth. Changes in mixed layer bulk sea temperature occur on a relatively long time scale because of the high heat capacity of water. Satellite imagery measures skin SST (at different depths for infrared and microwave imagery) that can vary on shorter time scales. However, the effective depth of the SST measurement, the time of day, and the decision to measure or adjust for diurnal warming all affect the ocean temperature retrievals provided by satellite SST measurements.

Satellite mounted infrared (IR) radiometers detect SST with good spatial and temporal resolution. Satellites equipped with Advanced Very High Resolution Radiometers (AVHRR) infrared radiometers were first launched in 1978, with improved generations launched in 1981, and 1998. This makes for a conveniently long record of global SST estimates with a footprint size of 1-5 km and a measurement depth of  $\sim 1 \mu\text{m}$  (Reynolds, et al. 2002). A major limitation of infrared SST retrievals is that clouds obscure the sea surface and hence make sea surface temperature measurements sparse over large areas of the globe at any given time. Clouds appear cold against the background of the relatively warm sea surface, and are therefore easily filtered out of the dataset. Though the AVHRR SST record is long, the quality of estimates can be compromised by atmospheric effects from water vapor and aerosols, even in the absence of clouds. Atmospheric contamination can be difficult to identify and remove because the signature can be very similar to that of the sea surface in the tropics, where atmospheric water vapor content is high (Wentz and Chelton, 2014).

Microwave wavelengths pass through clouds, and measure surface temperature at  $\sim 1 \text{ mm}$  depth, and therefore see a combination of the cool skin and the uppermost part of the warm layer. Microwave SST has only been measured since 1997. Compared to infrared SST, microwave SST have a relatively short data record, limited spatial coverage, and a wide sensor footprint (low resolution) of  $\sim 50 \text{ km}$ . The Tropical Rainfall Measuring Mission (TRMM) satellite was launched with an orbit inclination of  $45^\circ$  in 1997. It is equipped with the TRMM Microwave Imager (TMI), which measures SST at a cloud penetrating frequency of 10 GHz. This instrument provides the unique opportunity to study the diurnal warm layer in tropical oceans where cloud fraction is highly variable.

TRMM completes 16 passes daily in a non-sun synchronous orbit which ranges from  $\pm 35^\circ$  of the equator. (<http://www.remss.com/missions/tmi>)

When adjusted to 0.5 m or 1 m standard depths, analyzed satellite SST estimates can be compared with and validated by buoy observations of ocean temperature. These depths are convenient for standardization and verification purposes with climate records that employ in situ sea temperature observations (e.g. COADS, Woodruff, et al. 1998), because in situ observations are frequently measured at a nominal 1 m depth by a bucket or buoy. Reynolds optimally interpolated near surface temperature (NST) products used by OAFlux are intended to estimate sea temperatures representative of 0.5 m depth (Jin & Weller, 2008b; Reynolds et al., 2007). ERA-I (and consequently TropFlux) uses the Operational Sea Surface Temperature and Sea-Ice Analysis 1 m depth temperature estimate.

It is complicated and often unnecessary to include the diurnal warming and cooling processes of the upper few meters in the ocean heat budget, because this variability is not representative of the ocean mixed layer. However, the shallow skin depth of satellite measurements are likely to sample diurnal warm layers. For this reason many satellite SST products attempt to estimate and adjust for diurnal warming of the upper few meters. Common methods include using only nighttime retrievals, down-weighting daylight retrievals, or modeling a foundation temperature which is unaffected by surface processes.

## **3.6 METHODS AND RESULTS**

### **3.6.1 Solar Radiation Model**

One way to include both corrections using daily data is to use a model for solar radiation. Since the zenith angle of the sun is known as the sun rises and sets each day, the daily average solar insolation can be distributed over the daylight hours by the cosine of zenith angle. At low latitudes, a half cosine over 12 daylight hours is a good approximation to the distribution of solar radiation. A sample of 7 days of observed SWR and the solar model are shown in Figure 3.11. This could be refined to reflect changes in daylight hours with latitude and time of year. However, this simple model is sufficient in the tropics. This changing solar flux approximates the diurnal cycle, and includes the mean effect of clouds—though not their instantaneous effect on the radiation, which is a sufficient approximation to the slowly evolving integrals of solar absorption that affect the diurnal warm layer. Implementation of the warm layer correction using daily averaged data is achieved by calculating fluxes hourly with the solar model, with all other variables set at the daily average value.

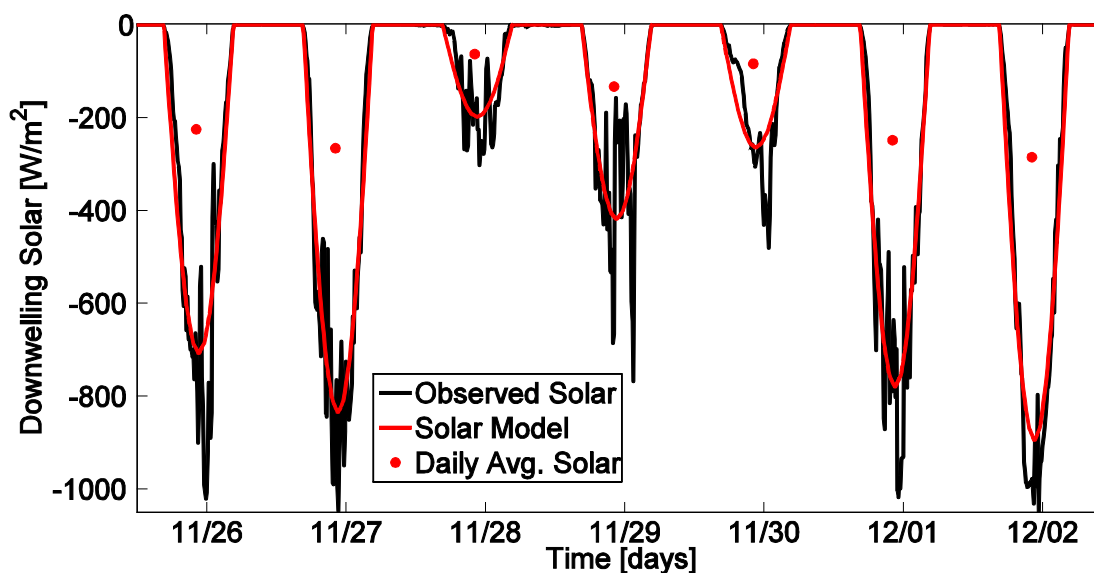


**Figure 3.11** The simple solar model approximates the diurnal cycle by distributing the daily average shortwave radiation in a half cosine throughout 12 hours in the day. 7 days of observed 10 minute SWR from the *Revelle* and the corresponding solar model are shown.

### 3.6.2 Sensitivity experiments to the Warm layer/Cool skin with *Revelle* DYNAMO data

Fluxes were computed with observations from the R/V *Revelle* using 11 different experimental configurations to quantify the error associated with neglecting the warm layer and cool skin corrections, and the effectiveness of the solar model. These experiments vary the choice of sea temperature used to estimate the SST, whether to use warm layer and cool skin corrections, and whether to use observed solar radiation or daily the average solar radiation via the solar model. The sea temperature options are the 1 m temperature (modeled using the COARE algorithm from the ship thermosalinograph at 4 m depth), and the observed temperature at 0.05 m depth.

Table 3.1 lists the names, resolution, use of the cool skin and warm layer correction, solar forcing, and sea temperature depth for all flux estimate experiments studied in this thesis. Since there are many cases with subtle differences, an abbreviation system is adopted to describe each experiment completely. The cases using 10-minute observations are named without any prefix, while cases for daily resolution are prefaced with a *D* for daily resolution. A lowercase *c*, *w*, or *s* indicates the cool skin, warm layer, and solar parameterization in COARE 3.5. A capital *O* indicates the phenomenon is observed, *M* indicates it is modeled with the COARE model, and *I* indicates it is ignored; these qualifiers follow the parameterization letter to indicate the treatment in each experiment. The SST depth is indicated by *t* followed by the measurement depth in meters. The cool skin does not depend on accumulated solar radiation and is therefore less sensitive to the 10 minute fluctuations. To isolate the effects of the warm layer, independent of the effectiveness of the solar model, the observed solar radiation was used for all cases when the warm layer is ignored.

Fluxes computed using the temperature measured at 0.05 m depth are considered the *best estimate* of sensible and latent heat flux. The cool skin is modeled for these, but the warm layer in the near subsurface is essentially observed because warming above 0.05 m depth is negligible. Fluxes computed with a 1 m “SST” but ignoring both the warm layer and cool skin corrections are considered the *worst estimate*. Currently, daily average gridded and buoy fluxes are all computed using the worst estimate configuration. The effect of the physics and their parameterizations is illustrated by their difference from either the *best estimate* or the *worst estimate* control experiments.

**Table 3.1.** *Revelle* Experiment names, resolution, and sea temperature (ST) depth used for all variations. The warm layer, cool skin and solar input can be Modeled, Ignored, or Observed, indicated by an M, I, O.

Name	Resolution	Cool skin	Warm layer	Solar input	ST depth
cMwOsOt0.05	10 min	M	O	O	0.05 m
cMwMsOt1	10 min	M	M	O	1 m
cMwMsMt1	10 min	M	M	M	1 m
cMwIsOt1	10 min	M	I	O	1 m
clwOsOt0.05	10 min	I	O	O	0.05 m
clwMsOt1	10 min	I	M	O	1 m
clwIsOt1	10 min	I	I	O	1 m
DcMwOsOt0.05	Daily	M	O	O	0.05 m
DcMwMsOt1	Daily	M	M	O	1 m
DcMwMsMt1	Daily	M	M	M	1 m
DclwIsOt1	Daily	I	I	O	1 m

Figure 3.12 shows the 10-minute and daily resolution fluxes. *Best estimate* fluxes are on the x-axis, and the difference between the *worst estimate*, and *best estimate* fluxes are on the y-axis. The difference can be interpreted as the error induced by ignoring both corrections. In the 10-minute fluxes, both SHF and LHF biases change non-linearly as the magnitude of the flux increases. While low fluxes can be overestimated or underestimated, high fluxes are always overestimated. Much of the noise averages out in the daily fluxes; however, an increasing trend with increasing flux is still evident, at least in latent heat flux.

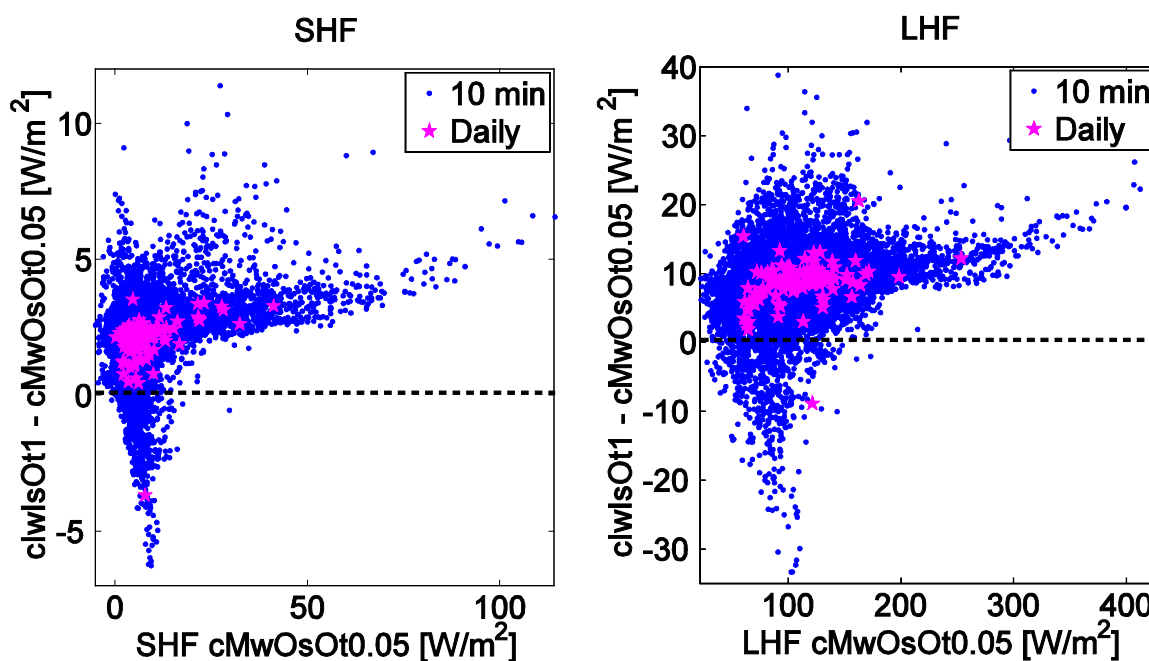


**Figure 3.12.** Heat flux difference between the best estimate from 10 min observations and worst estimate from daily averages, as a function of the sensible heat flux, computed with 10 minute resolution (blue dots) and averaged to daily resolution (pink stars) for (a) sensible heat flux and for (b) latent heat flux.

In Figures 3.13 and 3.14, the *worst estimate* bias is shown in black. The new bias is plotted in color on top of the worst estimate bias, as the warm layer (Figures 3.13a and 3.14a) and cool skin corrections (Figures 3.13b and 3.14b) are turned on individually, and as both are turned on in Figures 3.13c and 3.14c. Figures 3.13a and 3.14a show that realizations with negative errors are reduced when the warm layer is modeled. Negative errors result from ignoring the warm layer during daylight hours under light wind conditions. In the daily average these negative errors are balanced by positive errors associated with ignoring the ever-present cool skin. Panels 3.13b and 3.14b show that the positive bias is reduced when the warm layer is ignored, but the cool skin modeled. Finally, when both the warm layer and cool skin corrections are modeled, the bias hovers around zero with no significant trend with increasing flux magnitude (Figures 3.13c and

3.14c). This process illustrates how ignoring the warm layer and cool skin corrections both introduce systematic biases that need not cancel, affecting the mean flux estimate and artificially increasing the variability in the flux estimates.

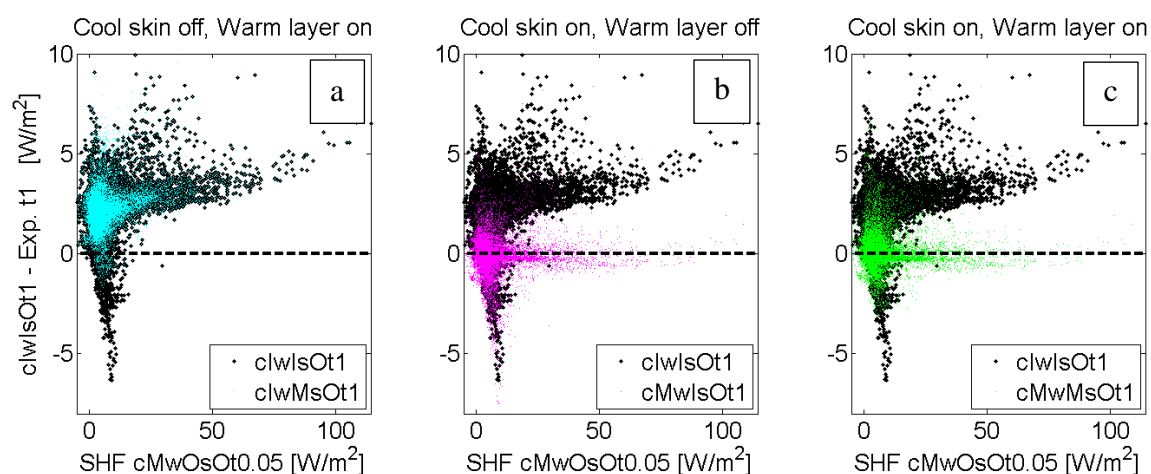


**Figure 3.13.** The black dots in all 3 panels show the error induced by ignoring the warm layer and cool skin corrections when using a 1 m SST. The cyan dots in panel a show the bias when the warm layer is modeled, but the cool skin is ignored. The pink dots in panel b show the bias when the cool skin is modeled, but the warm layer remains ignored. The green dots in panel c illustrate bias when both the cool skin and the warm layer corrections modeled.

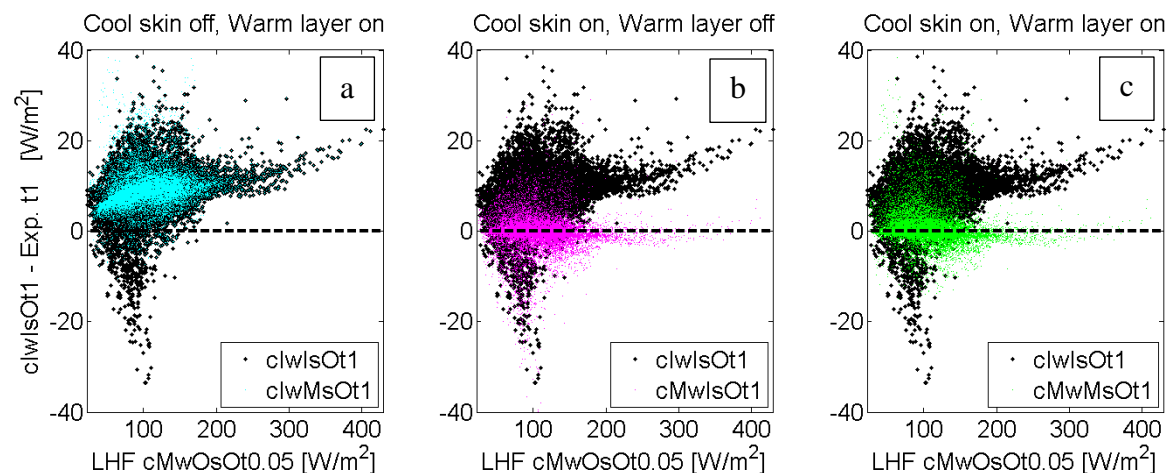


**Figure 3.14.** As in Figure 3.8, but for LHF.

These controlled experiments reveal the source and magnitude of biases associated with various methods of computing fluxes with COARE. The mean over the entire data set is compared for sensible and latent heat fluxes for the 11 experiments (Figure 3.15). The error is estimated by comparison with the fluxes computed by the *best estimate* SST as shown by the dashed line in Figure 3.15. Ignoring the cool skin correction (*cl*) introduces the largest error regardless of other choices, and results in a systematic overestimate  $\sim 2 \text{ W/m}^2$  (25% of the mean) and  $\sim 9 \text{ W/m}^2$  (8% of the mean) for sensible and latent heat flux, respectively. The error incurred by changing any of the other parameterizations is very small (mean bias  $< 1 \text{ W/m}^2$  for all cases).

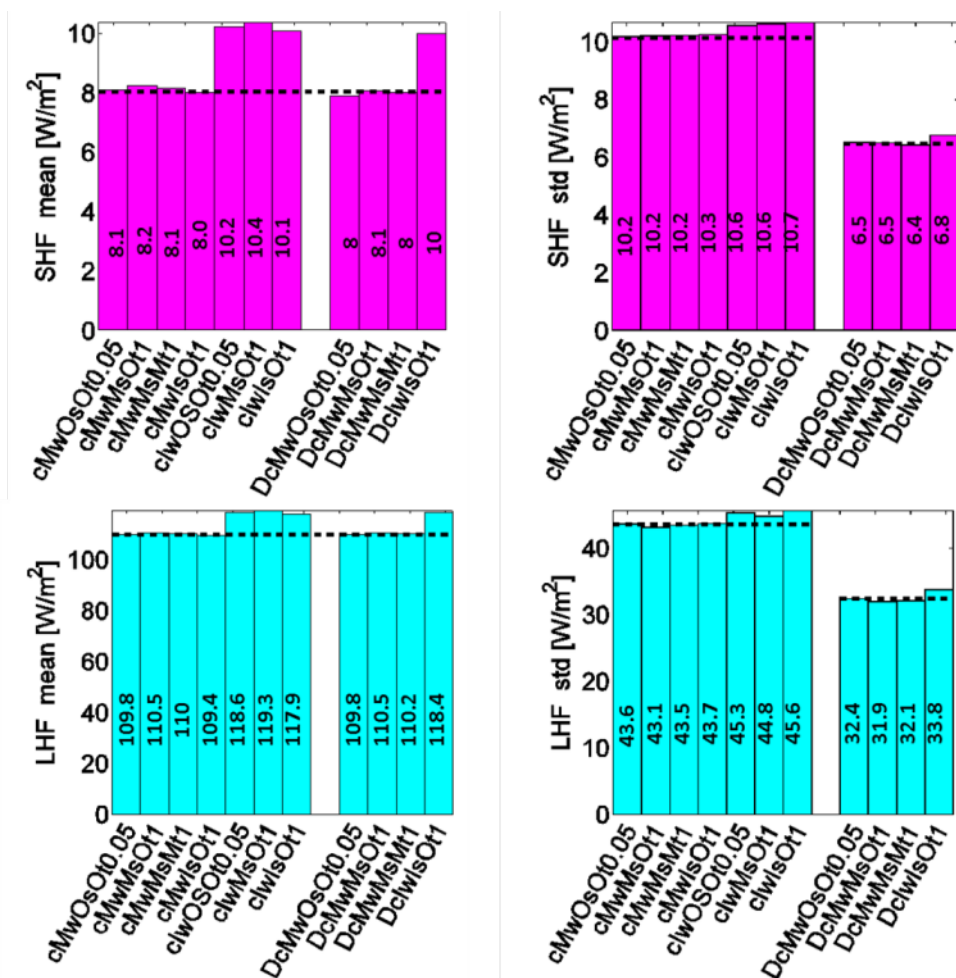


**Figure 3.15.** On the left the mean of all *Revelle Experiments* are shown for SHF on the top, and LHF on the bottom. The Right panels show the standard deviation of each experiment. Ignoring the cool skin correction makes the biggest difference in both the mean and standard deviation for latent and sensible heat fluxes. The dashed lines represent the value computed from our *best estimate* of SST.

By increasing SST when winds are light (and fluxes are weak) the warm layer increases the minimum flux and increases the flux variability. Ignoring the warm layer correction serves to broaden the range of flux estimates resulting in an overestimate of flux variability. Though the increase in standard deviation is small, (0.3 – 0.5 W/m<sup>2</sup> for sensible heat, 1.4 – 2 W/m<sup>2</sup> for latent heat, for daily and 10 minute resolution respectively when compared to the *best estimate*), the overestimation is on the order of 5% of the total flux variability for sensible and latent heat fluxes. It is valuable to be able to quantify

such systematic errors when they exist. The results of the *Revelle* experiments indicate that bias and variability errors can be reduced to less than  $0.1 \text{ W/m}^2$  for sensible, and less than  $0.3 \text{ W/m}^2$  for latent heat by including the warm layer and cool skin effects, and these effects can easily be included for daily data using the solar model.

### 3.6.3 A table of warm layer and cool skin corrections

To further illustrate the effects of the warm layer and cool skin corrections on fluxes, and reduce the computation time required to implement these corrections using daily average data, lookup tables for the daily average sensible and latent heat fluxes, and cool skin and warm layer corrections to SST are constructed (Figures 3.16-3.17). The lookup table is constructed by an idealized calculation in which the air-sea temperature difference and the moisture are all held constant ( $T_{air} = 28^\circ\text{C}$ ;  $T_{sea} = 29^\circ\text{C}$ ;  $RH = 80\%$ ). Wind speed is varied from 0-10 m/s. Daily average insolation varied between 40-400  $\text{W/m}^2$  for 37 solar cycles. Fluxes were computed with the COARE version 3.5 algorithm with and without the warm layer and cool skin corrections at hourly resolution using the solar radiation model described in Chapter 3.6.2. The results are binned by 0.3 m/s wind speed increments and 20  $\text{W/m}^2$  daily average solar radiation increments.

Figure 3.16a, shows the daily average sensible heat flux computed without the warm layer and cool skin corrections. The flux primarily scales with wind speed, with weak dependence on daily average short wave radiation. The range of fluxes (given the chosen parameterizations) spans slightly less than  $1 \text{ W/m}^2$  to about  $10 \text{ W/m}^2$ . Figure 3.16c shows the net correction that should be added to SHF given daily average solar and wind speed conditions. The correction ranges from slightly less than  $-2.5 \text{ W/m}^2$  to  $1.5$

$\text{W/m}^2$ . The largest positive corrections (due to a well-developed warm layer) are required when the mean flux is relatively small, so that the correction is  $O(30\%)$  of the mean flux. The largest negative corrections (due to cool skin dominance) occur when fluxes are relatively high, and amount to  $\sim 25\%$  decrease in the mean flux. The transition from the cool skin being the most important to the warm layer having a larger effect starts when  $\text{SWR} > \sim 200 \text{ W/m}^2$  for wind speeds  $< \sim 2 \text{ m/s}$ . Figure 3.16b and d show the same results for latent heat flux. Similar patterns exist with strong linear dependence on wind speed and very slight dependence on solar radiation. The positive corrections amount to  $\sim 15\%$  of the mean flux, while the negative corrections only decrease the mean flux by  $\sim 5\%$ .

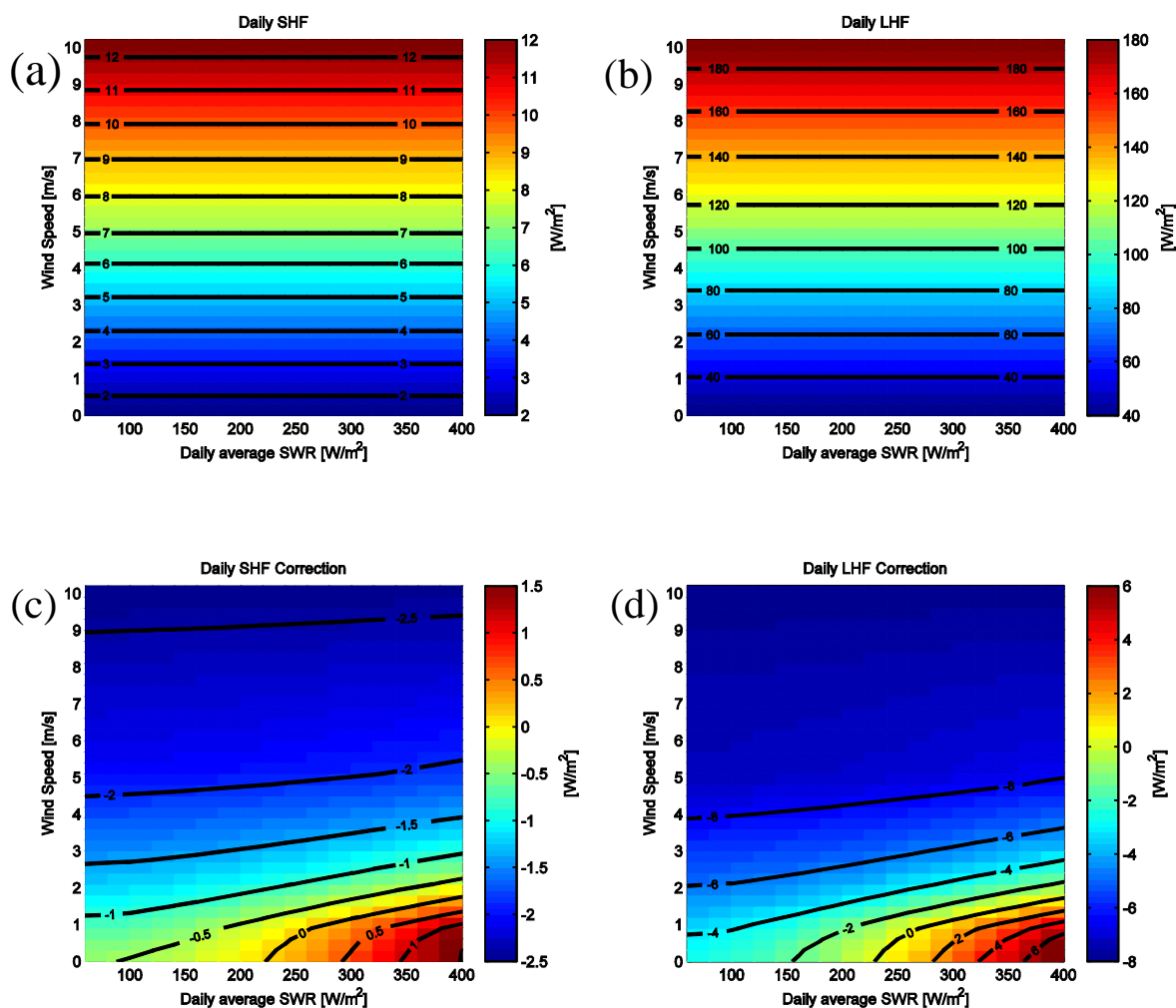


**Figure 3.16.** Daily average SHF (a) and LHF (b), without the warm layer and cool skin corrections, and SHF (c) and LHF (d) corrections with the warm layer and cool skin corrections turned on; binned by wind speed and daily average short wave radiation

The warm layer correction (Figure 3.17a) represents the adjustment required from 1 m depth to the viscous sublayer, and the cool skin (Figure 3.17b) adjusts for cooling within this layer; combined these corrections yield an estimate of the adjustment required to achieve an interface temperature from a 1 m estimate. Warm layer development is primarily dependent on wind speed, with moderate dependence on daily average solar radiation. The presence of a warm layer serves to enhance both fluxes by a few W/m<sup>2</sup>.

However, the largest corrections are required when the wind speed exceeds  $\sim 5$  m/s, the warm layer is mixed out, and the cool skin becomes the most important factor. Figure 3.17a shows that wind speeds greater than  $\sim 2.5$  m/s are sufficient to mix out the daily average warm layer, even in the presence of strong insolation. However, daily average solar radiation in excess of  $300 \text{ W/m}^2$  is required to produce a daily average warm layer of the same magnitude as the cool skin, even at extremely low wind speeds. In Figure 3.17b, the (negative) cool skin SST correction scales mostly with wind speed, with a weak linear dependence on daily average solar radiation. In the presence of strong solar radiation and weak winds, the cool skin depth increases, and more energy is absorbed in the cool skin depth which slightly compensates the cooling across the layer. This results in the smallest (negative) cool skin correction,  $\sim 0.16 \text{ K}$ , coincident with the largest (positive) warm layer correction,  $\sim 0.7 \text{ K}$ . The resulting net correction would be  $\sim 0.5 \text{ K}$ , equivalent to 50% of the prescribed sea-air temperature difference used to construct these tables.

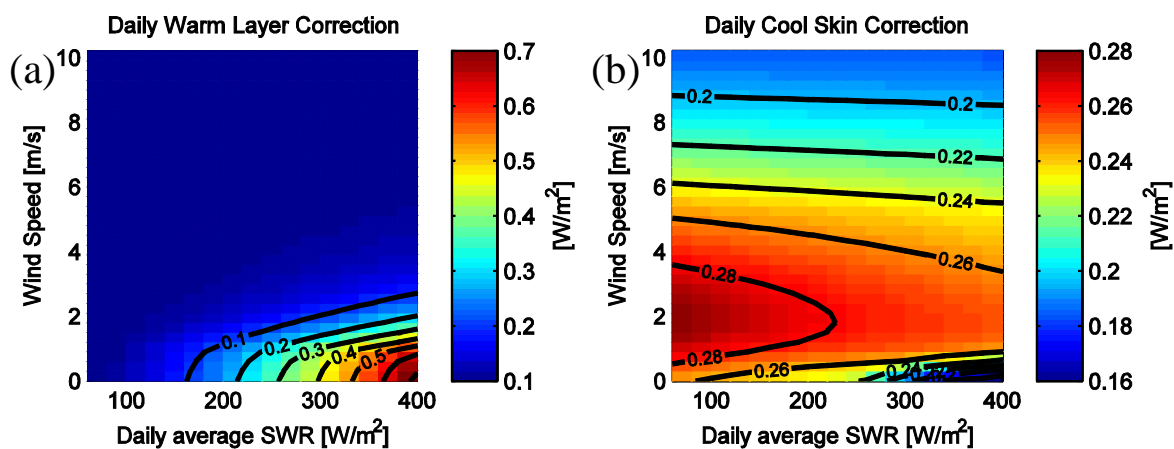


**Figure 3.17.** Daily average warm layer (a) and cool skin (b) corrections to adjust from 1 m to the interface temperature binned by wind speed and daily average short wave radiation.

### 3.6.4 Comparison of the 80.5° E, 0° N RAMA Buoy to the Revelle

The R/V *Revelle* was stationed approximately 3 km from the 80.5° E, 0° N RAMA buoy for a total of 52 days during the DYNAMO intensive observation period. Presumably, fluxes computed from these data sets should agree well during this time. The buoys measure sea temperature at 1 m depth and therefore should employ the warm layer and cool skin corrections when computing fluxes. The NOAA data portal offers daily and sub-daily fluxes computed with COARE. The sub-daily fluxes include both corrections when radiation data is available; however, both corrections are turned off for all daily average buoy flux products. In order to properly assess agreement between the R/V *Revelle* and the RAMA buoy, the fluxes are computed from hourly R/V *Revelle* and RAMA data including both corrections. The multitude of experiments in section 3.6.1.1 is not repeated for the buoy, but the daily RAMA fluxes omitting both corrections are shown to illustrate the error. For each method of computing fluxes with the RAMA data, the mean bias, standard deviation, and correlation are computed with respect to R/V *Revelle* daily average fluxes. Finally these statistics are recomputed and compared at daily resolution.

The mean differences between RAMA and R/V *Revelle* sensible and latent heat flux with the corrections turned on are 0.2 W/m<sup>2</sup> and 4.6 W/m<sup>2</sup> respectively. The biases increase to 1.9 W/m<sup>2</sup> and 11.4 W/m<sup>2</sup> for sensible and latent heat flux, respectively, when the warm and cool corrections are turned off. These differences are larger than the errors seen in the *Revelle* experiments because two independent data sets are being compared

rather than data from a single system, but different methods as with the *Revelle* experiments. Variability of both hourly and daily average fluxes is overestimated when the warm layer and cool skin corrections are ignored. Figure 3.18 shows bar plots of sensible and latent heat flux, mean and standard deviation computed from R/V *Revelle* data with the warm layer and cool skin corrections turned on, as well as fluxes computed from the 80.5° E, 0° N RAMA buoy for 40 days when data was available from both the ship and the buoy. The cyan bars include the warm layer and cool skin corrections, while the pink bars include neither. Without the warm layer and cool skin corrections, the RAMA buoy overestimates both latent and sensible heat in hourly and daily fluxes. Including both corrections brings the estimates substantially closer. Results are qualitatively consistent with the R/V *Revelle* experiments that show ignoring the cool skin correction produces the highest overestimation of both latent and sensible heat fluxes. The RAMA variability also increases when these corrections are ignored, though the R/V *Revelle* variability is yet  $1 \text{ W/m}^2$  (SHF), and  $4.7 \text{ W/m}^2$  (LHF) higher than the RAMA fluxes without the corrections.

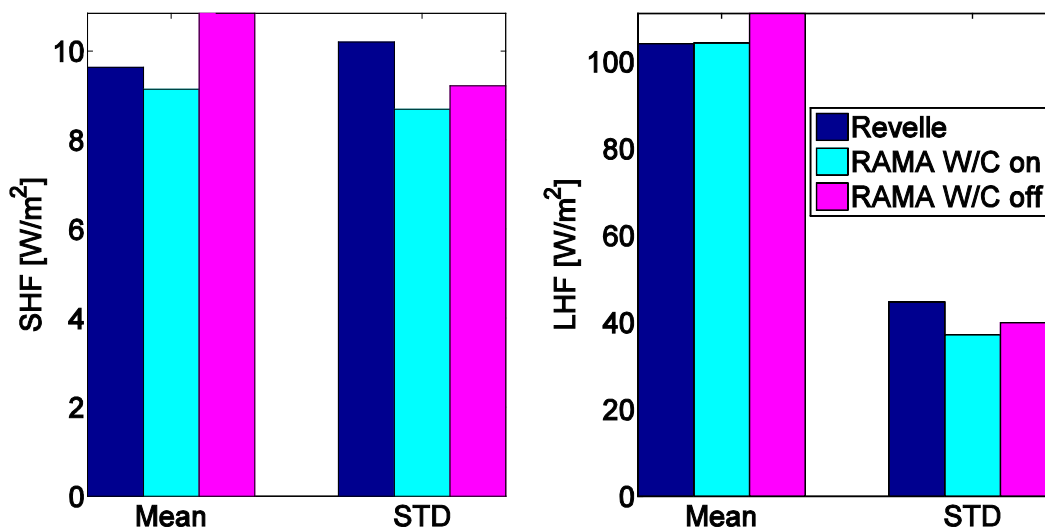


**Figure 3.18.** Sensible and latent heat flux mean and standard deviation computed with the *Revelle* data with the warm layer and cool skin corrections on, compared to the closest RAMA buoy at 80.5° E, 0° N, computed with, and without warm and cool corrections.

Table 3.2 lists the mean and standard deviation of the R/V *Revelle* daily average fluxes computed from both daily and hourly data. The mean is the same, and the daily average variability is reduced. Table 3.3 lists the mean, standard deviation, bias and correlation of RAMA with respect to the R/V *Revelle* fluxes. Hourly and daily estimates of both latent and sensible heat flux are remarkably well captured by the buoy fluxes when both corrections are employed. However, the biases nearly triple when these corrections are ignored. Looking only at the RAMA buoy fluxes, the variability is slightly overestimated for latent and sensible heat flux for hourly and daily fluxes when these corrections are ignored. This is consistent with results from the R/V *Revelle* experiments that show overestimation of high fluxes from ignoring the cool skin, and underestimation of weak fluxes from ignoring the warm layer.

**Table 3.2.** *Revelle* hourly mean and standard deviation are computed with the warm layer and cool skin corrections on. Hourly resolution fluxes are averaged to daily and the std is recomputed.

<i>Revelle</i>	SHF		LHF	
	mean	std	mean	std
Hourly	9.6	10.2	104	44.7
Daily	9.6	7.1	104	34.4

**Table 3.3.** RAMA hourly mean, standard deviation and correlation with *Revelle* fluxes computed with the warm layer and cool skin corrections on and off. Hourly resolution fluxes are averaged to daily and the std and correlation with the *Revelle* are recomputed.

RAMA	SHF				LHF			
	mean	std	bias	cc	mean	std	bias	cc
Hourly W/C on	9.1	8.7	0.18	0.93	104	37	4.63	0.85
Hourly W/C off	10.8	9.2	1.89	0.92	111	40	11.4	0.85
Daily W/C on	9.2	5.9	0.37	0.68	104	26	4.1	0.77
Daily W/C off	10.8	6.4	1.91	0.67	112	30	11.6	0.75

### 3.6.5 Gridded Flux Product Comparison

TropFlux and OAFlux are compared with 96 days of bulk fluxes from the R/V *Revelle*, and 69 days of bulk fluxes from the R/V *Moana Wave*. In situ observations from the research vessels and the three APL buoys were withheld from modeling and reanalysis efforts and data correction schemes. These independent observations can be used to assess the accuracies of OAFlux and TropFlux. The R/V *Revelle* was stationed closest (~3 km) to a RAMA buoy for 52 days of the DYNAMO IOP. The R/V *Revelle* made transects to  $\pm 2^\circ$  latitude along  $80.5^\circ$  E longitude, and East/West along the Equator to  $90^\circ$  E at the end of leg 3 during which time the grid cell nearest to the daily average location of the ship was used for comparison. The R/V *Moana Wave* was stationed 188 km south of the  $156^\circ$  E,  $0^\circ$  N TAO buoy for the duration of the TOGA-COARE IOP in 1992-1993. The APL buoys were located along  $79^\circ$  E longitude at  $0^\circ$  N,  $1.5^\circ$  S, and  $9.5^\circ$  S. They varied from 166 km (for the equator and  $1.5^\circ$  S buoys), to 244 km (for the  $9.5^\circ$  S

buoy) from the nearest RAMA buoys. Observations from all of these platforms offer opportunities to assess the gridded flux products.

Two related questions are investigated:

- 1) How well do gridded fluxes replicate observations in the vicinity of a buoy?
- 2) How well do gridded fluxes replicate observations in regions where in situ surface observations ingested into ECMWF reanalysis are sparse?

### ***3.6.5.1 Effect of Distance from a TPR Buoy on Gridded Flux Estimates***

Time series of OAFlux, TropFlux and in situ fluxes from the R/V *Revelle*, and the R/V *Moana Wave* from the DYNAMO and TOGA-COARE field experiments are shown in Figure 3.19. Time series for the three APL buoys deployed during DYNAMO are shown with the corresponding OAFlux and TropFlux estimates in Figure 3.20. Gridded sensible and latent heat fluxes generally track observations, though the gridded latent heat fluxes are consistently higher than those from the R/V *Moana Wave*. The R/V *Revelle* was ~3 km from a TPR buoy, while the R/V *Moana Wave* was 188 km from a buoy.

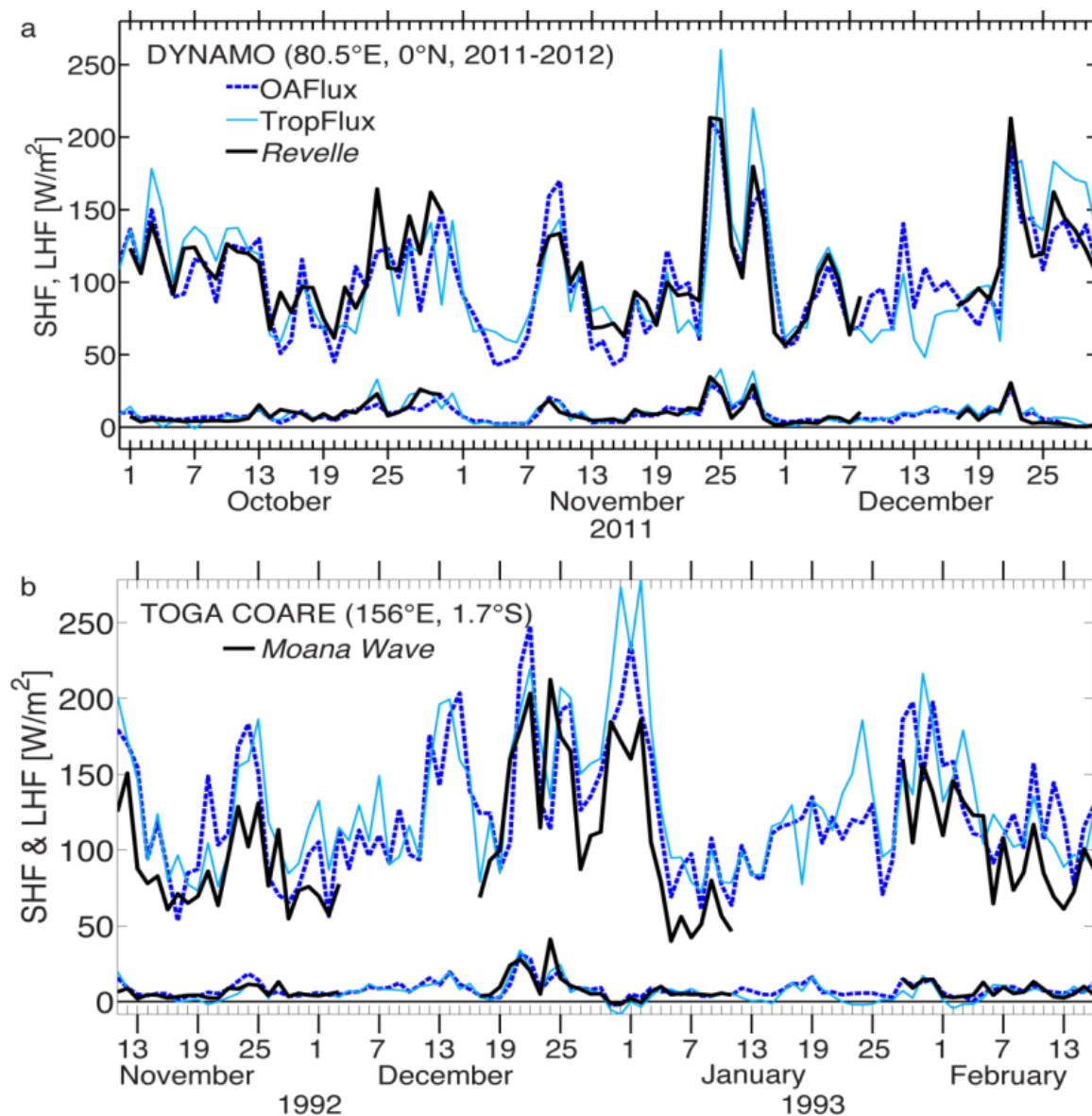


**Figure 3.19.** Sensible and latent heat fluxes computed from in situ data collected on the *Revelle* and the *Moana Wave* plotted with the OAFlex and TropFlux at the nearest grid cell to the location of each ship at the time.

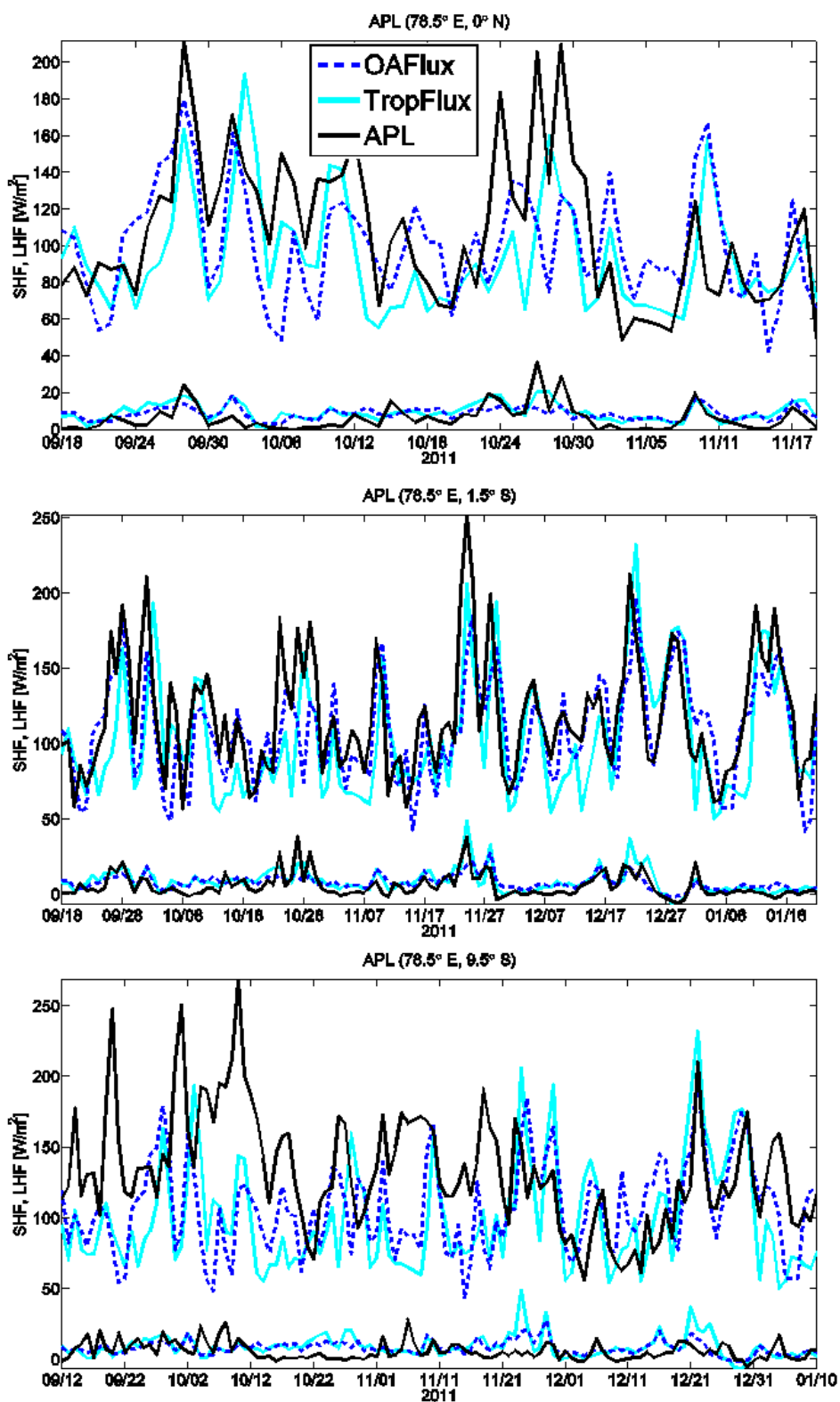


**Figure 3.20.** As in Figure 3.19, except using the APL buoys located at 78.5° E and 0° N, 1.5° S, and 9.5° S. Note different time axes.

Agreement between gridded products and observations degrade with distance from the location where reanalyses assimilate in situ data. The 9.5° S buoy location shows the poorest agreement of the time series in Figure 3.20 (the closest RAMA buoy is 80.5° E, 8° S). While SHF is consistently overestimated by gridded products, LHF is consistently underestimated.

Figure 3.21 shows the mean and standard deviation of fluxes from the 3 APL buoys and the R/Vs *Revelle* and *Moana Wave*. The only time series that is consistently well captured in the mean by both gridded products is the R/V *Revelle*, which was stationed ~ 3 km from a RAMA buoy source assimilated into the reanalyses used to produce OAFlux and TropFlux. The standard deviation of both SHF and LHF are poorly captured by both gridded products at most locations. TropFlux captures the variability of both fluxes at the 1.5° S APL buoy, and LHF at the 9.5° S buoy. Variability is most often underestimated by OAFlux, and is equally likely to be under or overestimated by TropFlux.

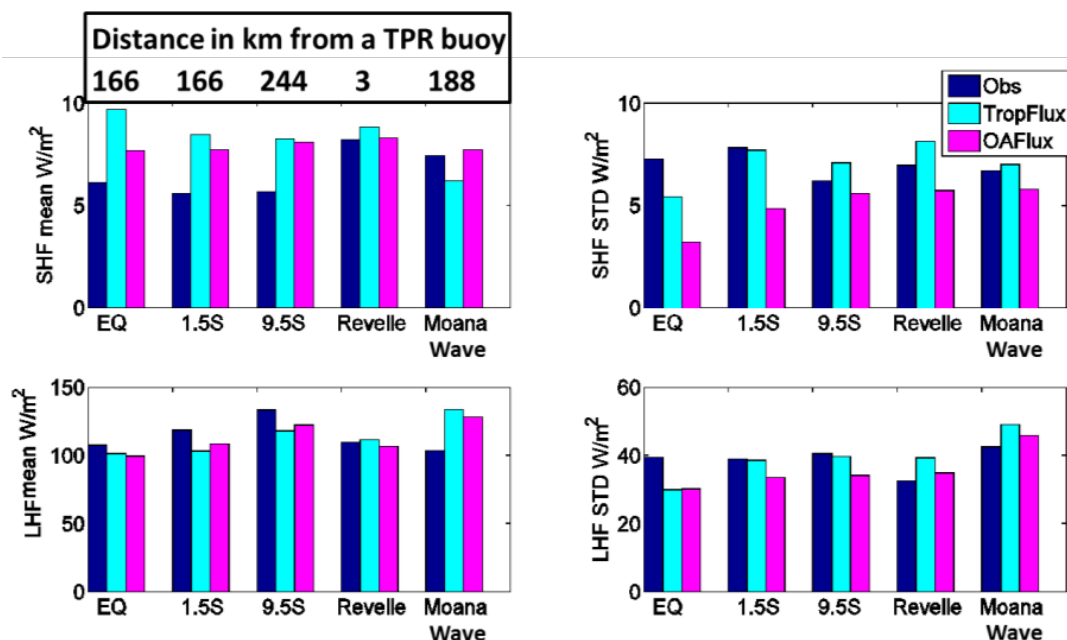


**Figure 3.21.** The mean and standard deviation of SHF and LHF compared between independent in situ observations and TropFlux and OAF flux. The *Revelle* was stationed closest to a TPR buoy (3 km). The equator and 1.5° S APL buoys were next closest (166 km) followed by the *Moana Wave* (188 km). The 9.5° S APL buoy was farthest from a TPR buoy (244 km).

Fluxes far from TPR buoys (~200 km) are poorly captured in the mean, while the R/V *Revelle* fluxes are well captured. The sample size is extremely limited, however (only one data series within 5 km of a RAMA buoy, and four O 150-250 km from a TPR buoy), and this analysis could be bolstered by additional independent observations both near and far from in situ data sources. The histograms in Figure 3.7 corroborate these findings by noting that the root mean square differences between flux estimates of OAF flux and TropFlux increase when all common locations are considered compared to only buoy locations. It is expected that the assimilation of observations into reanalyses improves local flux estimates based on the reanalysis, but does little to constrain fluxes ~200 km away.

Table 3.4 shows the root mean square error for both gridded products with respect to the R/V *Revelle* fluxes (~3 km from a RAMA bouy) and the APL and *Moana Wave* fluxes (over 160 km from TPR buoys). The root mean square difference (RMSD) between OAFflux and TropFlux at buoy locations, and at all other locations are also shown.

**Table 3.4.** The root mean square difference, and % difference of the mean flux between OAFflux and TropFlux is compared for sites near, and far from in situ buoy data sources. 3 km from a buoy corresponds to a single time series form the *Revelle*. 160-240 km from TPR includes three APL buoys and the *Moana Wave*. The last column is all grid cells that have a TPR buoy compered to all that do not.

	3 km from TPR		160-240 km from TPR		OAFflux - TropFlux	
	TropFlux	OAFflux	TropFlux	OAFflux	At TPR	Not at TPR
SHF RMSD [ $W/m^2$ ]	0.6	0.1	2.6	1.6	4.8	7.1
SHF RMSD/Mean (%)	7%	1%	46%	28%	43%	64%
LHF RMSD [ $W/m^2$ ]	1.9	3.1	16.7	13.3	25.4	30
LHF RMSD/Mean (%)	2%	3%	14%	11%	21%	25%

### 3.6.5.2 TPR Bias Corrections

TropFlux removes biases from the ERA-I data before computing bulk fluxes. TropFlux bias corrections to ERA-I variables were systematically developed based on climatological mean TPR observations over the ten year period 2000-2009. During this period, the Atlantic and Pacific basins were well represented by the TAO and PIRATA arrays. However, since the majority of RAMA buoys were not operational until 2009, the Indian Ocean remained poorly sampled. Though the RAMA array remains incomplete at

the time of this writing, 25 RAMA buoys are now transmitting data. Kumar et al. (2012) describes the bias and amplitude corrections applied to ERA-I to create TropFlux.

Collectively, the bias and amplitude corrections in TropFlux produce flux estimates that show better agreement with independent in situ observations than ERA-I fluxes (Kumar et al., 2012b). However, there is significant uncertainty in the biases of some of the variables. To further quantify these bias values, a similar analysis was done using TropFlux variables (used as input to the flux calculation) compared to TPR observations over a different time period in which all three major ocean basins were well represented. Buoys were averaged from 2009-2013 and compared to TropFlux input variables. This analysis was done with the bias-corrected TropFlux variables. So if the corrections were accurate, the TropFlux bias with respect to the TPR array should have a near zero mean. Over the five year period, compared to the TPR buoys, bias-corrected TropFlux specific humidity was higher by +0.28 g/kg and TropFlux wind speed was higher by +0.5m/s. This discrepancy suggests that the bias correction values (0.79 g/kg and 0.28 m/s) may not be very accurate.

A random sampling procedure is designed to determine if differences in bias resulted from sampling errors from year to year. A “buoy-year” was defined as any calendar year in which a single buoy had data available more than 75% of the time over the course of the year. Through this specification, a total of 525 buoy-years were identified from Pacific Ocean data for the period 1989-2013, Atlantic Ocean data from 1998-2013, and Indian Ocean data from 2002-2013. The mean of a buoy-year was compared with the annual mean of the nearest TropFlux grid to produce a bias estimate for each buoy and year. The same comparison was done using OAFlex input variables.

Figure 3.22 shows the annual residual bias (after standard corrections are applied) of OAFlux and TropFlux with respect to the TPR array from all 525 buoy years. The biases are against the variable in question, e.g., air-temperature biases are plotted against the annual mean air-temperatures measured by the buoys. The optimal interpolation procedures used to create OAFlux are designed to have low associated bias with respect to assimilated observations. TropFlux has a higher bias than OAFlux for moisture. OAFlux shows a larger bias for wind speed. Both gridded fluxes show little systematic bias for either air or ocean temperature.

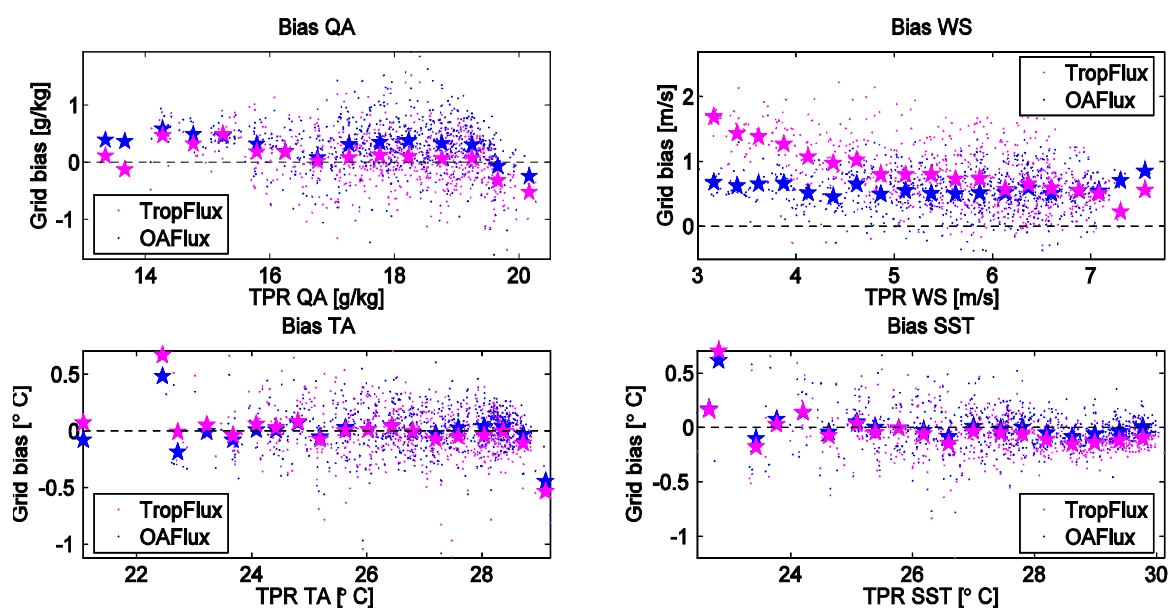


**Figure 3.22.** The bias computed as the annual average of OAFlux or TropFlux – TPR for 525 buoy years (small dots), and binned by the TPR values (stars). A buoy year is comprised of any calendar year in which buoy data was available greater than 75% of the year. Biases for specific humidity, wind speed, air temperature and SST are shown.

For OAFlux, the mean bias for  $q_{air}$  is  $0.06 \pm 0.02$  g/kg; for wind speed it is  $0.76 \pm 0.02$  m/s; for air temperature it is  $0.00 \pm 0.01$  °C; and for SST it is  $-0.07 \pm 0.01$  °C. For TropFlux, the bias for  $q_{air}$  is  $0.28 \pm 0.02$  g/kg; for wind speed it is  $0.53 \pm 0.01$  m/s; for air temperature it is  $0.03 \pm 0.01$  °C, and for SST it is  $-0.01 \pm 0.01$  °C. In this analysis, OAFlux

and TropFlux are assessed with respect to TPR buoy observations, and any significant deviation from 0 indicates some systematic error in the gridded products.

There are two caveats to interpreting this analysis. First, though OAFlux has a higher bias than TropFlux for wind speed, the TropFlux flux algorithm adds an additional gustiness correction to the wind speed used to compute bulk fluxes. The gustiness correction (Cronin et al, 2006) was developed for buoys to account for mesoscale convective features missed in the vector-averaged wind speed, by comparing hourly wind speed with the daily resolution vector-averaged wind speed from the buoys. The gustiness correction of 1.0-2.1 m/s depends on climatological SST. This climatological SST-dependent gustiness was added to wind speed in TropFlux prior to running COARE. The wind speed estimate provided on the TropFlux ftp site, and in Figure 3.25a (below), includes the constant bias correction, but not the gustiness. The bulk turbulent heat fluxes depend linearly on the magnitude of wind speed, so, adding 1.0-2.1 m/s to the wind speed scales up the sensible and latent heat and momentum fluxes proportionally.

Second, though both OAFlux and TropFlux show remarkable agreement with the buoy SST estimates, this temperature does not reflect the effects of thermodynamic processes of radiative heating in the diurnal warm layer and diffusive cooling in the viscous sub-layer. Hence, as shown in the R/V *Revelle* experiments of section 3.6.2, errors on the order of 10% of the flux magnitude may still result from using the sea temperature at 1 m depth to estimate the SST without the warm layer and cool skin corrections.

### **3.6.6 Intraseasonal variations of the warm layer computed with TropFlux and the solar model**

Negative outgoing longwave radiation (OLR) anomalies indicate deep convection in the active phase of the MJO. The passage of two distinct MJOs are visible in a Hovmoller (time-longitude) plot of OLR anomalies averaged over  $\pm 5^\circ$  latitude and plotted as a function of longitude with time increasing upward on the y-axis (Figure 3.23a). These events propagate eastward (shown by magenta lines) beginning in the end of October and the end of December around  $50^\circ$  longitude. Near-surface ocean temperature in the Indian Ocean and Maritime Continent are fairly constant near  $29^\circ\text{C}$ , as seen in Figure 3.23b, and there is weak intraseasonal variability detected. While the near-surface ocean temperature varies seasonally, the ocean skin temperature varies with the warm layer in the Indian Ocean (Figure 3.23c). The warm layer is modulated by the wind shear, and therefore varies seasonally and intraseasonally with the monsoon and MJO. In the Indian Ocean, the MJO convectively active phase is characterized by strong westerly wind bursts which serve to homogenize the upper ocean temperature profile, while calm wind and strong solar radiation in the suppressed phase support the development of a diurnal warm layer that raises the average SST. The warm layer correction minus the cool skin correction, computed with TropFlux input variables and the solar model using COARE version 3.5 shows a patchy intraseasonal warm signal in phase with the MJO suppressed phase, between the magenta lines.

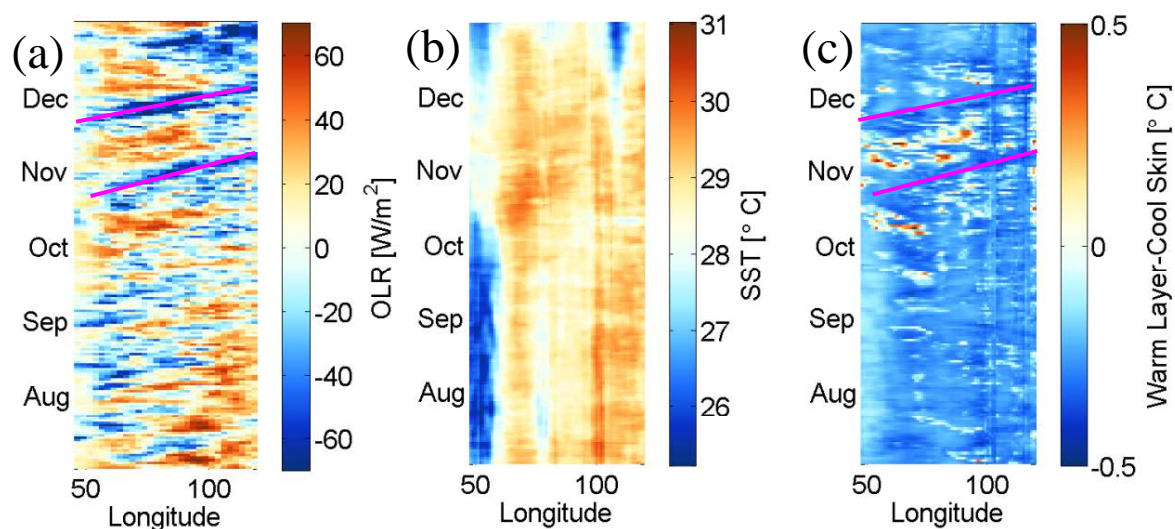


**Figure 3.23.** Time-longitude plots of outgoing longwave radiation anomalies (a), 1 m ocean temperature (b), and computed warm layer – cool skin corrections from 1 m to interface ocean temperature. Latitude is averaged over  $\pm 5^\circ$ , and the x-axis is longitude with the coast of Somalia on the left, and the maritime continent on the right

Kumar et al. (2012) propose a gustiness correction be added to the wind speed based on the climatological SST. This gustiness correction mixes out any warm layer nearly completely. Figure 3.24 shows a zonal plot of the meridional average over  $\pm 5^\circ$  latitude of the gustiness adjustment added to TropFlux wind speed. A large gustiness adjustment of about 2 m/s is added from the central Indian Ocean to the western Pacific Ocean, a relatively small correction was added to the Eastern Pacific, and the Atlantic correction decreased toward the east.

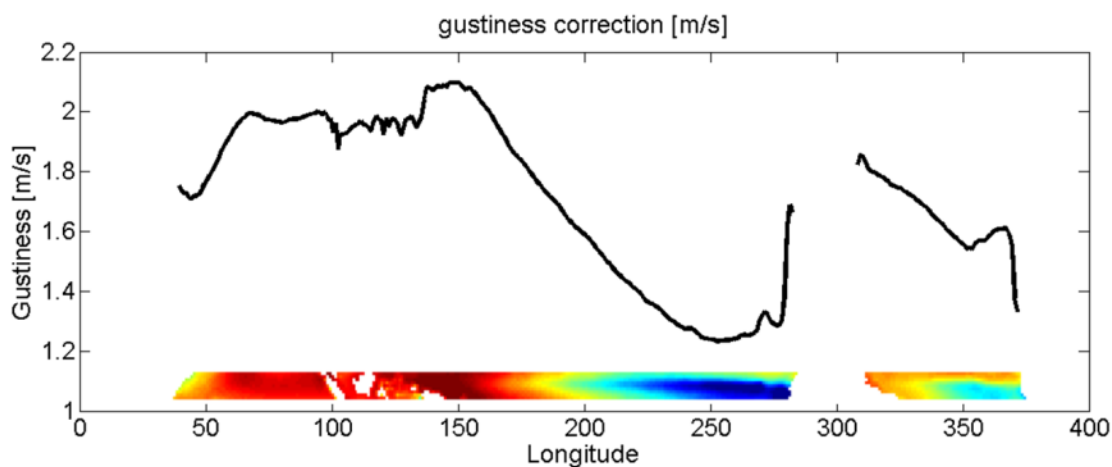


**Figure 3.24.** The average gustiness correction over  $\pm 5^\circ$  latitude added to TropFlux wind speed is plotted zonally. The  $\pm 5^\circ$  latitude strip is inset on the bottom for reference. Large gustiness corrections were added to the Indian Ocean, Maritime Continent, and Western Pacific. The spatially resolved gustiness correction is inset on the bottom for reference.

Figure 3.25a shows a time-longitude plot of the wind speed used to compute the warm layer and cool skin SST corrections in Figure 3.23c. As seen in the lookup table graphically displayed by Figure 3.17, a warm layer stronger than the cool skin effect only develops when wind speed is less than 2 m/s. These light-wind periods occur with greater likelihood in the equatorial Indian Ocean during the fall (Oct-Dec) as seen in the reported TropFlux wind speed (i.e. without the gustiness correction). When the gustiness adjustment is added, the wind speed rarely drops below 2 m/s, which as seen in Figure 3.17, is sufficient to mix down any accumulated heat and homogenize the ocean surface layer to 1 m depth, regardless of the intensity of solar radiation. This is apparent in Figure 3.25c as there are no periods where the warm layer overwhelms the cool skin as was seen in Figure 3.23c.

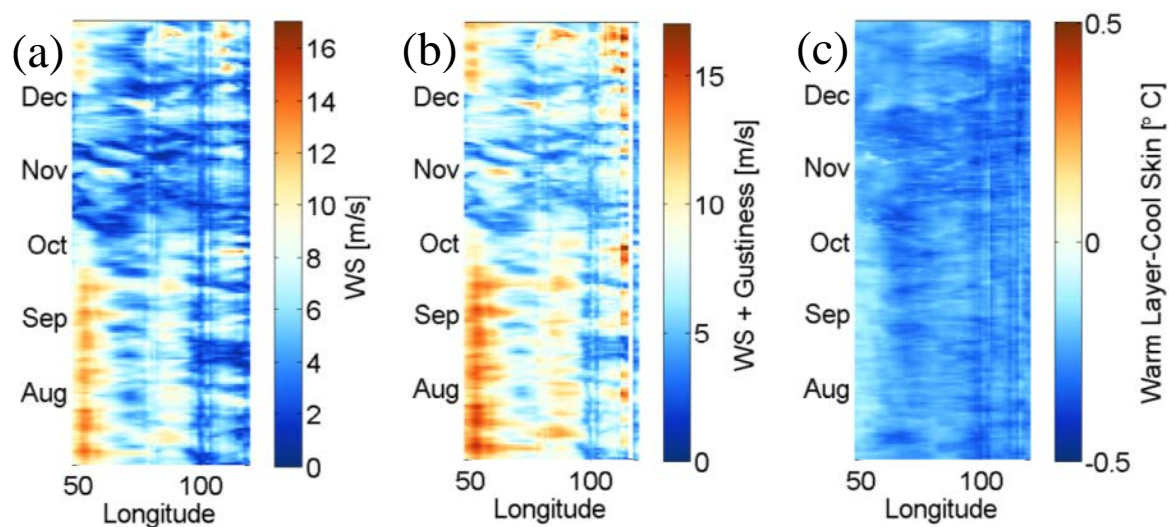


**Figure 3.25.** Time-longitude plots of TropFlux wind speed (a), wind speed +the proposed gustiness correction (b), and the warm layer – cool skin corrections computed with the gusty wind speed (c). Averaging is as in Figure 3.23

The results shown in Figures 3.25b and 3.25c are not supported by the observations. For example, consecutive days of persistently calm conditions were observed during the suppressed phase of the MJO with strong diurnal warming. Therefore, the addition of a gustiness adjustment to all wind speeds based on climatological SST may not be correct under all conditions of low wind speed. Though the warm layer has little effect on the mean sensible and latent heat fluxes over a long period, the additional evaporative fluxes that result from a pronounced warm layer may be important in the suppressed phase of the MJO.

## **3.7 DISCUSSION**

### **3.7.1 OAFlux and TropFlux Variability**

Though OAFlux and TropFlux both reproduce the mean SHF and LHF remarkably well when compared to R/V *Revelle* data (within ~5% of the mean flux), TropFlux overestimates variability in both SHF and LHF by 12 – 15%, while OAFlux underestimates SHF variability by about 12% but overestimates LHF variability by ~7%. Overestimation of heat flux variability appears to be attributable to the absence of warm layer physics: strong heat fluxes occur under high winds, but high winds also mix out the diurnal warm layer. Alternatively, the diurnal warm layer increases SST, sea-air temperature difference, and thereby the heat fluxes when winds are weak. The diurnal warm layer thus reduces variability in the fluxes due to the wind speed, and neglecting the diurnal warm layer unrealistically enhances diurnal and daily mean flux variability. The cool skin only weakly depends on wind. It is nearly constant so it does not systematically contribute much to the variability.

### **3.7.2 Intraseasonal variations of the warm layer the warm layer in gridded flux products**

When the effects of diurnal warming are included in the spatially resolved flux maps, an intraseasonal signal in phase with the MJO suppressed phase becomes more pronounced (section 3.6.6). This signal has not been incorporated into air-sea interaction studies thus far, and could have important implications for MJO dynamics. Using the solar model and COARE warm layer model to resolve this signal offers a new perspective that opens the door for additional studies of how air-sea interactions affect

the MJO. The R/V *Revelle* experiments and the look-up table quantify the relationship between daily average solar radiation, wind speed, and the warm layer correction, showing the magnitude the error introduced by ignoring the warm layer and cool skin corrections. The climatological mesoscale gustiness correction of 1.0-2.1 m/s is too aggressive to permit the observed warm layer, since wind speeds in excess of ~2 m/s mix the warm layer down to 1 m homogenizing the upper ocean layer. By adding the gustiness correction to wind speed, warm layer development is weaker and less variable in geographic regions with warm climatological SST. Yet these regions are observed to experience periods of persistent low winds modulated by seasonal and intraseasonal variability.

### **3.7.3 Gridded Flux Products in the Vicinity of a TPR buoy**

The reanalyses used by OAFlux and TropFlux ingest TPR buoy data to constrain the models. Additionally, OAFlux and TropFlux both use the TPR buoy data to estimate fluxes. This naturally causes a correlation of gridded products with fluxes computed at buoy locations, because the reanalysis and the buoy data are not independent. The remarkable agreement between the R/V *Revelle* fluxes and the 80.5° E RAMA buoy, and the correlation of gridded fluxes with TPR buoys explains the ability of the gridded products to reliably reproduce R/V *Revelle* fluxes and their variability when the R/V *Revelle* was near this RAMA buoy. All other locations for which independent data was compared show decreased skill in estimating the observed fluxes. Improved agreement in the vicinity of in situ data sources is also evident in histograms of the root mean square difference of buoy locations compared to non-buoy locations (Figure 3.7). The rms difference for non-buoy locations is 4 – 6 W/m<sup>2</sup> larger (40% of the mean for SHF, and 6% of the mean for LHF) than for buoy locations.

Flux calculation experiments from the R/V *Revelle* data show that the cool skin was of the greatest importance to the magnitude of the fluxes. Ignoring the cool skin resulted in an overestimate of both sensible and latent heat fluxes. Though OAFlux and TropFlux both neglect the cool skin correction, compensating errors may exist in the data inputs, bias corrections or assimilation procedures, or the flux algorithms for each product. TropFlux consistently overestimates SHF more than OAFlux with respect to independent in situ observations, perhaps due to differences in SST and wind speed. According to this analysis of all the TPR buoy data, OAFlux has a mean SST bias of  $-0.07^{\circ}\text{C}$  which is 23% of the average cool skin correction in the tropics. Using an SST that is biased low decreases the sea-air temperature difference, as does the cool skin adjustment. So the OAFlux underestimate of SST could actually compensate slightly for neglecting the cool skin correction and result in flux estimates that agree better with observations. The  $-0.01^{\circ}\text{C}$  bias of TropFlux compensates only 3% of the neglect of the cool skin correction on SST. Both gridded products have positive biases in wind speed that also contribute to the overestimate of computed fluxes.

Latent heat flux errors are less well explained by biases in inputs to the bulk flux algorithm. The assessment of the TropFlux bias corrections suggests that a positive bias of  $0.28\text{ g/kg}$  exists in the TropFlux specific humidity, making the air too moist, and reducing the sea-air moisture difference. The cool skin correction lowers the surface saturation specific humidity, based on the interface temperature, according to the Clausius-Clapeyron relation. By ignoring the cool skin correction of approximately  $0.3\text{ K}$ , the sea surface specific humidity is too high by approximately  $0.4\text{ g/kg}$ , and the sea-air

moisture difference is too large by ~5% which would result in a n overestimate of LHF. Combined with overestimates of wind speed of 10-15%, both OAFlux and TropFlux should overestimate LHF by > 15%. Yet Figure 3.21, which shows both gridded products compared to the five independent in situ time series used in this these, shows that both products underestimate LHF when compared to the APL buoys, and strongly overestimate LHF compared to the R/V *Moana Wave*. This suggests that the gridded LHF error may not be so easily attributed to biases in input variables. Since it is the sea-air moisture difference that is important to the fluxes, TropFlux may slightly compensate the effects of ignoring the cool skin related moisture depression by over moistening the air by +0.3 g/kg so that the sea-air moisture difference is closer to the true interfacial difference. These are examples of potentially compensating errors that would need to be examined before including the warm layer and cool skin dynamics would improve the mean flux estimates.

## CHAPTER 4: CONCLUSIONS

### 4.1 TURBULENCE FLUX CALCULATIONS

After extensive measurement set up, data logging and quality control, turbulent fluxes were calculated with DYNAMO data using eddy covariance and bulk methods. Individual 10 minute bulk flux calculations produce less variable time series for ship based flux calculations than eddy covariance (EC) methods because bulk methods are less sensitive to problems with motion corrections required to isolate true winds, sampling variability. The 10 minute means used for bulk fluxes are more easily and robustly sampled than higher moments such as the covariance. Though EC flux time series are highly variable, the mean over many flux estimates can be used to provide a good estimate of the flux under particular conditions. The covariances fluxes can be composited, e.g., as a function of wind speed, to see their dependence on the mean conditions. In fact, EC methods continue to be used to refine bulk transfer coefficients by comparing the ensemble of EC fluxes and their associated mean bulk fluxes computed from the same system.

The sensitivity of the EC fluxes to the averaging window length and detrending the perturbation variables varies for sensible and latent heat fluxes. The mean and standard deviation of the bulk fluxes were insensitive to changing the averaging window length. The mean 10-minute covariance latent heat flux was underestimated by ~5% compared to the bulk fluxes, while the 20-minute fluxes agreed within the accuracy of the

measurement. Covariance sensible heat flux agreed with bulk fluxes regardless of the averaging window length. This suggests that the largest eddies responsible for the exchange of moisture are less well sampled by the 10 minute window. This systematic difference suggests that structures responsible for turbulent moisture flux are of a larger-scale than those responsible for sensible heat flux. Removing the mean only instead of detrending resulted in ~20% larger average sensible heat flux, and ~5% underestimation of latent heat flux regardless of the choice of averaging window. Covariance fluxes showed the best agreement with bulk fluxes when a 20 minute window was used and all time series were detrended before covariances were computed.

## **4.2 WARM LAYER AND COOL SKIN CORRECTIONS**

The variable diurnal warm layer and nearly constant cool skin corrections affect daily average bulk fluxes. Experiments with the R/V *Revelle* time series were conducted to quantify errors in the fluxes due to changing the sea temperature input to the COARE bulk flux algorithm. Specifically, sea temperature measurements at different depths were input to the bulk algorithm. The computation varied according to the choices of whether to model the diurnal warm layer and cool skin temperature. The best estimates of fluxes are produced by applying a cool skin correction model to the observed ocean temperature measured at 0.05 m. The ocean temperature at 0.05 m depth effectively measures the diurnal warm layer. Using a 1 m temperature (interpolated between 4 m and 0.05 m depth) and modeling the warm layer and cool skin with observed solar radiation results in a root mean square error (RMSE) of 0.49 W/m<sup>2</sup> and 2.1 W/m<sup>2</sup> for sensible and latent heat respectively. This is the lowest error that can be expected using a 1 m bulk ocean

temperature. These experiments show that neglecting the cool skin correction resulted in the highest errors and a 10% over estimate of both sensible and latent heat fluxes.

The distribution of solar radiation over the hours of the day must be supplied to evaluate the diurnal warm layer accurately. This presents a problem when only daily averaged data are available, and the diurnal warm layer and cool skin are usually both neglected, assuming that their effects nearly cancel in the net. These correction rarely balance, in fact, the cool skin is mostly stronger, resulting in a net mean SST correction of  $-0.2$  °C.

Two methods for including the warm layer and cool skin corrections using daily average solar radiation were developed and tested. The most accurate is to run the COARE algorithm with a simple solar model that distributes the daily average insolation over the day according to the sun elevation. With this method, the resulting RMSE for sensible and latent heat fluxes are  $0.74$  W/m<sup>2</sup> and  $2.9$  W/m<sup>2</sup>, only slightly increased from using the sub-daily resolved observations.

In the second method, a lookup table is constructed by running the diurnal warm layer and cool skin under the simple solar model for different wind speeds and daily average solar radiation. The table summarizes the results of the warm layer and cool skin adjustments on SST and fluxes binned by daily average solar radiation and wind speed. Fluxes computed with both corrections ignored, as is the current practice with daily data, can then be adjusted by the values in the the lookup tables. When compared to the most accurate computations of the fluxes in DYNAMO, the resulting RMSEs for sensible and latent heat flux adjusted with the lookup table are  $0.96$  W/m<sup>2</sup> and  $3.5$  W/m<sup>2</sup>, respectively, only slightly worse than using the more accurate warm layer and cool skin corections

directly. A temperature correction can be added to the SST input to the COARE algorithm, or a net correction can be added to the final sensible and latent heat fluxes.

Ignoring both corrections completely results in much larger errors of  $2.1 \text{ W/m}^2$  and  $9.0 \text{ W/m}^2$  for sensible and latent heat, respectively. Fairall et al (1996b) state a goal of resolving the net heat flux estimate to an accuracy of  $\pm 10 \text{ W/m}^2$ . If daily average data with 1 m SST is used in an accurate bulk flux formula without the warm layer and cool skin adjustments, the combined RMSE for sensible and latent heat flux can easily exceed  $10 \text{ W/m}^2$ . Employing both corrections using a simple solar model is an effective way to improve flux estimates from daily average data. The lookup table for the warm layer/cool skin correction is a computationally inexpensive way to reduce error of daily average flux estimates, and could easily be used with gridded flux products. Additionally, the lookup table can be used to adjust fluxes directly and does not require the host of original input variables, only the daily average wind speed and solar radiation.

### **4.3 GRIDDED FLUX ESTIMATES**

The OAFlux and TropFlux gridded products assessed in this thesis make use of reanalyses that assimilate the TAO, PIRATA, and RAMA (TPR) buoys. Both gridded products also use the TPR buoys to validate and bias-adjust input variables used to make bulk flux calculations. For these reasons, OAFlux and TropFlux agree better with each other near buoys. Because much of the variability of the atmosphere is large scale and spatially autocorrelated, both products also exhibit higher skill replicating independent observations near buoys. OAFlux and TropFlux both produce high quality flux estimates,

provided there is a TAO/PIRATA/RAMA buoy nearby. Skill deteriorates for both gridded products as the distance from a buoy increases.

The RMSD for both gridded sensible and latent heat flux compared to the R/V *Revelle* are on the order of 5% of the mean. The RMSD increases to ~15-25% of the mean for latent and sensible heat flux respectively when compared to in situ observations more than 160 km from the nearest TPR buoy. Differences between gridded products at all 106 buoy locations for the calendar year of 2011 are higher than the single case of the R/V *Revelle* examined, with RMSDs on the order of 25% (latent heat flux), and 50% (sensible heat flux) of the mean. These numbers increase to 30% (latent) and 70% (sensible) of the mean when all common grid points are compared.

Some differences between OAFlux and TropFlux can be attributed to differences in variables input into the bulk algorithm. TropFlux specific humidity is ~0.3 g/kg higher than TPR specific humidity on average, while typical sea-air humidity differences are on the order of 5 g/kg. The TropFlux overestimate is about 5% of the mean sea-air difference. Both OAFlux and TropFlux use wind speeds that are biased high with respect to TPR (biases are +0.8 m/s, and +0.5 m/s respectively). TropFlux uses an SST that is adjusted to 1 m depth, and OAFlux uses a 0.5 m SST. Both products ignore the warm layer and cool skin corrections. Existing residual biases in input variables could be helping to compensate for some of the error associated with ignoring these SST corrections.

The experiments with the R/V *Revelle* fluxes show that the cool skin corrections make the biggest difference to the mean flux, and that ignoring the cool skin resulted in

overestimation of the fluxes by 10% for latent and 20% for sensible heat flux. The ability of both gridded products to capture the mean as well as they do while ignoring both corrections further suggests that compensating errors exist in their algorithms. TropFlux and OAFlux do not produce the same results—often one overestimates while the other underestimates fluxes—suggesting that the errors differ between the two products.

The compensating errors in OAFlux and TropFlux confound the warm layer/cool skin problem, such that gridded flux estimates do not uniformly agree better with in situ observations when cool skin and warm layer corrections are included. Both gridded products overestimate sensible heat flux (Figure 3.21), so proper adjustment of the sea temperature to estimate the SST will improve it. Latent heat flux is systematically underestimated by both products, however, and adjusting the sea temperature will further diminish it.

When TropFlux daily mean solar radiation and SST are used to compute hourly fluxes with the solar model to approximate the diurnal cycle, the warm layer and cool skin corrections (that adjust the 1 m SST to an interface temperature) have a patchy signal that is modulated by intraseasonal wind bursts. TropFlux uses a gustiness correction of 1.0-2.1 m/s based on the climatological SST. If this gustiness correction is added to the TropFlux wind, the warm layer is wiped out. The lookup table shows that wind speeds greater than 2 m/s are sufficient to homogenize the ocean surface layer, resulting in an interface temperature which is cooler than at 1 m. Observations of several calm days during the suppressed phases of two MJO cycles in the central Indian Ocean, and the corresponding observed intraseasonal signal in the warm layer, suggest that the TropFlux gustiness correction is not appropriate for low wind speeds, especially in the

suppressed phase of the MJO. This mesoscale gustiness correction does not take into account the different wind regimes of the MJO. The analysis presented in this thesis suggests that the gustiness correction and the common method for calculating daily average fluxes in global gridded products should be carefully revisited for a more accurate analysis of intraseasonal flux variability.

The propagation speed and genesis mechanism of the MJO remain open problems. The inclusion of the warm layer and cool skin corrections in spatially resolved daily average fluxes exposes patterns in spatial variability that were not evident from in situ data. The intraseasonal variation of the warm layer effect on SST, and its effect on fluxes, may explain some part of the transition of the MJO to the convective phase. Perhaps warm SST anomalies in advance of the MJO convective phase enhance local convergence through hydrostatic boundary layer pressure anomalies, inducing horizontal boundary layer moisture convergence that primes the atmosphere for deep convection. An observed intraseasonal SST signal in the MJO suppressed phase could prove an important contribution to outstanding scientific quandaries related to MJO initiation and propagation.

## **APPENDIX**

The OSU DYNAMO air-sea flux experimental setup is described, including instrument brands and models, instrument locations on the ship, and wiring. Following is a step by step procedure for collecting the data using the Campbell Scientific data logger software, and Card Convert. Finally quality control procedures specific to the OSU system are described.

### **A.1 EXPERIMENTAL SETUP**

The OSU CSAT3 sonic anemometer, Gladiator gyroscope/accelerometer, and LICOR Infrared Gas Analyzer (IRGA), were all mounted on the ship's forward mast (instrument heights are listed in Table 1). The Gladiator was mounted 70 cm aft of and 8.8 cm below the center of the CSAT3 transducers. Lacking exact measurements for the IRGA with respect to the sonic, my best estimate from a photograph of the system is that the IRGA is mounted approximately 30 cm port, 50 cm above and 60 cm aft of the center of the sonic transducers.

**Table A.1.** Instrumentation, sampling frequency, and measurement height

<b>Sensor</b>	<b>sampling frequency</b>	<b>Height (m)</b>
CSAT3 sonic anemometer	20 Hz	16.6
Gladiator motion pack	20 Hz	16.5
Licor7500	20 Hz	17.15
Radiometers (top PSD van)	1 Hz averaged to 1min	12.6
Vaisala hmp155 T/RH	20 Hz	12.32
Young barometer	20 Hz	7.65
Sea bird	1 Hz averaged to 1min	0.05-0.1
Ships Computer (SCS)		
compass	10 Hz	
GPS	10 z	

### **A.1.1 Wiring**

The Campbell Scientific CR3000 data logging program was written by Ed Swiatek (Campbell Scientific) and specifies the wiring for all instrumentation. Figure 1 shows the wiring for the CR3000 including the Gladiator motion sensor, Young barometer, and the ships navigation system.

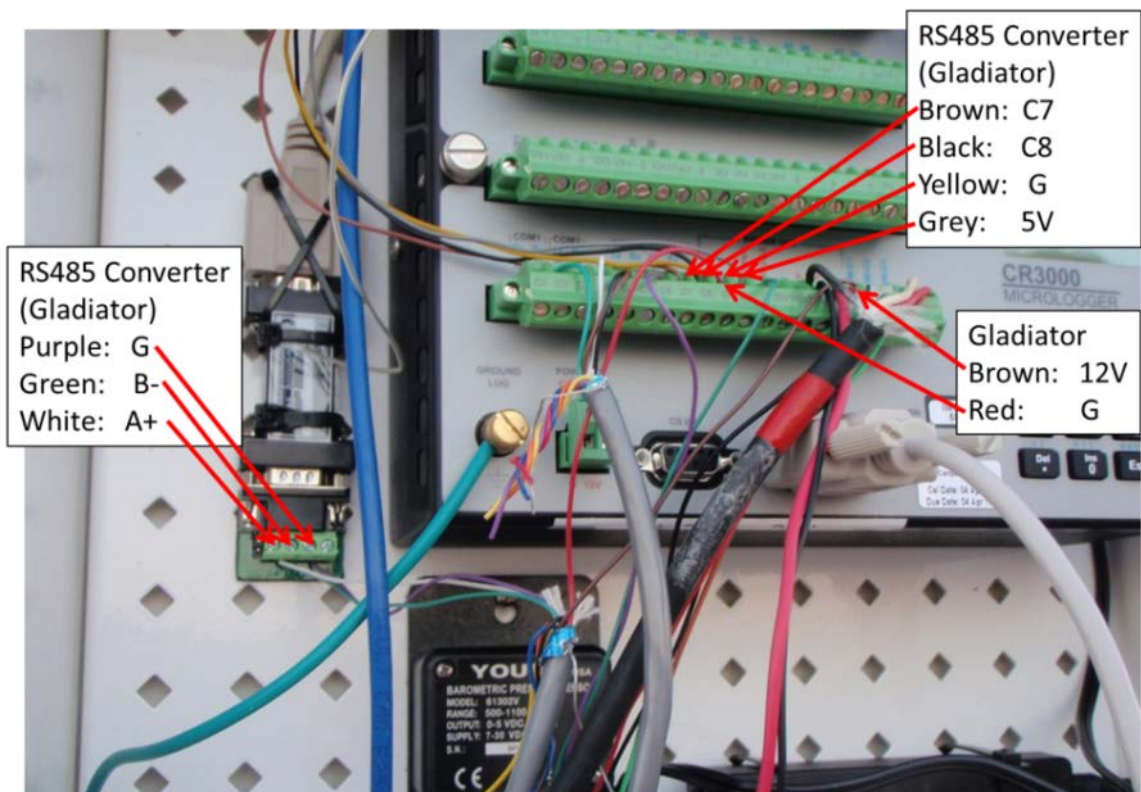


**Figure A.0.1.** Wiring for the Campbell CR3000, Gladiator gyroscope/accelerometer, including the RS485 converter.

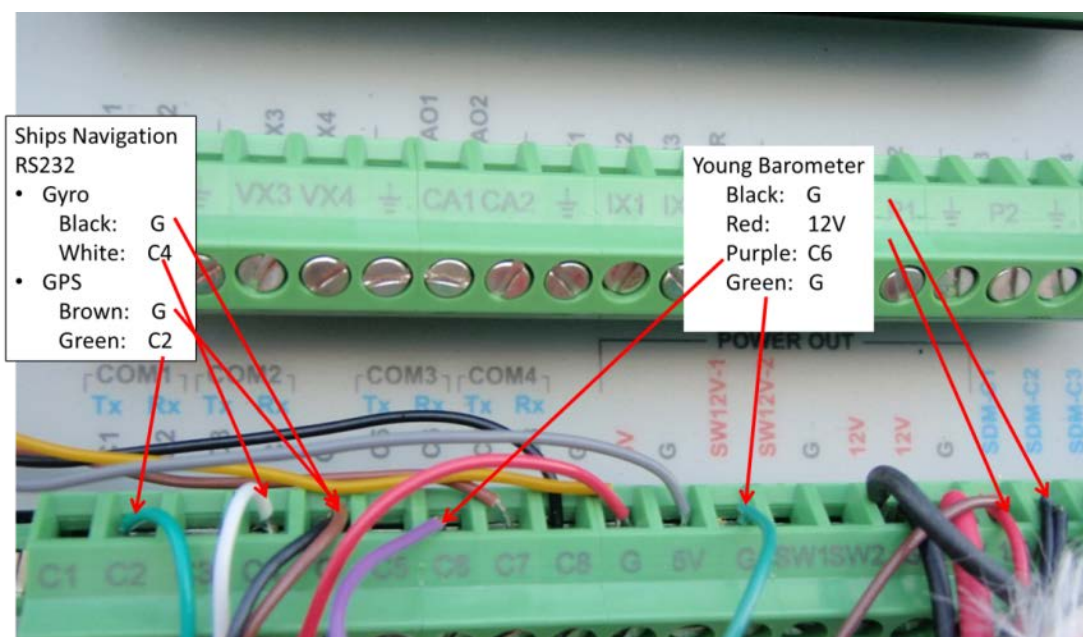


**Figure A.0.2.** Wiring for The ships navigation system and the Young barometer

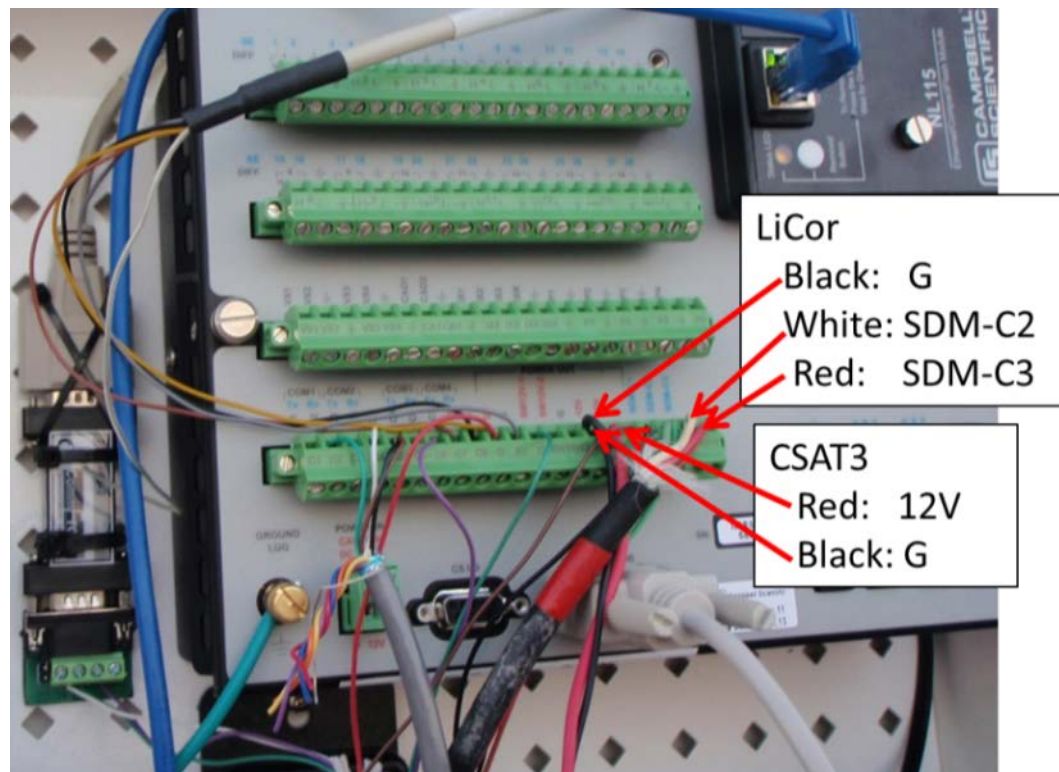


**Figure A.0.3.** Wiring for LiCor Infrared Gas Analyzer and CSAT3 Sonic Anemometer

### A.1.2 Data Acquisition

All 20 Hz data streams were logged in data tables on the memory card of the Campbell Scientific CR3000 data logger. The CSAT3 sonic winds and  $T_{sonic}$  were logged in the *ts* data table. The Gladiator accelerometer had a serial data stream that was impossible for the CR3000 to parse in real time, and its binary data stream was logged directly in the *landmark* data table. The ship GPS and compass data are in the *gps* data table and the *compass* data table, respectively. Additionally, there is a *diag\_stats* table that outputs diagnostic statistics for the system every thirty minutes.

The CR3000 has an internal ring memory which is capable of holding ~12 minutes of data before overwriting original data. A memory card was inserted in the

logger which could store several days of data; however it was necessary to download the data daily because it took ~5 minutes to retrieve one full day of data from the memory card. I attempted to use two memory cards and simply alternate between cards each time. However, the CR3000 stored data on the card and the internal ring memory. A digital marker is left on the card upon removal from the data logger which holds the place for the data logged on the internal memory while the card is out. Once the card is returned, the new data is then transferred to the card. If a second card is used, the logger has no reference for how to seamlessly restore the ring memory data to the memory card. In other words, without the reference marker left on card\_1, the entire ring memory was dumped onto card\_2 resulting in 5-10 minutes of repeated data written to card\_2.

The procedure for collecting data using one memory card is as follows:

1. In the data logger box, press the 'remove card' button
2. Wait until the light turns green
3. Remove the memory card
4. Immediately bring card to data processing computer and insert in card reader
5. Open the Campbell LoggerNet program.
6. Select '*Card Convert*' (see Figure A.4).



**Figure A.0.4.** The CR3000 welcome screen. Hover the mouse over the data tab to see cord convert and data viewing options.

7. Convert landmark files with options set as in Figure A.5. Note: Though the Gladiator Landmark outputs GPS time, this time data was not sufficient to synchronize the ship motion to the 20 Hz sonic anemometer data. Logging the time in the binary data table would change the data format in the file but may considerably simplify synchronization between the instruments.

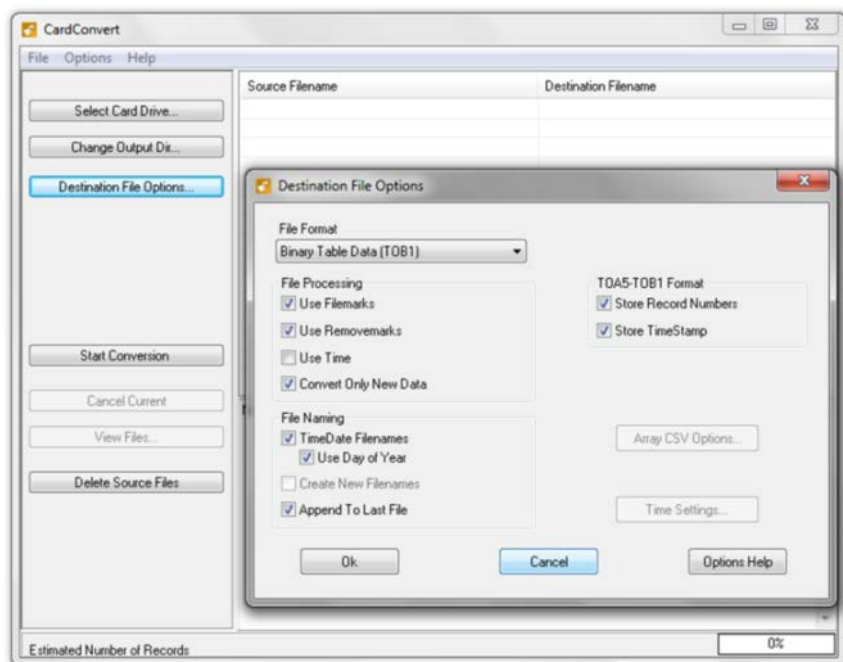


**Figure A.0.5.** Selection pane for binary files.

8. Convert all other data tables according to the options in Figure A.6.

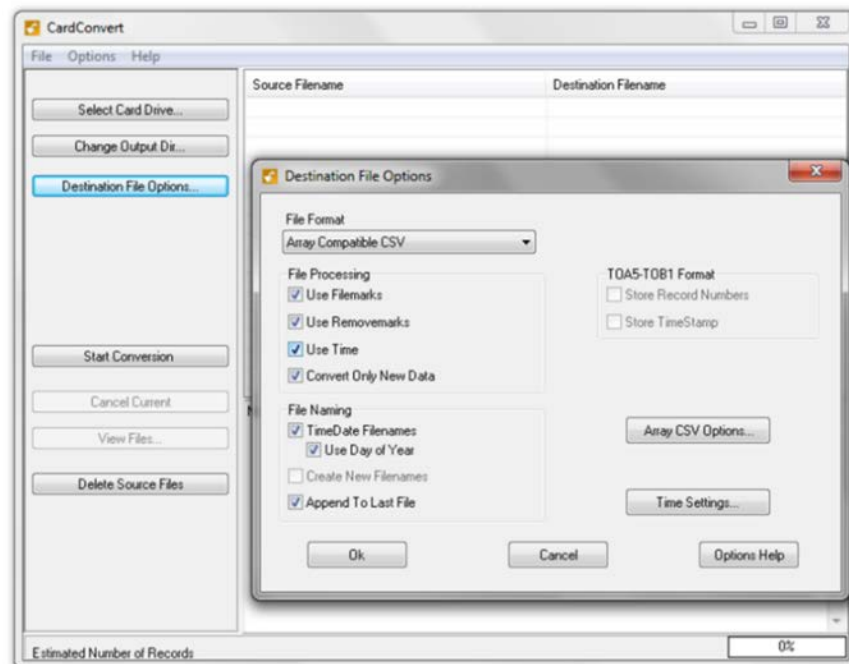


**Figure A.0.6.** Selection pane for CSV files

9. Immediately return card to data logger.
10. Wait until card is initialized.
11. Check that all data tables are logging properly.
12. If warnings do not clear and data tables are not logging, remove and reinsert card.

## **A.2 PROCESSING RAW DATA**

### **A.2.1 MATLAB Reader Programs**

All programs file names that end in “\_read” read and execute Phase 1 quality control. The time series (*ts*), *compass* and *gps* data tables are all Comma Separated Variables (CSV) which are easily read in MATLAB using `textscan`. When the data is collected from the memory card the first and last hour recorded for that day may be partial files. In that case these files must be concatenated to form one gapless hour. This is built into the MATLAB reader programs. Programs read and filter the data for unphysical values using a combination of built in diagnostics, exclusion of out of range values, and identification of missing values. This automated first pass quality control step is QC phase 1. Table 2 lists Phase 1 quality control procedures. The Gladiator Landmark gyro/accelerometer data was logged in binary in a separate data table called *landmark*. The *landmark* data has Phase 1 QC built into the reader files, which is accomplished through checksums and diagnostic flags.

The hourly .mat files are then saved for easy use in later programs. The location of programs, raw CSV and binary files, mat files, and descriptions of Phase 1 QC follows.

CSV and binary files are saved in:

*C:\Data\cruises\DYNAMO\_2011\Revelle\cr3000\Raw*

Files are then separated by legs 2 & 3. From here there is another folder called *Raw\_mat\_files*. This is where the hourly mat files are saved. Technically they are not raw, because Phase 1 QC has already been done.

Programs are located in:

*C:\Data\cruises\DYNAMO\_2011\Revelle\Scientific\_analysis\programs\cr3000*

- *CSV\_cr3000\_ts\_read.m*

Reads CSAT3 sonic winds, and sonic temperature, Vaisala HMP155 relative humidity and temperature and vapor pressure, LI-COR 7500 IRGA CO2 and H2O, and Young barometric pressure from

*C:\Data\cruises\DYNAMO\_2011\Revelle\cr3000\Raw\leg\*\* The \* is 2 for leg two and 3 for leg three. Files are saved as *ts\_ddd\_hh.mat* in the

*..Raw\_mat\_files* directory. *Tsonic* is a separate .mat file I made for Jim Edson in the *CSV\_cr3000\_ts\_read.m* program because he only wanted our sonic temperature without all the rest of the variables.

- *CSV\_cr3000\_compass\_read\_hrs.m*

Reads ship's heading from the ship's navigation system.

- *CSV\_cr3000\_gps\_read\_hrs.m*

Reads GPS from the ships navigation system. Latitude, longitude, degrees, minutes, speed over ground, course over ground, heading, and GPS height above mean sea level, and barometric pressure.

### **A.2.2 Quality Control**

Quality control for the OSU eddy covariance data happens in three phases. Phase one is implemented immediately in the raw data reader files (by reader programs above). Phase 2 comes from an automated inspection of data in which suspected “bad” data is flagged for later visual inspection of time series plots. The user may manually specify a solution to data problems specific to the day and hour that is affected. When no solution is evident the entire hour is discarded. Phase 3 QC happens in the flux processing whereby the data is filtered to exclude obstructed wind directions, significant maneuvers of the ship, and plume contamination.

Phase 1 QC is described in Table A.2.

**Table A.2.** Phase 1 quality control procedures, nan values in excess of min/max, missing values, and diagnostic flags as noted. Also despiked4sigma all data streams one time unless otherwise noted.

Sensor	variable	min	max	missing number	flag
CSAT3	U(x,y,z)	100	100		diag_csat>0
	Ts	0	50		diag_csat>0
Gyro	accel(x,y,z)				
	gyro(x,y,z)				
Licor	H2O	0		-7999	AGC>62, diag_irga>0
	CO2	0		-99999	AGC>62, diag_irga>0
Young barometer	Pressure			-7999	
Vaisala	T_hmp	23	32		Despike4sigma 2 times
	RH_hmp	0	110		Despike4sigma 1 time
	E_hmp	0	50		Despike4sigma 1 time
SCS	GPS			-7999	

Notes about phase 1 QC:

- The variable *diag\_csat* will take on values between and including 0 and 61503. A value of 0 indicates good data. 61440, 61441, 61442 and 61503 are associated with documented errors in the manual. Values of 12-15 are reserved as diagnostic flags. Values of 06-11 are associated with uvw ranges, and may indicate that further processing is required. Values of 00-05 are a counter. See CSAT3 manual chapter 10, pg 21-23, and Appendix B.4, pg B-5 for more information.

- Though it may be a conservative filter, all CSAT3 velocities and sonic temperature are set to not-a-number when values of `diag_csat` are nonzero.
- A matrix of nans is saved for use in later processing
- I chose to despike using the function `despike4sigma` and interpolate over nans in this phase of QC

#### Landmark QC:

Early in leg 2 severe data outages were observed in all high frequency variables. It was determined processing the accelerometer data stream overwhelmed the CR3000 when included as CSVs in the *ts* data stream. The Gladiator accelerometer was separated from the other 20 Hz data and logged as a binary signal in TOB1 format. This change in data acquisition fixed the outages, however, the binary files were difficult to read and synchronize with the ascii variables. Synchronization with other *ts* variables was challenging because the binary data had a GPS timestamp in a cryptic form that was defined as weeks and milliseconds since the beginning of the GPS epoch on January 6<sup>th</sup> 1980. The Landmark GPS time was less precise, and potentially different than the *ts* data table timestamp, which was generated by the CR3000 clock. Furthermore, occasionally the *landmark* data stream was corrupted either in the CR3000 or during the CardConvert procedure. Either way, these hours had to be manually quality controlled, which earned low confidence in these hours of data. The following summarizes the binary reader, gyro fix, and time sync programs.

Presumably, since the gyro and *ts* data were logged by the same system at the same time, the gyro data can be synchronize to the *ts* timestamp. This works well for most

files, however there are cases when the gyro data stream contains a different number of data points than the *ts* data.

- *Binary\_landmark\_read.m* written by Simon de Szoeki reads all gyro data and saves .mat files in `../Raw_mat_files/cr3landmark*.mat`
- *Gyro\_diagnostics* was run after all reader programs, but before any other processing of data. It produces a gps timestamp for the gyro data (*yday\_g*) and plots it on top of *yday\_ts*. This shows if gyro data and *ts* timestamps are lined up or not.
  - It can also indicate if nans are present in the beginning or end of gyro data.
  - Sometimes both data streams will have timestamp jumps, this signifies a general problem with data logging endemic to all instruments and data tables; these times are not recoverable.
  - This program also performs a series of inquiries in both data streams, described below, and outputs the results to an excel file (described below). This spreadsheet provides a succinct document which shows obvious errors and potentially subtle issues in both data streams.
- The excel file provides a framework to make corrections to gyro data if determined necessary. Corrected gyro files are saved as mat files. Tests are as follows:
  - Check first time and min time. They should be equal.
  - Check last time and max time. They should be equal.
  - Check length. *landmark* length should be the same as *ts* length.

- Check largest positive jump. Should be  $2.326e-6$  for gyro.
- Check largest negative jump. Should be 0.
- Check number of NaNs (not-a-number used to indicate missing data).
  - For *ts* timestamp, also check for uniqueness. All values in *ts* timestamp should be unique.

These quantities were all saved in a spreadsheet and flagged when they deviated from the usual operational values. This spread sheet helped in the development of the gyro fix program that was run before synchronizing the gyro data stream to the *ts* data.

*Gyrofix.m* saved in

*C:\Data\cruises\DYNAMO\_2011\Revelle\Scientific\_analysis\programs\cr3000\gyrofix.m*

- This m-file has specific fixes to each day for the unsynchronized gyro files. Fixes are specific to individual days/hours and should be run once after the read files (*Binary\_landmark\_read.m*), but before all other processing (*binary\_ts\_sync\_nan\_test.m*). Solutions for each corrupted file are described in-line in the fix file. Once fixed, it will not be obvious which files contained errors except by reading through the fix file. “Broken” files are moved to a separate folder (...\*Raw\_mat\_files\test20120821\broken\_matfiles*) to be used later.

as a backup in case investigation should be desired.

Broken .mat files are sent here (\*=2 or 3):

*C:\Data\cruises\DYNAMO\_2011\Revelle\cr3000\Raw\leg\_\*\Raw\_mat\_files\test2012082  
I\broken\_matfiles*

- *binary\_ts\_sync\_nan\_test.m* loads gyro and *ts* files and plots *accx* prior to any processing as a reference. A logical vector  $Q = \text{isnan}(accx)$  is saved so that nans can be added back into the data file in later processing because values are interpolated in the sync process which fills all NaNs even if there are large data gaps. Replacing NaNs gets rid of the linear interpolation over large chunks of missing data. The length of each file is checked, and if the  $\text{length}(yday\_ts) \neq \text{length}(accx)$  [is not equal to] a line prints the day and hour that has the problem, and length of each file in the format:
 

$\text{Length}(yday\_ts) = \text{#####}$ ,  $\text{Length}(gyro) = \text{#####}$ ,  $\text{Diff} = \text{#####}$ , and  $\text{Missing} = \text{#####}$  from the gyro file.

  - Variables then run through a deNaN function which interpolates over nans and stretches or shrinks the gyro data to match the *ts* data length. The new *accx* is then plotted on top of the original *accx*. If the sync went well the lower frequency oscillations should coincide and discrepancies should be in noise only. Sometimes adding a few nans to either the beginning or the end of a gyro file will sync data exactly.

- Sometimes data will repeat at the end of the hourly file (this is seen in the cryptic timestamp) so that truncating the file at the length of the ts file will result in synchronized files. This fix is difficult to test though because data is simply chopped; the challenge is knowing which part of the data is actually good, and which part is extraneous.
- Gyro files are then saved as mat files available for further use. It is important to be sure that any corrections made to the gyro data are appropriate because they will be more difficult to diagnose after this point. In any case the original files that were modified are saved in  
*C:\Data\cruises\DYNAMO\_2011\Revelle\cr3000\Raw\leg\_[2,3]\Raw\_mat\_files\test20120821\broken\_matfiles*
- Gyro files that are actually used in flux calculations are saved in  
*...\Raw\_mat\_files\cr3landmark\_sync\*.mat*

## BILIOGRAPHY

- Cassou, C. (2008). Intraseasonal interaction between the Madden–Julian Oscillation and the North Atlantic Oscillation. *Nature*, *455*(7212), 523–527. doi:10.1038/nature07286
- Clayson, C. A., & Bogdanoff, A. S. (2013). The Effect of Diurnal Sea Surface Temperature Warming on Climatological Air–Sea Fluxes. *Journal of Climate*, *26*(8), 2546–2556. doi:10.1175/JCLI-D-12-00062.1
- Daley, R. (1997). Atmospheric data assimilation. *JOURNAL-METEOROLOGICAL SOCIETY OF JAPAN SERIES 2*, *75*, 209–219.
- De Szoeki, S. P., Edson, J. B., Marion, J. R., & Fairall, C. W. (2014). The MJO and Air-Sea Interaction in TOGA COARE and DYNAMO. *Journal of Climate*.
- Dee, D. P., Uppala, S. M., Simmons, A. J., Berrisford, P., Poli, P., Kobayashi, S., ... Bauer, P. (2011). The ERA-Interim reanalysis: Configuration and performance of the data assimilation system. *Quarterly Journal of the Royal Meteorological Society*, *137*(656), 553–597.

Donald, A., Meinke, H., Power, B., Wheeler, M., & Ribbe, J. (2004).

Forecasting with the Madden-Julian Oscillation and the applications for risk management. In *Proceedings of the 4th International Crop Science Congress (ICSC 2004)*. Retrieved from <http://eprints.usq.edu.au/1140>

Edson, J. B., Jampana, V., Weller, R. A., Bigorre, S. P., Plueddemann, A. J., Fairall, C. W., ... Hersbach, H. (2013). On the Exchange of Momentum over the Open Ocean. *Journal of Physical Oceanography*, 43(8), 1589–1610. doi:10.1175/JPO-D-12-0173.1

Fairall, C. W., Bradley, E. F., Godfrey, J. S., Wick, G. A., Edson, J. B., & Young, G. S. (1996). Cool-skin and warm-layer effects on sea surface temperature. *Journal of Geophysical Research: Oceans (1978–2012)*, 101(C1), 1295–1308.

Fairall, C. W., Bradley, E. F., Hare, J. E., Grachev, A. A., & Edson, J. B. (2003). Bulk Parameterization of Air–Sea Fluxes: Updates and Verification for the COARE Algorithm. *Journal of Climate*, 16(4). Retrieved from <http://search.ebscohost.com/login.aspx?direct=true&profile=ehost&scope=site&authtype=crawler&jrnl=08948755&AN=9061005&h=fCYI>

AEdVCnEKwc9hw7B0xVQLhsn7iA%2BfD7A9FKuOju8tadmE0DU  
34ELuauMOJmmfzTuJEip2EW%2F6gGNUeuqN6g%3D%3D&crl=c

Fairall, C. W., Bradley, E. F., Rogers, D. P., Edson, J. B., & Young, G. S.

(1996a). Bulk parameterization of air-sea fluxes for tropical ocean-global atmosphere coupled-ocean atmosphere response experiment. *Journal of Geophysical Research: Oceans (1978–2012)*, *101(C2)*, 3747–3764.

Fairall, C. W., Bradley, E. F., Rogers, D. P., Edson, J. B., & Young, G. S.

(1996b). Bulk parameterization of air-sea fluxes for tropical ocean-global atmosphere coupled-ocean atmosphere response experiment. *Journal of Geophysical Research: Oceans (1978–2012)*, *101(C2)*, 3747–3764.

Fairall, C. W., White, A. B., Edson, J. B., & Hare, J. E. (1997). Integrated

Shipboard Measurements of the Marine Boundary Layer. *Journal of Atmospheric and Oceanic Technology*, *14(3)*, 338–359.

doi:10.1175/1520-0426(1997)014<0338:ISMOTM>2.0.CO;2

Foken, T., & Nappo, C. J. (2008). *Micrometeorology*. Springer.

Fuehrer, P. L., & Friehe, C. A. (2002). Flux corrections revisited. *Boundary-Layer Meteorology*, *102(3)*, 415–458.

- Jin, X., & Weller, R. A. (2008a). *Multidecade Global Flux Datasets from the Objectively Analyzed Air-sea Fluxes (OAFlux) Project: Latent and Sensible Heat Fluxes, Ocean Evaporation, and Related Surface Meteorological Variables* Lisan Yu. OAFlux Project Tech. Rep. OA-2008-01. Retrieved from [ftp://159.226.119.59/ftp/ds135\\_OAFLUX-v3-netheat\\_1\\_1day\\_netcdf/OAFlux\\_TechReport\\_3rd\\_release.pdf](ftp://159.226.119.59/ftp/ds135_OAFLUX-v3-netheat_1_1day_netcdf/OAFlux_TechReport_3rd_release.pdf)
- Jin, X., & Weller, R. A. (2008b). *Multidecade Global Flux Datasets from the Objectively Analyzed Air-sea Fluxes (OAFlux) Project: Latent and Sensible Heat Fluxes, Ocean Evaporation, and Related Surface Meteorological Variables* Lisan Yu. OAFlux Project Tech. Rep. OA-2008-01. Retrieved from [ftp://159.226.119.59/ftp/ds135\\_OAFLUX-v3-netheat\\_1\\_1day\\_netcdf/OAFlux\\_TechReport\\_3rd\\_release.pdf](ftp://159.226.119.59/ftp/ds135_OAFLUX-v3-netheat_1_1day_netcdf/OAFlux_TechReport_3rd_release.pdf)
- Kaimal, J. C., & Wyngaard, J. C. (1990). The Kansas and Minnesota experiments. *Boundary-Layer Meteorology*, 50(1-4), 31–47.
- Kalnay, E., Kanamitsu, M., Kistler, R., Collins, W., Deaven, D., Gandin, L., ... Joseph, D. (1996). The NCEP/NCAR 40-Year Reanalysis Project. *Bulletin of the American Meteorological Society*, 77(3), 437–471.  
doi:10.1175/1520-0477(1996)077<0437:TNYRP>2.0.CO;2
- Kanamitsu, M., Ebisuzaki, W., Woollen, J., Yang, S.-K., Hnilo, J. J., Fiorino, M., & Potter, G. L. (2002). NCEP–DOE AMIP-II Reanalysis

(R-2). *Bulletin of the American Meteorological Society*, 83(11), 1631–1643. doi:10.1175/BAMS-83-11-1631

Kumar, B. P., Vialard, J., Lengaigne, M., Murty, V. S. N., & McPhaden, M.

J. (2012a). TropFlux: air-sea fluxes for the global tropical oceans—description and evaluation. *Climate Dynamics*, 38(7-8), 1521–1543.

Kumar, B. P., Vialard, J., Lengaigne, M., Murty, V. S. N., & McPhaden, M.

J. (2012b). TropFlux: air-sea fluxes for the global tropical oceans—description and evaluation. *Climate Dynamics*, 38(7-8), 1521–1543.

Large, W. G., & Pond, S. (1981). Open ocean momentum flux

measurements in moderate to strong winds. *Journal of Physical Oceanography*, 11(3), 324–336.

Large, W. G., & Pond, S. (1982). Sensible and latent heat flux measurements

over the ocean. *Journal of Physical Oceanography*, 12(5), 464–482.

Lau, K.-M., & Chan, P. H. (1988). Intraseasonal and Interannual Variations

of Tropical Convection: A Possible Link between the 40–50 Day

Oscillation and ENSO? *Journal of the Atmospheric Sciences*, 45(3),

506–521. doi:10.1175/1520-0469(1988)045<0506:IAIVOT>2.0.CO;2

Lin, X., & Johnson, R. H. (1996). Heating, moistening, and rainfall over the

western Pacific warm pool during TOGA COARE. *Journal of the*

*Atmospheric Sciences*, 53(22), 3367–3383.

Ling, J., Bauer, P., Bechtold, P., Beljaars, A., Forbes, R., Vitart, F., ...

Zhang, C. (2014). Global vs. Local MJO Forecast Skill of the ECMWF model during DYNAMO. *Monthly Weather Review*, (2014). Retrieved from <http://journals.ametsoc.org/doi/abs/10.1175/MWR-D-13-00292.1>

Liu, W. T., & Businger, J. A. (1975). Temperature profile in the molecular sublayer near the interface of a fluid in turbulent motion. *Geophysical Research Letters*, 2(9), 403–404. doi:10.1029/GL002i009p00403

Liu, W. T., Katsaros, K. B., & Businger, J. A. (1979). Bulk parameterization of air-sea exchanges of heat and water vapor including the molecular constraints at the interface. *Journal of the Atmospheric Sciences*, 36(9), 1722–1735.

Madden, R. A., & Julian, P. R. (1971). Detection of a 40-50 day oscillation in the zonal wind in the tropical Pacific. *Journal of the Atmospheric Sciences*, 28(5), 702–708.

Maloney, E. D., & Hartmann, D. L. (2000). Modulation of hurricane activity in the Gulf of Mexico by the Madden-Julian oscillation. *Science*, 287(5460), 2002–2004.

- Maloney, E. D., & Sobel, A. H. (2004). Surface Fluxes and Ocean Coupling in the Tropical Intraseasonal Oscillation. *Journal of Climate*, *17*(22), 4368–4386. doi:10.1175/JCLI-3212.1
- Maloney, E. D., & Xie, S.-P. (2013). Sensitivity of tropical intraseasonal variability to the pattern of climate warming. *Journal of Advances in Modeling Earth Systems*, *5*(1), 32–47. doi:10.1029/2012MS000171
- Monin, A. S., & Obukhov, Am. (1954). Basic laws of turbulent mixing in the surface layer of the atmosphere. *Contrib. Geophys. Inst. Acad. Sci. USSR*, *151*, 163–187.
- Neelin, J. D., Held, I. M., & Cook, K. H. (1987). Evaporation-Wind Feedback and Low-Frequency Variability in the Tropical Atmosphere. *Journal of the Atmospheric Sciences*, *44*(16), 2341–2348. doi:10.1175/1520-0469(1987)044<2341:EWFALF>2.0.CO;2
- Price, J. F., Weller, R. A., & Pinkel, R. (1986). Diurnal cycling: Observations and models of the upper ocean response to diurnal heating, cooling, and wind mixing. *Journal of Geophysical Research: Oceans*, *91*(C7), 8411–8427. doi:10.1029/JC091iC07p08411
- Reynolds, R. W., Rayner, N. A., Smith, T. M., Stokes, D. C., & Wang, W. (2002). An improved in situ and satellite SST analysis for climate. *Journal of Climate*, *15*(13), 1609–1625.

Reynolds, R. W., Smith, T. M., Liu, C., Chelton, D. B., Casey, K. S., &

Schlax, M. G. (2007). Daily high-resolution-blended analyses for sea surface temperature. *Journal of Climate*, 20(22), 5473–5496.

Saunders, P. M. (1967). The Temperature at the Ocean-Air Interface.

*Journal of the Atmospheric Sciences*, 24(3), 269–273.

doi:10.1175/1520-0469(1967)024<0269:TTATOA>2.0.CO;2

Schubert, J. J., Stevens, B., & Crueger, T. (2013). Madden-Julian oscillation

as simulated by the MPI Earth System Model: Over the last and into the next millennium. *Journal of Advances in Modeling Earth Systems*,

5(1), 71–84.

Straub, K. H., & Kiladis, G. N. (2002). Observations of a Convectively

Coupled Kelvin Wave in the Eastern Pacific ITCZ. *Journal of the*

*Atmospheric Sciences*, 59(1), 30–53. doi:10.1175/1520-

0469(2002)059<0030:OOACCK>2.0.CO;2

Stull, R. B. (1988). *An introduction to boundary layer meteorology* (Vol.

13). Springer. Retrieved from

<http://books.google.com/books?hl=en&lr=&id=BK8P9rl->

[CB4C&oi=fnd&pg=PR11&dq=boundary+layer+meteorology&ots=oc](http://books.google.com/books?hl=en&lr=&id=BK8P9rl-CB4C&oi=fnd&pg=PR11&dq=boundary+layer+meteorology&ots=oc)

[dv5uGfjE&sig=cp7buDy4xi4WpoXAQ4RUFCK413A](http://books.google.com/books?hl=en&lr=&id=BK8P9rl-dv5uGfjE&sig=cp7buDy4xi4WpoXAQ4RUFCK413A)

Vickers, D., & Mahrt, L. (1999). Observations of non-dimensional wind shear in the coastal zone. *Quarterly Journal of the Royal*

*Meteorological Society*, 125(559), 2685–2702.

Von Plato, J. (1991). Boltzmann's ergodic hypothesis. *Archive for History of*

*Exact Sciences*, 42(1), 71–89.

Webster, P. J., & Lukas, R. (1992). TOGA COARE: The Coupled Ocean—

Atmosphere Response Experiment. *Bulletin of the American*

*Meteorological Society*, 73(9), 1377–1416. doi:10.1175/1520-

0477(1992)073<1377:TCTCOR>2.0.CO;2

Wheeler, M. C., & Hendon, H. H. (2004). An all-season real-time

multivariate MJO index: Development of an index for monitoring and prediction. *Monthly Weather Review*, 132(8). Retrieved from

[http://search.ebscohost.com/login.aspx?direct=true&profile=ehost&sc](http://search.ebscohost.com/login.aspx?direct=true&profile=ehost&scope=site&authtype=crawler&jrnl=00270644&AN=14084042&h=ydv)

[ope=site&authtype=crawler&jrnl=00270644&AN=14084042&h=ydv](http://search.ebscohost.com/login.aspx?direct=true&profile=ehost&scope=site&authtype=crawler&jrnl=00270644&AN=14084042&h=ydv)

[Pa7yIfHdvQST8zJmg%2FwU6cje%2BbfdRgpb3q%2F%2FtOQG4hB](http://search.ebscohost.com/login.aspx?direct=true&profile=ehost&scope=site&authtype=crawler&jrnl=00270644&AN=14084042&h=ydv)

[9Rca90%2B%2FxknD9iXn9yOAMfreGJkriTjQO4Bxn6Xw%3D%3](http://search.ebscohost.com/login.aspx?direct=true&profile=ehost&scope=site&authtype=crawler&jrnl=00270644&AN=14084042&h=ydv)

[D&crl=c](http://search.ebscohost.com/login.aspx?direct=true&profile=ehost&scope=site&authtype=crawler&jrnl=00270644&AN=14084042&h=ydv)

Woodruff, S. D., Diaz, H. F., Elms, J. D., & Worley, S. J. (1998). COADS

Release 2 data and metadata enhancements for improvements of

marine surface flux fields. *Physics and Chemistry of the Earth*, 23(5), 517–526.

Yu, L., & Weller, R. A. (2007). Objectively analyzed air-sea heat fluxes for the global ice-free oceans (1981-2005). Retrieved from <http://darchive.mblwhoilibrary.org/handle/1912/4115>

Zhang, C. (2005). Madden-Julian oscillation. *Reviews of Geophysics*, 43(2). Retrieved from <http://www.agu.org/pubs/crossref/2005/2004RG000158.shtml>

Zhang, Y., Rossow, W. B., Lacis, A. A., Oinas, V., & Mishchenko, M. I. (2004). Calculation of radiative fluxes from the surface to top of atmosphere based on ISCCP and other global data sets: Refinements of the radiative transfer model and the input data. *Journal of Geophysical Research: Atmospheres* (1984–2012), 109(D19). Retrieved from <http://onlinelibrary.wiley.com/doi/10.1029/2003JD004457/full>